Unconventional Superconductivity in the Layered Iron Germanide YFe$_2$Ge$_2$

Jiasheng Chen

Supervisor: Prof. Malte Grosche

Department of Physics
University of Cambridge

This dissertation is submitted for the degree of
Doctor of Philosophy

Trinity College

October 2019

Declaration

This dissertation is the result of my own work and includes nothing which is the outcome of work done in collaboration except as specified in the text and Acknowledgements.

It is not substantially the same as any that I have submitted, or, is being concurrently submitted for a degree, diploma or other qualification at the University of Cambridge or any other University or similar institution except as specified in the text. I further state that no substantial part of my dissertation has already been submitted, or, is being concurrently submitted for any such degree, diploma or other qualification at the University of Cambridge or any other University of similar institution except as specified in the text.

It does not exceed the prescribed word limit of 60,000 words.

Some of the work described herein has been published in scientific journals. In particular, Chapter 4 contains material from:

- **J. Chen**, M. B. Gamża, K. Semeniuk, and F. M. Grosche. Composition dependence of bulk superconductivity in YFe_2Ge_2. Physical Review B **99**, 020501(R) (2019).

- **J. Chen**, K. Semeniuk, Z. Feng, P. Reiss, P. Brown, Y. Zou, P. W. Logg, G. I. Lampronti and F. M. Grosche. Unconventional Superconductivity in the Layered Iron Germanide YFe_2Ge_2. Physical Review Letters **116**, 127001 (2016).

<div align="right">

Jiasheng Chen
October 2019

</div>

Unconventional Superconductivity in the Layered Iron Germanide YFe_2Ge_2

Jiasheng Chen

Since the discovery of superconductivity in LaFePO, numerous iron-based superconductors have been identified within diverse structure families. Superconductivity in the layered iron germanide YFe_2Ge_2 was first reported in 2014. It stands out from the commonly known iron- based superconductor families for not containing either Group-V or Group-VI elements and has since been predicted to be an unconventional superconductor.

The intermetallic d-electron system YFe_2Ge_2 exhibits an unusually high Sommerfeld coefficient of $\approx 100\,\mathrm{mJ/molK^2}$, signalling strong electronic correlations. Its low-temperature normal-state resistivity displays a $T^{1.5}$ power-law temperature dependence, which is an indication of non-Fermi-liquid behaviour. While superconductivity in YFe_2Ge_2 has been widely observed below $T_c \approx 1.9\,\mathrm{K}$ in electric transport measurements, evidence of a bulk superconducting transition has proved elusive. This has prompted significant efforts into improving the crystal quality.

In this thesis, I present the crystal growth methods which have successfully produced high-quality poly- and single-crystal YFe_2Ge_2 samples. Measurements on these samples have led to conclusive evidence that superconductivity is an intrinsic property of this compound. Disorder effects on both the poly- and single-crystals have been studied through structural investigations, in which anti-site disorder of germanium substitution on the iron site was found to be the dominant factor. The fast suppression of the superconducting transition temperature, T_c, of YFe_2Ge_2 by disorder suggests an unconventional pairing mechanism. Using a liquid transport flux method, single crystals with residual resistivity ratios ($\mathrm{RRR} = \rho_{300\,\mathrm{K}}/\rho_{2\,\mathrm{K}}$) reaching 470 have been synthesised. These crystals exhibit clear bulk superconducting transitions. Low-temperature specific heat and μSR measurements performed on these crystals provided evidence for multi-gap superconductivity, most likely of the $s^{\pm}$-wave nature, which is compatible with theoretical predictions. Moreover, quantum oscillations have been detected for the first time in dHvA susceptibility and tunnel-diode oscillation measurements of high-quality YFe_2Ge_2 single crystals. Although unable to account fully for the high Sommerfeld coefficient, the current results have confirmed significant mass enhancements in the detected Fermi surface sheets.

Acknowledgements

Mukherjee, David Jarvis, Puthipong Worasaran, Stephen Hodgson, Cheng Liu, Dr. Patricia Alireza, Dr. Montu Saxena, Dr. Mike Sutherland, Dr. Sian Dutton, Prof. Gilbert Lonzarich, Prof. John Cooper and other members of the QM group.

Last but not least, I would like to thank my parents and my wife Xin Lin for their continuous love and encouragement.

Table of contents

Chapter 1

Introduction

1.1 Unconventional superconductivity and the iron-based superconductors

Superconductivity is a fascinating macroscopic quantum phenomenon found in an ever-expanding set of materials. Since its first demonstration by Heike Kamerlingh Onnes in 1911 in the element of mercury, a tremendous amount of effort has been devoted to discovering novel superconductors with an ever increasing critical temperature T_c and to better understanding the underlying mechanisms. Among these research efforts was the great success by Bardeen, Cooper and Schrieffer (BCS) in the 1950s for formulating a microscopic theory of the pairing mechanism which explains the physics behind what are now known as 'conventional' superconductors. In these materials, an effective attraction between the electrons is achieved through interactions of these electrons with the crystal lattice vibrations, or phonons. This allows the electrons to overcome their electrostatic Coulomb repulsion and form the so-called Cooper pairs, enabling the formation of a superconducting condensate at low temperatures. Traditionally, the BCS theory is believed to support an upper limit for T_c below $30\,\text{K}$, based on the known strength of the electron-phonon interaction in these materials. But recent demonstrations of superconductivity in high-pressure hydrogen sulfide H_2S at $203\,\text{K}$ [1] and LaH_{10} at $250\,\text{K}$ [2] showed that the technological benefits of superconductivity, in particular dissipationless electrical current flow with its enormous potential for super-efficient electric motors and generators, are not fundamentally limited to low temperatures.

In LaH_{10} and other hydrogen-rich materials, superconductivity is again *conventional* and mediated by deformations of the crystal lattice which, however, reach to very high energies. This is thanks to the light mass of the hydrogen atoms and the large spring constants caused by strong compression under pressure of nearly 2 million atmospheres. Unfortunately, this
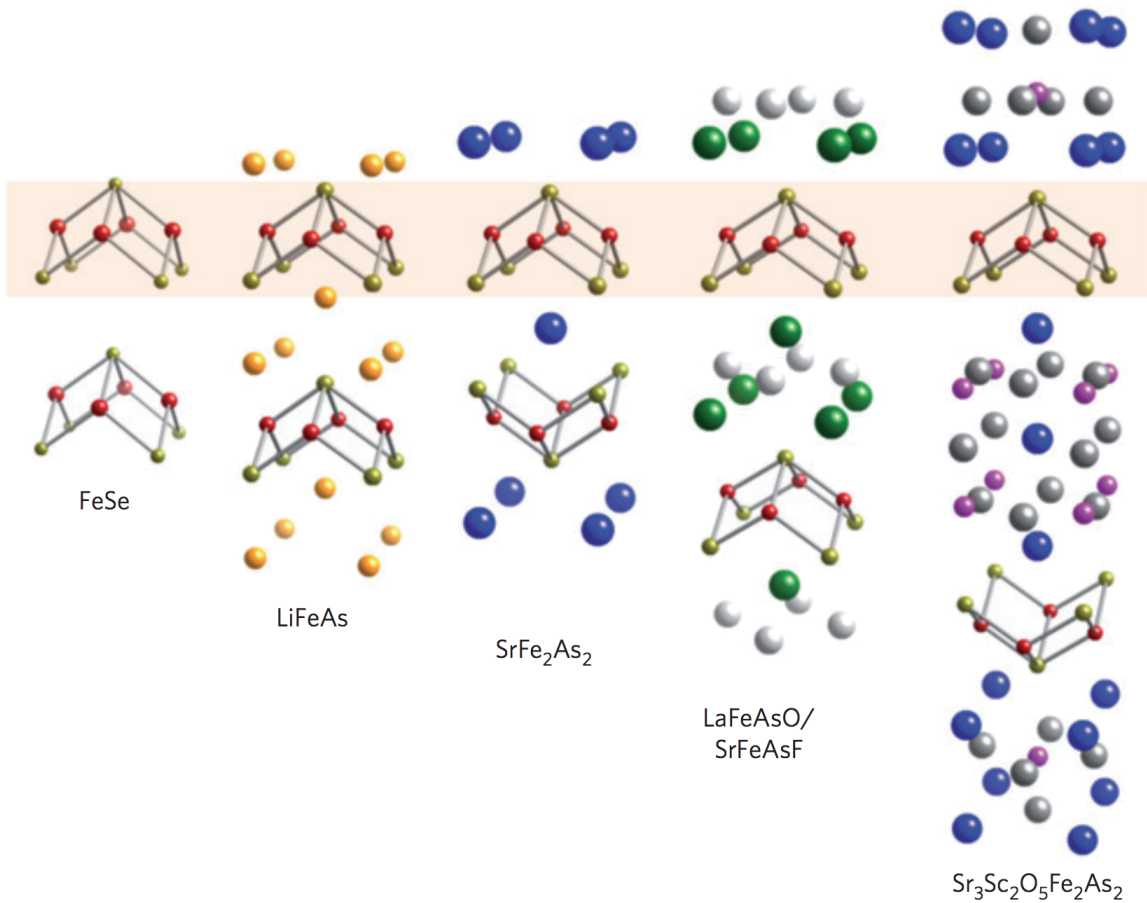
Fig. 1.1 Structure of different iron-based superconductor families, showing the common building block of the iron pnictogen/chalcogen trilayer. Iron atoms are represented by the red spheres. (Figure credit: [3])

mechanism probably cannot be extended straightforwardly to ambient pressure. Instead, *unconventional* superconductors harness the ultra-strong direct electronic interactions which are known in some cases to reach coupling energies equivalent to several thousand Kelvin, and can stabilise magnetism far above room temperature. Beginning in the late 1980s, excitement was brought about by the discoveries of a series of layered copper-based superconductors (cuprates), with some of these materials demonstrating transition temperatures much above the boiling point of liquid nitrogen ($T = 77$ K), making them functionally more useful. More recently, the discovery of superconductivity with relatively high T_c in wide structural families of layered iron-based compounds has again fuelled the interests of many researchers. High T_c

in the iron-based superconductors (FeSCs) came as a surprise, since iron, being a ferromagnet, was customarily believed to be detrimental to superconductivity based on the BCS theory.

Since the discovery of superconductivity at 5 K in LaFePO in 2006 [6], diverse structural families of FeSCs have been found, almost all of which combine iron with a group-V (pnictogen) or a group-VI (chalcogen) element. A common building block to these materials is an Fe-X (X being a pnictogen or chalcogen element) trilayer (Fig. 1.1), where the Fe atoms form a square planar lattice with each Fe atom at the centre of a distorted tetrahedron formed by the X atoms. Different crystal structures can be derived by the insertion of different "bridging layers" between the Fe-X trilayers. These structural families include the 11-type (FeSe, FeTe) with no bridging layer, the 111-type (LiFeAs, NaFeAs), the 122-type (KFe_2As_2, $BaFe_2As_2$), the 1111-type (LaFeAsO, SmFeAsO) and the more exotic compounds such as $(Sr_4Sc_2O_6)Fe_2P_2$ [7] and $(Ca_3Al_2O_{5-y})Fe_2As_2$ [8]. Apart from the similar basic structure,
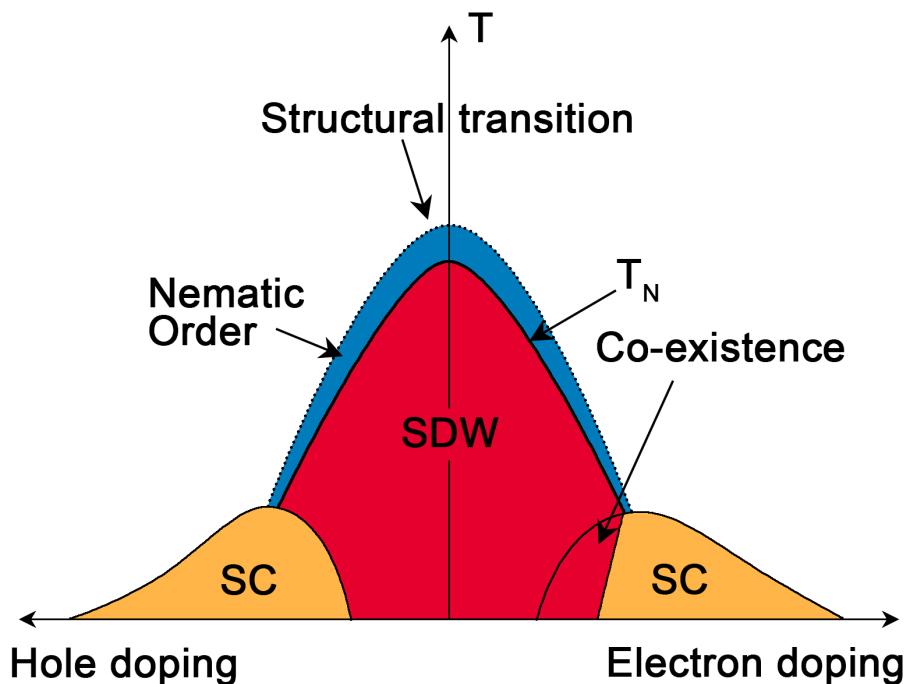
Fig. 1.2 Schematic phase diagram of iron pnictides on hole- or electron-doping. In the red region, the system shows a spin-density-wave (SDW) magnetic order. Upon doping, regions of superconducting (SC) order develop. Superconductivity can also be induced by applying pressure and/or isovalent chemical substitution. The nematic phase at $T > T_N$ is a subject of strong current interest for FeSCs, but is not a topic of focus in this thesis. (Figure adapted from [4, 5])

another common feature shared by the FeSCs is their proximity to an antiferromagnetic order. Fig. 1.2 shows a typical phase diagram for an FeSC. The undoped parent compound is usually an antiferromagnet. Superconductivity can be induced by suppressing this magnetic order in various ways. These include electron or hole doping [9], application of hydrostatic pressure [10], and isovalent substitution which creates "chemical pressure" [11].

Despite the very similar crystal structures exhibited by different FeSCs, there is a large variability in their electronic structures [12]. The electronic structures of FeSCs generally comprise several Fe d-bands near the Fermi energy, with small electron- and hole-like pockets, which are quite sensitive to external perturbations, such as pressure or chemical doping. The Fermi surfaces of iron pnictides typically consist of hole pockets in the middle of the Brillouin zone and electron pockets at the zone boundaries. But in several iron chalcogenides, only electron Fermi surfaces are present. Moreover, in the extremely hole-doped iron pnictides, such as KFe_2As_2, the electron Fermi surface at the zone-boundary is absent, and is instead replaced with tiny hole pockets.

It is widely believed that a phonon-mediated pairing mechanism in the original form of the BCS theory cannot account for the high T_c observed in many of the FeSCs. Determining the symmetry and structure of the superconducting order parameter, or in other words the superconducting energy gap function, in momentum space provides important clues for understanding the mechanism by which superconductivity arises. Although there is yet to be a first-principle microscopic theory that fully describes the origin of superconductivity in FeSCs, the majority of experiments support a spin-singlet s-wave state with sign-changing superconducting gaps on different part of the Fermi surfaces [5, 12]. In particular, a spin resonance has been observed by inelastic neutron scattering in a wide range of FeSCs below their superconducting transitions [13–15], implying that the superconducting gap $\Delta_{\mathbf{k}}$ has opposite signs at the hole pocket relative to the electron pockets, which have been taken as evidence for an $s^{\pm}$ gap structure. However, alternative pairing states have also been proposed, most notably for the heavily hole- and electron-doped systems where the low-energy electronic structures deviate most significantly from the weakly to moderately doped FeSCs. Theoretical studies have shown that the attractive electron interactions in the $d_{x^2-y^2}$ channel may have comparable strength to that in the $s^{\pm}$ channel [16], and in the electron-doped FeSCs, this can become the dominant superconducting instability. In d-wave superconductors, nodes are expected on the hole pockets due to symmetry, which gives rise to low-energy quasiparticle excitation and can be detected through thermodynamic and thermal transport measurements. Evidence for nodal gaps has been found in thermal conductivity measurements of the highly hole-doped superconductor KFe_2As_2 and was interpreted in favour of d-wave superconductivity [17, 18]. However, later ARPES measurements reported

an *s*-wave gap with eight line nodes on the intermediate hole band [19] and further heat capacity measurement have revealed qualitative agreement to the ARPES results by fitting the specific heat data to a self-consistent four-band model with *s*-wave gap functions [20]. Therefore the pairing state in KFe$_2$As$_2$ remains controversial.

The diverse electronic structures and potentially non-universal superconducting states of the FeSCs provide a useful testbed for different theories of pairing. The variability of superconducting properties of the different systems when tuned by doping or pressure allows the detailed refinements of material-specific theories. On the other hand, the apparent commonality between all iron-based superconductors, such as their structural similarities, strong electronic correlations and closeness to the border of magnetism, can provide important clues for the search for superconductors with higher T_c.

1.2 The layered iron germanide YFe$_2$Ge$_2$

Isostructural to the 122-family of FeSCs, the layered iron germanide YFe$_2$Ge$_2$ stands out from the commonly known FeSCs for not containing group-V and group-VI elements. The only other such example of layered FeSC is the recently discovered iron silicide LaFeSiH [21]. In 2014, Zou et al. reported the observation of superconductivity in YFe$_2$Ge$_2$ for the first time [22]. Full resistive transitions and partial DC diamagnetic screening of up to 80% were shown for polycrystalline YFe$_2$Ge$_2$ samples with residual resistivity ratio (RRR $= \rho_{300\,\text{K}}/\rho_{2\,\text{K}}$) reaching 50. Although the onset of superconductivity was observed at 1.8 K in resistivity (for a sample with RRR $= 41$), a complete transition was only reached at 0.6 K. Despite the high diamagnetic fraction, no signature of bulk superconductivity was observed for these samples in heat capacity measurements. Meanwhile, in this initial study, single crystals grown by flux method were reported to have a substantially lower RRR exhibiting only partial transitions even in resistivity measurements.

Following the initial report of superconductivity in YFe$_2$Ge$_2$, Kim et al. [24] at the Ames Laboratory carried out a systematic investigation into the growth of YFe$_2$Ge$_2$ single crystals using a Sn-flux method. In their study, they investigated the effects of varying the growth protocols, such as changing the decanting temperatures, and the effects of polishing and annealing on the sample properties. They found resistive superconducting transitions in samples with RRR ≈ 34. Their best samples had RRRs up to 65. However, similar to Zou's initial study on the polycrystals, none of their samples showed signatures of bulk superconductivity in heat capacity measurements. It was hence concluded that the observed superconductivity is either filamentary and strain-stabilised in small regions of the sample or from a secondary alien phase present at undetectable quantity. Similar doubt that
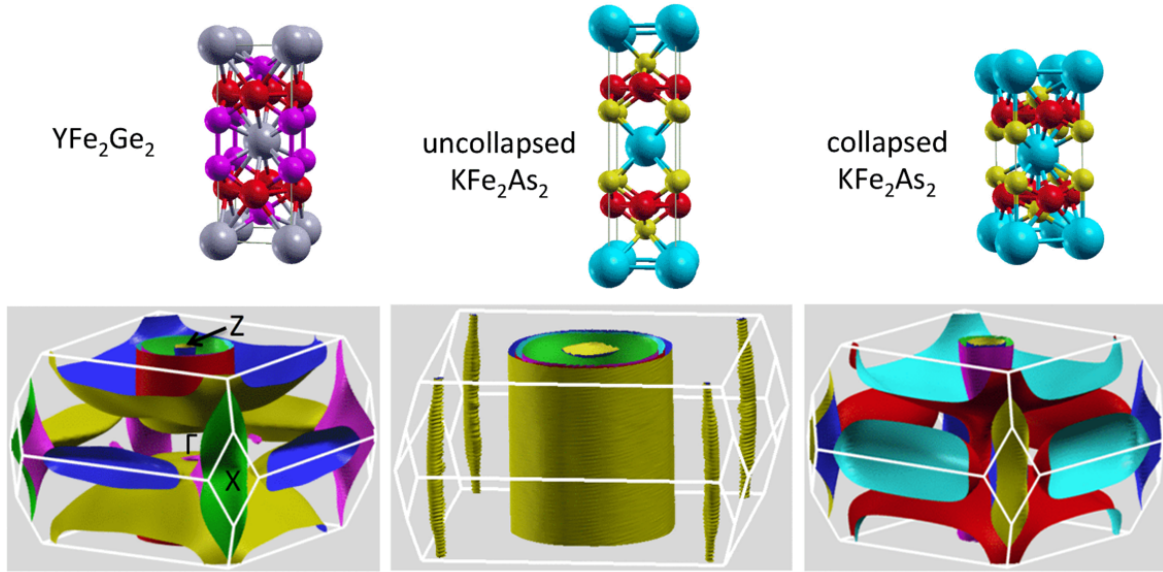
Fig. 1.3 Crystal structure and Fermi surface calculated within DFT for YFe_2Ge_2 and for KFe_2As_2 in the uncollapsed and collapsed tetragonal structure. (Figure credit: [23])

superconductivity was extrinsic to YFe_2Ge_2 also advanced in a later study [25]. The studies described in this thesis built on these initial investigations of superconducting properties in YFe_2Ge_2. As will be shown later in Chapter 4 and 5, conclusive evidence has been established for bulk superconductivity in YFe_2Ge_2 samples with RRR above about 70 [23, 26].

YFe_2Ge_2 shares key properties with the alkali metal iron arsenides $(K/Rb/Cs)Fe_2As_2$ [20, 30–32]: it has the same $ThCr_2Si_2$ structure, featuring square lattice iron layers, its low temperature heat capacity Sommerfeld coefficient is similarly enhanced, and antiferromagnetic order can be induced by chemical substitution [28]. There is an important difference, however: although YFe_2Ge_2 appears at first sight to be isoelectronic to the alkali metal iron arsenide superconductors, the existence of Ge-Ge bonds in YFe_2Ge_2, contrasting with the absence of As-As bonds in the arsenides, causes the Fe oxidation state to differ from that of the arsenides [25]. On the other hand, the calculated Fermi surface in YFe_2Ge_2 is very similar to that expected for KFe_2As_2 in the pressure-induced collapsed tetragonal phase (Fig. 1.3) [33].

While YFe_2Ge_2 is a paramagnet, its sibling compound $LuFe_2Ge_2$ exhibits an antiferromagnetic transition at $T_N \approx 9\,\mathrm{K}$ [34, 29]. In its ordered state, the iron moments are ferromagnetically ordered in the basal plane while coupling antiferromagnetically along the
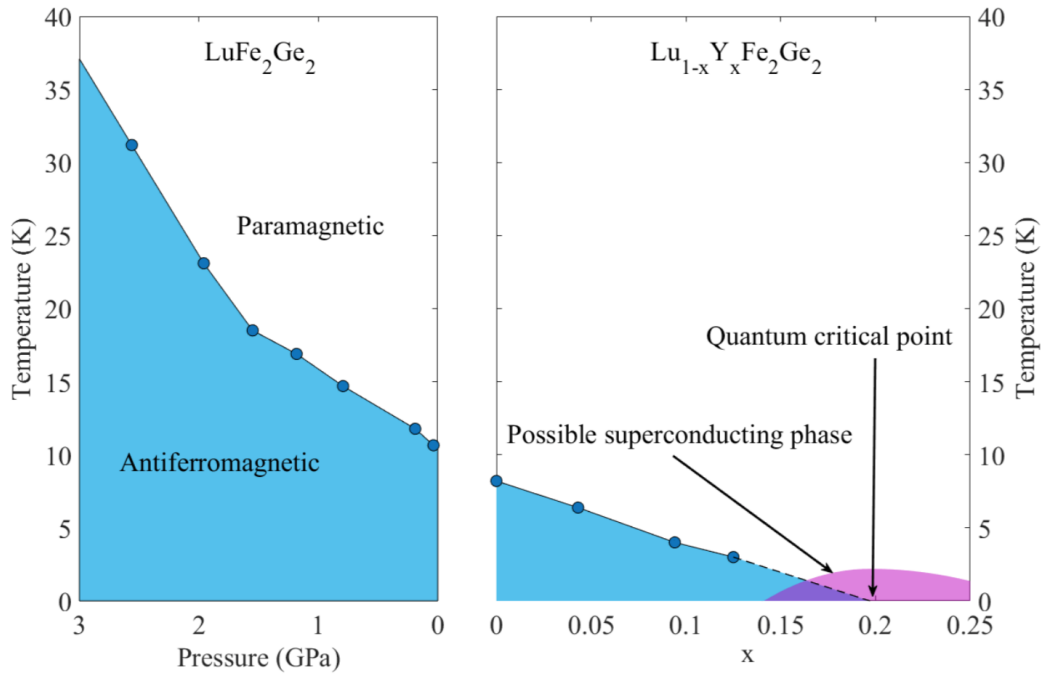
Fig. 1.4 Dependence of the magnetic transition temperature T_N of $LuFe_2Ge_2$ with hydrostatic pressure and of $Lu_{1-x}Y_xFe_2Ge_2$ with doping. (Figure credit: [27], data obtained from [28, 29])

c-direction. Hydrostatic pressure on $LuFe_2Ge_2$ was found to move the transition to higher temperatures [29], whereas another study revealed that substituting lutetium with yttrium leads to the suppression of T_N [28]. Fig. 1.4 summarises the effect of pressure and chemical substitution on T_N. When 20% of Lu are replaced by Y, the Néel temperature extroplates to zero. This suggests the potential occurrence of a quantum critical point (QCP), near which one may expect to find a dome of superconducting phase. However, no superconductivity has so far been detected near the critical composition down to $2\,K$, possibly because of strong disorder scattering.

    YFe_2Ge_2 further exhibits various interesting normal-state properties. Measurements of resistivity and heat capacity down to $2\,K$ were first reported in [34]. An unusually high Sommerfeld coefficient $C/T \approx 100\,mJ/molK^2$ was observed. This is around 8 times higher than the band-structure calculated value [22], indicating the presence of strong electronic correlations. In addition, the low-temperature resistivity of YFe_2Ge_2 shows an anomalous $T^{3/2}$ temperature dependence [22, 23], suggesting non-Fermi liquid behaviour.

After the initial discovery of superconductivity, density functional theory (DFT) studies put forward by Subedi [35] and Singh [36] suggested two potential scenarios for unconventional superconductivity in YFe_2Ge_2. Subedi argued that the presence of an electron pocket at the Brillouin zone corner and hole pockets near the zone centre favours antiferromagnetic spin fluctuations and an $s^{\pm}$ order parameter wave function. On the other hand, Singh put forward a more radical proposal: noting that magnetism with ordering wave vector (0, 0, 1/2) can be induced in YFe_2Ge_2 by alloying with isoelectronic Lu [28, 29], ferromagnetic correlations within the plane could induce a triplet superconducting state.

Although experimentally observed to be paramagnetic, YFe_2Ge_2 appears to be on the threshold of magnetism. DFT calculations [35, 36] indicated that various types of magnetic order, including a ferromagnetic order and antiferromagnetic orders with different wavevecotrs, all have energies lower than the non-spin-polarised state. Among the various magnetic states, the A-type order of the Fe atoms, same as that observed in $LuFe_2Ge_2$, was found to be the most favourable state according to the DFT studies. On the experimental side, X-ray absorption and photoemission studies have demonstrated the presence of large fluctuating Fe moments in YFe_2Ge_2 [37], also suggesting its closeness to the border of magnetism. Furthermore, a recent inelastic neutron scattering experiment [38] has revealed the presence of both ferromagnetic and antiferromagnetic in-plane fluctuations.

Despite having a relatively low transition temperature, YFe_2Ge_2 presents a special case of iron-based superconductors with a three-dimensional Fermi surface as a result of the Ge-Ge bonding. By comparing and contrasting the superconducting and normal state properties of YFe_2Ge_2 with other known iron-based superconductors, we can improve our understanding of the microscopic mechanism of the FeSC as a whole and possibly provide new directions for the search of superconductors with higher T_c, e.g. by exploring the nearby QCP.

1.3   Thesis layout

In Chapter 2, I start with a brief overview of the key theoretical concepts underpinning the experimental results discussed in the later chapters. These include theory of superconductivity, impurity effects in superconductors, the theory behind muon spin spectroscopy and the theory of de Haas-van Alphen effect. Chapter 3 describes the growth techniques employed for synthesising both poly- and single-crystal YFe_2Ge_2 and the range of experimental methods used to measure the physical properties of these crystals.

In Chapter 4, I present the results obtained during a systematic programme to optimise the growth parameters for synthesising high-quality, polycrystalline YFe_2Ge_2 samples. Thermodynamic, magnetic and transport measurements of these samples provided the first conclusive

evidence for bulk superconductivity in this compound. Potential causes of disorder, which is detrimental to superconductivity, are further discussed in light of results from both powder X-ray diffraction (XRD) and energy dispersive spectroscopy (EDS) measurements. Materials presented in this chapter have been published in [23, 26].

In Chapter 5, I describe the modified Sn-flux and the liquid transport methods which have allowed the growth of ultra-pure YFe_2Fe_2 single crystals with drastically improved sample quality. Samples grown with these methods have displayed RRRs up to 200 and 470, respectively. In the latter case, samples have shown notably sharper superconducting transitions than our best polycrystals. Beyond the initial sample characterisations, in the later sections of this chapter, I present results from low-temperature heat capacity, muon spin rotation and quantum oscillation measurements on these new generations of high-quality single crystals and discuss their implications for the superconducting pairing state and the electronic structure of YFe_2Ge_2.

Finally, in Chapter 6, a short summary is given where I discuss the broader relevance of the study on YFe_2Ge_2 for understanding the physics of FeSCs as a whole. I also provide possible future prospects of related projects going foreward.

Chapter 2

Theoretical concepts

2.1 Superconductivity

2.1.1 Ginzburg-Landau theory

Without going into details of the underlying microscopic mechanisms for the formation of a superconducting state, a phenomenological description given by the Ginzburg-Landau theory captures the key features of a superconducting phase transition. Near a phase transition from a normal state to a superconducting state, the free energy density can be expressed as an expansion of a complex order parameter $\psi = \sqrt{n_s}\exp(i\theta)$, where n_s is the superfluid density and θ gives the phase of the order parameter [39, 40]:

$$F = \alpha|\psi|^2 + \frac{\beta}{2}|\psi|^4 + \frac{1}{2m_s}|(-i\hbar\nabla - q_s\mathbf{A})\psi|^2 + \frac{|\mathbf{B}|^2}{2\mu_0}, \tag{2.1}$$

where α and β are constants, m_s is the superfluid mass, q_s is the superfluid charge, $\mathbf{A}$ is the magnetic vector potential, $\mathbf{B} = \nabla \times \mathbf{A}$ is the magnetic field, and μ_0 is the permeability of free space. Two Ginzburg-Landau equations are obtained by minimising the free energy with respect to ψ and $\mathbf{A}$:

$$\frac{1}{2m_s}(-i\hbar\nabla + q_s\mathbf{A})^2\psi + (\alpha + \beta|\psi|^2)\psi = 0, \tag{2.2}$$

$$\mathbf{J_s} = \frac{iq_s\hbar}{2m_s}(\psi^*\nabla\psi - \psi\nabla\psi^*) - \frac{q_s^2}{m_s}\mathbf{A}\psi^*\psi = -\frac{q_s n_s}{m_s}(\hbar\nabla\theta + q_s\mathbf{A}), \tag{2.3}$$

where J_s is the supercurrent density and ψ^* is the complex conjugate of ψ. These equations reveal two characteristic length scales [40], namely the penetration depth λ and the coherence length ξ, which are important for classifying the superconducting behaviour. λ is a measure

of how far the magnetic field can penetrate into a superconductor, while ξ is associated with the spatial variation of ψ.

Two classes of superconductors are defined according to the dimensionless Ginzburg-Landau parameter

$$\kappa = \frac{\lambda}{\xi}. \tag{2.4}$$

For $\kappa < 1/\sqrt{2}$, we have a "type-I" superconductor, in which magnetic flux is expelled under external applied field until superconductivity is suddenly destroyed at a single critical field B_c. When $\kappa > 1/\sqrt{2}$, we have a "type-II" superconductor where, instead of a sudden change from a Meissner state (which excludes magnetic flux completely) to a normal state, a vortex state with periodical arrangement of quantised magnetic flux lines is reached above a lower critical field B_{c1}. To destroy the vortex phase, an upper critical field B_{c2} is required.

2.1.2   BCS theory

The modern understanding of the microscopic mechanism of superconductivity started with the formalism proposed by Bardeen, Cooper and Schrieffer (BCS) [41]. They showed that an arbitrarily weak attractive interaction between electrons can result in the formation of a coherent many-body state which could be seen as a condensate of Cooper pairs. An energy gap Δ separates the excitations of this condensate from its ground state energy.

The formation of Cooper pairs, for example in an elemental superconductor, most commonly arises from an attractive interaction mediated through the vibrations of the ionic lattice (phonons). This can be understood in a classical picture as follows. An electron moving in a conductor will attract the nearby positively charged lattice ions, which due to their higher masses move slower than the electrons. It hence leaves behind a region with a larger density of positive charges. Another electron, with an opposite spin, is attracted to such a region, resulting in an effective attraction between the two electrons. This type of phonon-mediated superconductivity is often termed *conventional* superconductivity.

While a variational approach was used in the original BCS paper to derive the ground state properties, a self-consistent field method is more intuitive when dealing with excited states [40, 42]. In a second-quantised form, the pairing Hamiltonian can be expressed as:

$$H = \sum_{\mathbf{k}\sigma} \varepsilon_{\mathbf{k}} c_{\mathbf{k}\sigma}^{+} c_{\mathbf{k}\sigma} + \sum_{\mathbf{k}l} V_{\mathbf{k}l} c_{\mathbf{k}\uparrow}^{+} c_{-\mathbf{k}\downarrow}^{+} c_{-l\downarrow} c_{l\uparrow} \tag{2.5}$$

$$\approx \sum_{\mathbf{k}\sigma} \varepsilon_{\mathbf{k}} c_{\mathbf{k}\sigma}^{+} c_{\mathbf{k}\sigma} + \sum_{\mathbf{k}l} V_{\mathbf{k}l} (c_{\mathbf{k}\uparrow}^{+} c_{-\mathbf{k}\downarrow}^{+} b_l + b_{\mathbf{k}}^{*} c_{-l\downarrow} c_{l\uparrow} - b_{\mathbf{k}}^{*} b_l), \tag{2.6}$$

where $c_{\mathbf{k}\sigma}^{+}$ and $c_{\mathbf{k}\sigma}$ are electron creation and annihilation operators with wavevector $\mathbf{k}$ and spin σ, $\varepsilon_{\mathbf{k}}$ is the single-particle energy relative to the Fermi energy, $V_{\mathbf{kl}}$ is the scattering amplitude between a state with $(\mathbf{l}\uparrow, -\mathbf{l}\downarrow)$ to one with $(\mathbf{k}\uparrow, -\mathbf{k}\downarrow)$. The second equation is obtained by substitution of $b_{\mathbf{k}} = \langle c_{-\mathbf{k}\downarrow} c_{\mathbf{k}\uparrow}\rangle_{avg}$ and neglecting small fluctuation terms. An energy gap function is defined as:

$$\Delta_{\mathbf{k}} = -\sum_{\mathbf{l}} V_{\mathbf{kl}} b_l = -\sum_{\mathbf{l}} V_{\mathbf{kl}} \langle c_{-\mathbf{l}\downarrow} c_{\mathbf{l}\uparrow}\rangle. \tag{2.7}$$

By diagonalising Eq. 2.6 using a Bogoliubov transformation and solving the equation using the BCS coherent ground state, we arrive at the energy spectrum of the excited states:

$$E_{\mathbf{k}} = \sqrt{\varepsilon_{\mathbf{k}}^2 + |\Delta_{\mathbf{k}}|^2}, \tag{2.8}$$

where the energy gap function can be determined by the self-consistent equation:

$$\Delta_{\mathbf{k}} = -\frac{1}{2}\sum_{\mathbf{l}} \frac{\Delta_{\mathbf{l}}}{\sqrt{\varepsilon_{\mathbf{l}}^2 + |\Delta_{\mathbf{l}}|^2}} V_{\mathbf{kl}}. \tag{2.9}$$
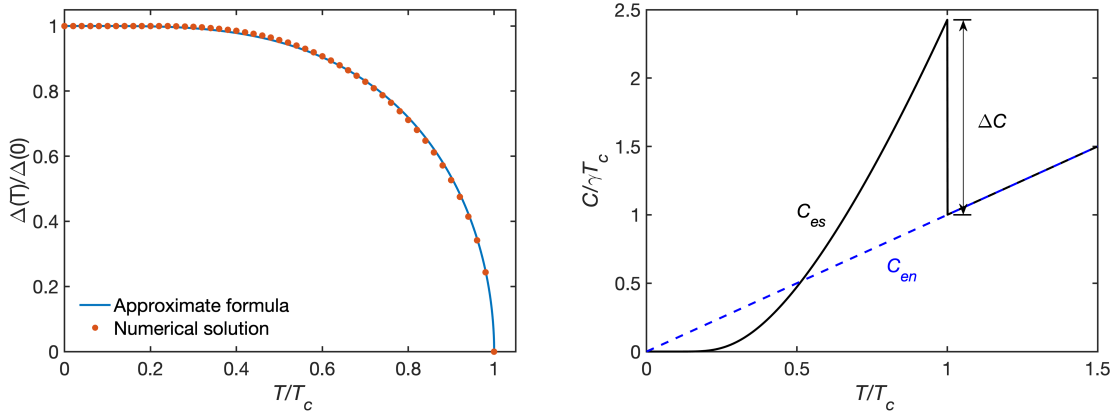
Fig. 2.1 (Left panel) The temperature dependence of the BCS gap function obtained from numerical solution to Equ. 2.13 (red solid dots) [43] and the approximate formula Equ. 2.15 (blue line). (Right panel) Comparision between superconducting (C_{es}) and normal (C_{en}) state electronic heat capacity of a BCS-type superconductor. A jump in the heat capacity ΔC occurs at the transition from normal to superconducting state.

In the BCS theory, the approximation $V_{\mathbf{kl}} = -V$ is taken for $\mathbf{k}$ and $\mathbf{l}$ states out to a cutoff energy $\hbar\omega_c$ away from the Fermi energy E_F, whereas beyond $\hbar\omega_c$ $V_{\mathbf{kl}}$ is taken to be zero. We hence find that the energy gap function satisfies

$$\Delta_{\mathbf{k}} = \begin{cases} \Delta, & \text{for } |\varepsilon_{\mathbf{k}}| < \hbar\omega_c \\ 0, & \text{for } |\varepsilon_{\mathbf{k}}| > \hbar\omega_c \end{cases}. \tag{2.10}$$

Replacing the summation in Equ. 2.9 by an integration from $-\hbar\omega_c$ to $\hbar\omega_c$, and noting the symmetry between $\pm\varepsilon$, we get

$$\frac{1}{N(0)V} = \int_0^{\hbar\omega_c} \frac{d\varepsilon}{\sqrt{\Delta^2 + \varepsilon^2}} = \sinh^{-1}\frac{\hbar\omega_c}{\Delta} \tag{2.11}$$

and hence

$$\Delta = \frac{\hbar\omega_c}{\sinh[1/N(0)V]} \approx 2\hbar\omega_c e^{-1/N(0)V} \tag{2.12}$$

where $N(0)$ denotes the density of state at the Fermi level for electrons of one spin orientation, and the last step is justified in the weak-coupling limit where the dimensionless electron-phonon coupling parameter, $\lambda_{ep} = N(0)V \ll 1$.

At finite temperatures, we have to consider the quasiparticle excitations and their probability distribution. The temperature dependence of the BCS gap function, $\Delta(T)$, can be calculated by solving the self-consistent equation [40]

$$\frac{1}{N(0)V} = \int_0^{\hbar\omega_c} d\varepsilon \frac{1}{\sqrt{\varepsilon^2 + |\Delta(T)|^2}} \tanh\left(\frac{\sqrt{\varepsilon^2 + |\Delta(T)|^2}}{2k_BT}\right). \tag{2.13}$$

In the limit $T \to 0$,

$$\Delta(0) = 1.764 k_B T_c. \tag{2.14}$$

While the BCS gap function can be solved numerically from Equ. 2.13, an approximation to the solution exists which can be written as

$$\Delta(T) = 1.76 \tanh\left\{1.82[1.018(\frac{T_c}{T} - 1)]^{0.51}\right\}. \tag{2.15}$$

The temperature dependence of the BCS gap function, $\Delta(T)$ is shown in Fig. 2.1. The presence of the energy gap causes a modification to the electronic specific heat from its normal state value. As a result, the electronic specific heat diminishes exponentially at lowest temperatures, while a jump in specific heat of $\Delta C(T_c) = 1.43 C_{en}(T_c)$, where C_{en} is the normal state electronic specific heat, is expected at $T = T_c$ (Fig. 2.1).

A popular empirical model adapted from the BCS theory is the α-model of supercon-
ductivity [44]. By allowing the value of the zero temperature energy gap, $\Delta(0)$ to be a
variable, with $\alpha \equiv \Delta(0)/k_B T_c$ and assuming the normalised form of the superconducting
order parameter $\Delta(T)/\Delta(0)$ from the BCS theory, the α-model can be used to fit the mea-
sured electronic heat capacity versus temperature to quantify the magnitude of any deviation
from the BCS theory. For example, in superconductors where the discontinuous increase at
transition temperature $\Delta C_e(T_c) > 1.43 \gamma_n T_c$, a value of $\alpha > \alpha_{BCS} = 1.764$ may be obtained
which is viewed as a sign for strong coupling.

2.1.3 Destruction of superconducting state by magnetic field

In a type-II superconductor, superconductivity is destroyed as magnetic field is increased
above the upper critical point B_{c2}. This process can happen in two ways: either the gradual
increase of the density of magnetic flux lines causes the normal state regions of the vortex
cores to overlap, or the Zeeman-splitting between the up- and down-spin electrons becomes
so great that it destroys electron pairing. The former effect is termed 'orbital limiting' and
the latter 'Pauli limiting'.

The orbital limiting process is modeled by Werthamer, Helfand and Hohenber (WHH)
[45], where the zero-temperature limit of the orbital limited upper critical field at critical
temperature T_c is given by:

$$B_{c2}^{(O)}(0) = \delta T_c |dB_{c2}/dT|_{T_c},$$ (2.16)

where δ is a numerical factor which takes on the value 0.69 in the dirty limit (mean free path
$l \ll \xi$) or 0.73 in clean limit ($l \gg \xi$).

In the Pauli limiting case, the critical field B_{c2}^P results from the balancing between the
Zeeman energy of the normal state and the superconducting state condensation energy [46]
which gives:

$$B_{c2}^{(P)} = (2g\mu_0)^{-1/2} \frac{\Delta_0}{\mu_B} = 1.84 T_c (\mathrm{T\,K^{-1}})$$ (2.17)

for a BCS superconductor, where μ_B is the Bohr magneton and g is the Lande g factor.

2.1.4 Unconventional superconductivity

In the BCS theory, the gap function $\Delta_{\mathbf{k}}$ is assumed to be isotropic in momentum space. The
Cooper pairs responsible for superconductivity are bound states of electrons with opposite
spins, giving an angular momentum $l = 0$, and the attractive interactions between the electrons
are phonon-mediated. Soon after the proposal of the BCS theory, it was realised that, by
fully accounting for both the charge and spin degrees of freedom of the electron, attractive

components of the effective interaction between electrons can arise even in the absence of lattice vibrations. In these *unconventional* superconductors, the driving force for electron pairing may come from the more direct electronic interactions, e.g. from exchange of excitations corresponding to spin fluctuations. Unlike the phonons, which are typically limited to low energies, the strong interactions of the electron spin degrees of freedom can reach energies up to several thousand Kelvins. While the microscopic mechanisms behind conventional superconductivity have been successfully formulated by the BCS theory, no equivalent first-principle microscopic theory exists for unconventional superconductivity, due to difficulties in dealing with the inherently strong correlations involved.

As described in Section 2.1.2, electron pairings in conventional superconductors rely on the retardation effects due to the slow motions of the lattice ions. Electronic fluctuations, in the contrary, occur on the same time scales as the electron motions. In unconventional superconductors, to partially negate the effects of Coulomb repulsion, electrons therefore avoid each other in space rather than in time. As a result, pairing correlations develop between electrons from different sites and the orbital part of the superconducting order parameter, namely the superconducting gap function, tends to be orthogonal to the conventional s-wave type. In momentum space, the gap functions tend to be highly anisotropic and sign change can often occur resulting in gap nodes at certain positions on the Fermi surface. Determining the symmetry and structure of the gap function in momentum space is thus often the first step in identifying an unconventional superconductor. It also provides important clue regarding the superconducting pairing mechanism.

Examples of known unconventional superconductors include Sr_2RuO_4 (assumed to adopt a p-wave pairing state [47]), the iron-based superconductors (generally thought to have an $s^{\pm}$-wave state [16]), the cuprates (with a $d_{x^2-y^2}$ pairing symmetry [48]) and a range of heavy-fermion superconductors [49]. In many iron-based superconductors, despite most likely having an s-wave gap state, sign changes of the order parameter can occur between the different Fermi surfaces thanks to its multi-band nature. This is analogous to the isotropic, single-band $d_{x^2-y^2}$ state in the cuprates, except that the sign changes do not occur on the same band.

2.2 Multiband superconductivity

BCS theory describes a single-band superconductor, in which all the electrons on the isotropic Fermi surface contribute equally to the superconducting pairing, resulting in a constant superconducting gap Δ. However, when the FS of a material contains multiple sheets associated with different bands, different scenarios may occur, where each band develops its

own gap. The simplest form of multiband superconductivity occurs, when the electrons on the different bands experience different electron-phonon coupling strengths, giving rise to superconducting energy gaps of different sizes on the different bands.

The general BCS gap equation for a multiband system with intra- and inter-band interactions $V_{\mu\nu}(\mathbf{k},\mathbf{k}')$ is

$$\Delta_\mu(\mathbf{k}) = -\sum_{\mathbf{k}'\nu} V_{\mu\nu}(\mathbf{k},\mathbf{k}') \frac{\Delta_\nu(\mathbf{k}')}{2E_{\nu\mathbf{k}'}} \tanh \frac{E_{\nu\mathbf{k}'}}{2T} \tag{2.18}$$

$$\simeq -\sum_\nu \lambda_{\mu\nu}\Delta_\nu \int_0^{\hbar\omega_c} d\varepsilon \frac{1}{\sqrt{\varepsilon^2+\Delta_\nu^2}} \tanh\left(\frac{\sqrt{\varepsilon^2+\Delta_\nu^2}}{2k_B T}\right) \tag{2.19}$$

where μ, ν are band indices, and the quasiparticle energy $E_{\nu\mathbf{k}} = \sqrt{\varepsilon_{\nu\mathbf{k}}^2 + \Delta_{\nu\mathbf{k}}^2}$, with $\varepsilon_{\mathbf{k}}$ the single-particle dispersion measured with respect to the Fermi energy. In the second equation above, constant density of states N_ν for each Fermi surface sheet ν and isotropic interactions $V_{\mu\nu}$ are assumed, and the dimensionless interaction matrix $\lambda_{\mu\nu} = V_{\mu\nu}N_\nu$. Generally, due to the presence of inter-band coupling, all bands display the same transition temperature. The temperature dependence of the order parameters on the different bands is determined from the different inter- and intra-band coupling constants, $\lambda_{\mu\nu}$. The typical temperature dependence of the gap functions of a two-band superconductor for various inter-band coupling strengths is illustrated in Fig. 2.2.
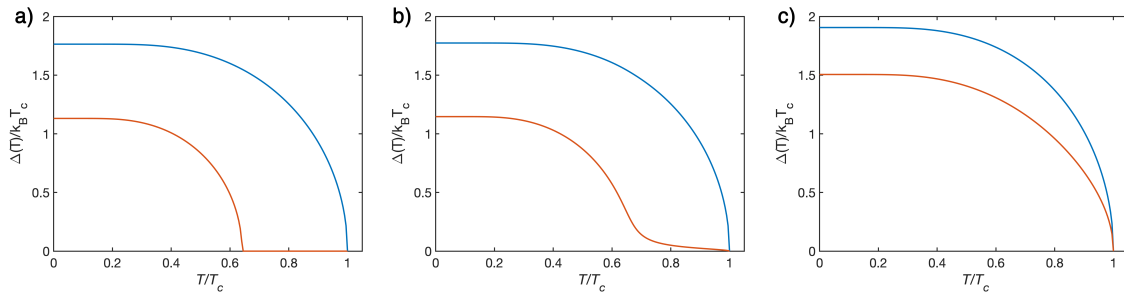
Fig. 2.2 Superconducting gap functions for a two-band superconductor with (a) weak, (b) intermediate and (c) relatively strong inter-band coupling. The blue and red lines represent the larger and the smaller gaps, respectively.

Specific heat

Knowing the temperature dependence of the superconducting gap function $\Delta(T)$, thermodynamic properties, such as entropy S and specific heat C, can be calculated as for a system of independent fermion quasiparticles [50]:

$$\frac{S}{\gamma_n T_c} = -\frac{6}{\pi^2}\frac{\Delta(0)}{k_B T_c}\int_0^\infty [f\ln f + (1-f)\ln(1-f)]\mathrm{d}y, \tag{2.20}$$

$$\frac{C}{\gamma_n T_c} = t\frac{\mathrm{d}(S/\gamma_n T_c)}{\mathrm{d}t} \tag{2.21}$$

where $f = [1+\exp(\frac{E}{k_B T})]^{-1}$ is the Fermi-Dirac distribution function and $t = T/T_c$. The energy of the quasiparticles is given by $E = \sqrt{\varepsilon^2 + \Delta(t)^2}$, and the integration variable $y = \varepsilon/\Delta(0)$. For a multi-band system, the contributions from each band can be summed up to obtain the total specific heat, in which each band is characterised by a partial Sommerfeld coefficient γ_i with $\gamma_1 + \gamma_2 = \gamma_n$.

The reverse procedure can also be used where the experimentally measured specific heat data is fitted to infer information regarding gap functions. For practical purposes, the empirical α-model [51] can often be used to simplify the fitting of experimentally measured heat capacity data. In a two-gap superconductor, by assuming the temperature dependence of the normalised BCS gap $\delta(t) = \Delta(t)/\Delta(0)$ for both gaps, the ratios of $2\Delta_i(0)/k_B T_c$ are then considered to be fitting parameters, together with the ratio of the partial Sommerfeld coefficients γ_1 and γ_2. More realistic calculations can be performed where the influence of inter-band interaction is taken into account and the gap functions are solved self-consistently rather than assumed to be of the BCS phenomenological form [20].

Penetration depth

In a two-gap model [52, 53], the temperature dependence of the penetration depth may be written as

$$\frac{\lambda^{-2}(T)}{\lambda^{-2}(0)} = \omega\frac{\lambda^{-2}(T,\Delta_{0,1})}{\lambda^{-2}(0,\Delta_{0,1})} + (1-\omega)\frac{\lambda^{-2}(T,\Delta_{0,2})}{\lambda^{-2}(0,\Delta_{0,2})} \tag{2.22}$$

where $\lambda^{-2}(0)$ and $\Delta_{0,i}$ are is the values of the penetration depth and the i-th ($i = 1$ or 2) superconducting gap at $T = 0\,\mathrm{K}$, respectively, and ω is a weighting factor denoting the relative contribution of the two bands.

Each term in Equ. 2.22 is evaluated using the standard expression within the local London approximation [54]

$$\frac{\lambda^{-2}(T,\Delta_{0,i})}{\lambda^{-2}(0,\Delta_{0,i})} = 1 + \frac{1}{\pi} \int_0^{2\pi} \int_{\Delta(T,\phi)}^{\infty} \frac{(\frac{\partial f}{\partial E})E}{\sqrt{E^2 - \Delta_i(T,\phi)^2}} dE d\phi \qquad (2.23)$$

where $\Delta_i(T,\phi) = \Delta_{0,i}\delta(T/T_c)g(\phi)$ and $g(\phi)$ gives the angular dependence of the gap. $\delta(T/T_c) = \tanh\left\{1.82[1.018(T_c/T - 1)]^{0.51}\right\}$ is again an approximation to the temperature dependence of the gap function in the BCS form. For s-wave and $s + s$-wave gaps $g(\phi)$ is 1, whereas for a d-wave gap it is $|\cos(2\phi)|$.

2.3   Impurity effects in superconductors

Real materials inevitably contain impurities and lattice defects. According to Anderson's theorem [56], non-magnetic impurities in a BCS superconductor have a negligible effect on T_c due to time-reversal invariance. In contrast, magnetic impurities are known to strongly suppress both T_c and the superconducting energy gap $\Delta(0)$ in a singlet s-wave superconductor. The dependence of T_c on the scattering rate Γ has been derived by Abrikosov and Gor'kov using the Green's function method [57] (see also later in Section 4.3).

Anderson's theorem requires the pair potential to be varying only weakly in momentum space, which is violated in unconventional superconductors with a higher orbital momentum pairing state, such as in a d–wave superconductor. The pair-breaking theory was later generalised [58, 59] and non-magnetic impurities were shown to act also as pair-breakers in an unconventional superconductor just as magnetic impurities in a s-wave superconductor. The $s^{\pm}$-wave superconducting state, having sign-changing order parameters, is also expected to have a similar T_c-suppression rate with point-like defects as in the d-wave case [60, 61].
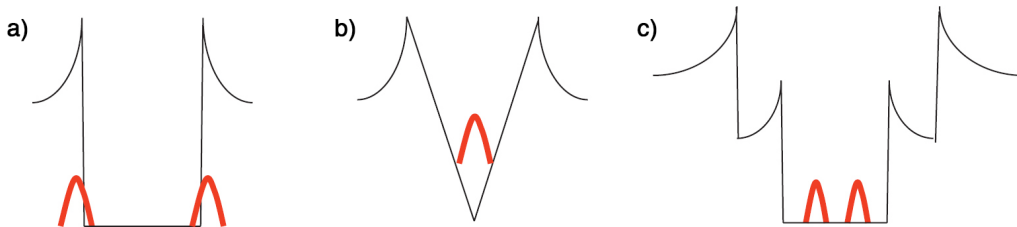
Fig. 2.3   Schematic illustrations of the impurity bound states (red lines) in (a) s-wave, (b) d-wave and (c) $s^{\pm}$-wave states. (Figure credit: [55])
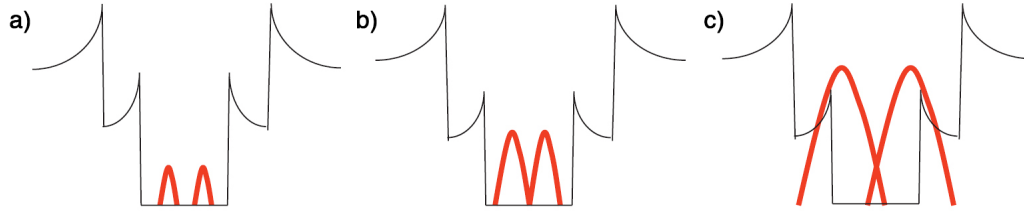
Fig. 2.4 Systematic evolution of the impurity bound states (red lines) in the $s^{\pm}$-wave state with an increasing impurity concentration n_{imp} relative to the critical value n_{imp}^{crit}, from (a) $n_{imp} < n_{imp}^{crit}$, (b) $n_{imp} = n_{imp}^{crit}$ to (c) $n_{imp} > n_{imp}^{crit}$. (Figure credit: [55])

Understanding of the effect of impurity scattering in superconductors was further extended by considering $\mathcal{T}$-matrix theory [62, 63]. In the low-density limit of impurity concentration, the $\mathcal{T}$-matrix theory includes certain multiple scattering process to infinite order. This enables the prediction of material properties with impurity scattering in the strong coupling (unitary) limit, capturing the physics of the impurity resonance, which is not possible when weak coupling (Born) approximation is assumed. The $\mathcal{T}$-matrix theory of impurity scattering has been successfully applied to different classes of unconventional superconductors, such as the heavy-fermion, high-T_c cuprate and iron-base superconductors [55, 62, 63].

Fig. 2.3 shows schematic diagrams of the impurity bound states for three different superconducting states with non-magnetic unitary impurities [55]. In a conventional s-wave superconductor, an in-gap state is not induced by non-magnetic impurities, so there is little change of the superconducting properties. In contrast, in a d-wave superconductor, Fig. 2.3(b) shows the formation of a bound state at zero energy. In the presence of a finite density of non-magnetic impurities, this in-gap state forms an impurity band leading to a finite density of state around zero energy. The accurate prediction of superconducting properties with increasing impurity level has played an important role in understanding the puzzling experimental results in heavy-fermion superconductors and the cuprates and in identifying the d-wave gap symmetry [62, 63]. Qualitatively, the effect of impurities on the $s^{\pm}$-wave superconductor can be understood as an intermediate case between the s-wave and the d-wave superconductors (e.g. Fig. 2.3(c)) [55].

Fig. 2.4 illustrates how the impurity band evolves in an $s^{\pm}$-wave superconductor. With a small amount of impurity, the low-energy density of state (DOS) of the system remained gapped. As the concentration of impurity increases through a critical value $n_{imp} = n_{crit}$, the bound state DOS develops into a V-shape. Thermodynamically, this is similar to the d-wave DOS. Eventually, at high impurity concentration, the impurity bound states show a finite $N_{imp}(0)$+V-shape DOS. Therefore, the presence of these impurity bound states
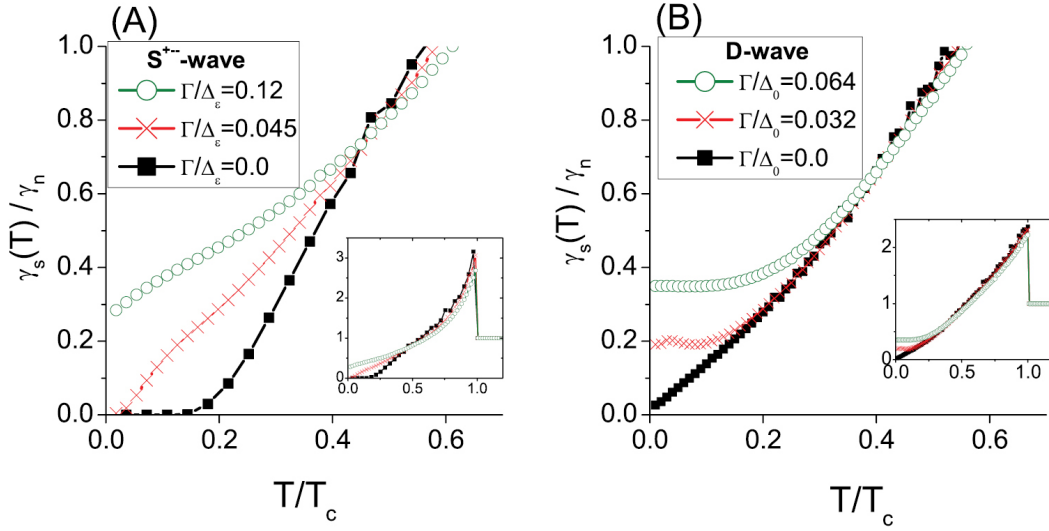
Fig. 2.5 Normalised specific heat coefficient $\gamma_s(T)/\gamma_n$ calculated for the $s^{\pm}$-wave and d-wave superconductors with various impurity scattering rates Γ. (a) The two-band $s^{\pm}$-wave case for $\Gamma/\Delta_e = 0, 0.045$ and 0.12, $2\Delta_e/T_c = 7.5$ and $|\Delta_e/\Delta_h| = 2.5$, where Δ_e and Δ_h are the gap sizes at zero temperature for the hole and electron band respectively. (b) The d-wave case for $\Gamma/\Delta_0 = 0, 0.032$ and 0.0064, where $\Delta_0 = 10T_c$ is the maximum amplitude of the gap at zero temperature. (Figure credit: [55])

can, above certain concentrations, significantly alter the physical properties of an $s^{\pm}$-wave superconductor at low temperatures. For example, Fig. 2.5 shows the theoretical calculations of the normalised specific heat coefficients $\gamma_s(T)/\gamma_n$ for the $s^{\pm}$-wave and d-wave cases under varying impurity scattering rates Γ. In the clean limit of $\Gamma/\Delta = 0$, the $s^{\pm}$-wave superconductor shows the usual exponential behaviour as in a conventional s-wave superconductor while a linear-T dependence is observed in the d-wave case. However, with increasing impurity scattering above the critical level, $\gamma_s(T)/\gamma_n$ in the $s^{\pm}$-wave develops a T-linear behaviour at low temperature. By contrast, in the d-wave superconductor a flat T-dependence is observed. Such non-trivial and distinct developments of the low-temperature thermodynamic properties provide a means of discerning the two gap states through experimental investigations.

2.4 Theory of muon spin relaxation spectroscopy

Muon spin spectroscopy is commonly abbreviated as μSR, which stands for muon spin rotation, relaxation or resonance, with R corresponding to the specific application of the muon. Being charged spin-$\frac{1}{2}$ particles with magnetic moments around 3.18 times larger than

those of protons, muons can be an extremely sensitive microscopic probe of magnetism. Although they have the same magnitude of charge and spin as an electron, muons are about 207 times heavier than electrons. In condensed matter physics, positive muons (μ^+s) rather than negative muons (μ^-s) are mainly used for material investigations, because μ^-s tend to be attracted by the atomic nuclei in the host materials while μ^+s avoid them so they can sit at interstitial positions in the crystal structure.

To produce low energy muons (4.1 MeV) for μSR experiments, high-energy protons (produced in a synchrotron) collide with a light target (e.g. graphite or beryllium) and produce pions (π^+s) which are at rest in the surface layer of the target via

$$p + p \rightarrow \pi^+ + p + n. \tag{2.24}$$

The decay of π^+ then produces μ^+ via

$$\pi^+ \rightarrow \mu^+ + \nu_\mu, \tag{2.25}$$
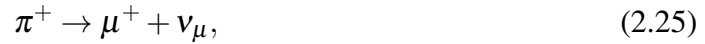
where ν_μ is a muon-neutrino.

Parity violation in the weak interaction ensures that the μ^+ has its spin pointing along the opposite direction of its momentum, resulting in a perfectly spin-polarised beam of low-energy μ^+s. This feature is one of the key prerequisites of the μSR technique. These μ^+s are then implanted in pulses into the bulk of the material. They lose their kinetic energy through ionisation of atoms, scattering of electrons, and Muonium formation over a timescale of a few nanoseconds.

Once implanted, the μ^+ experiencing the local magnetic field will precess about the field direction until it decays via

$$\mu^+ \rightarrow e^+ + \nu_e + \bar{\nu}_\mu \tag{2.26}$$

The probability of this decay is proportional to $\exp(-t/\tau_\mu)$, where $\tau_\mu = 2.2\,\mu$s is the lifetime of the muon. In this three-body decay, the decay positrons can be emitted with a spectrum of different energies and momenta. Weak interaction conserves parity and results in the emitted positrons emerging predominantly along the direction of the muon spin, with an angular distribution given by the probability function

$$P(\phi) \propto 1 + A\cos(\phi) \tag{2.27}$$

where ϕ is the angle between the direction of the muon spin and that of the positron momentum. The parameter A describes the asymmetry, which increases monotonically with the energy of the emitted positron.
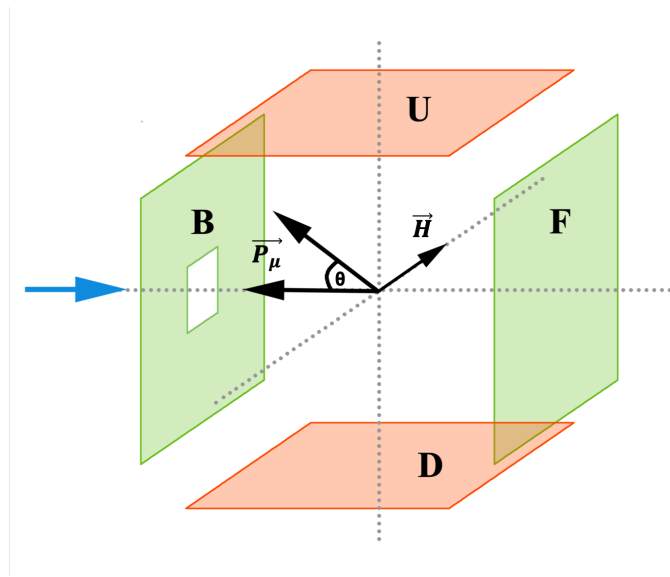
Fig. 2.6 Detector groupings for TF-μSR experiment. The muon spin initially points towards the B detector, and a magnetic field is applied along the y-axis. The spin vector precesses in the x-z plane, and the detectors are grouped into the BUFD directions, where the BF pair monitors the spin polarisation in the z direction, and the UD pair monitors the polarisation in the x direction.

It is the positrons which are detected in the μSR measurements, and the orientation of the positron spin encodes the information about the orientation of the muon spin when it decays. While a single positron decay cannot reveal the direction of the muon spin, by measuring the anisotropic distribution of the decay positrons from a collection of muons implanted under the same conditions, it is possible to calculate the statistical average of the spin-polarisation direction of the muon ensemble. Experimentally, this distribution of positrons is detected using scintillation detectors placed around the sample.

Various configurations of μSR experiments exist depending on the direction of the applied magnetic field. Here we will only describe the transverse field Muon spin rotation (TF-μSR), which is typically used for studying the vortex phase of type-II superconductors. For further information on the other μSR techniques, the reader is referred to the following references: [64–66].

In the transverse field (TF) configuration, the experiment is carried out with an external field applied perpendicular to the initial direction of the muon spin polarisation. Fig.2.6 shows a schematic diagram of this configuration. In the applied field, the spin of the muon which has settled at an interstitial site in the lattice precesses about the field direction with
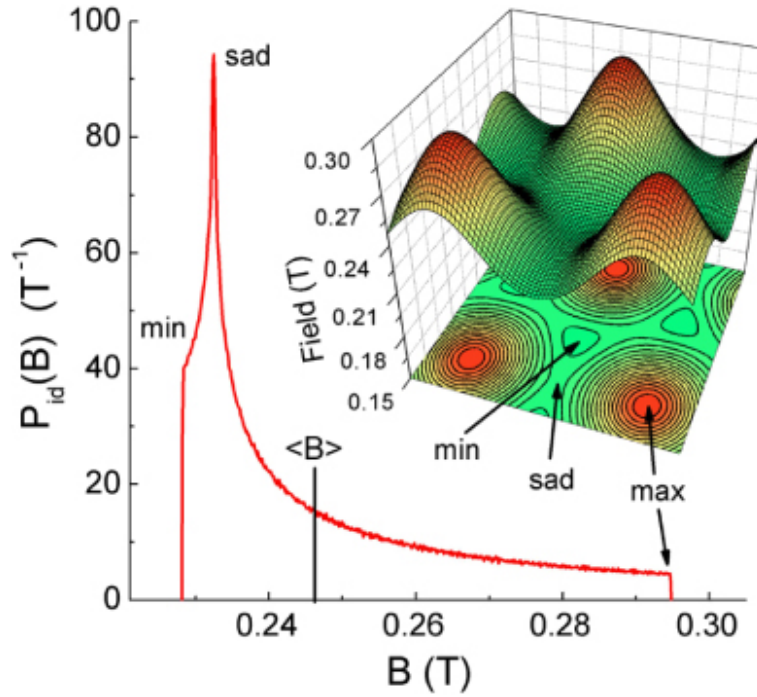
Fig. 2.7 The typical spatial distribution function of magnetic field $B(r)$ and the corresponding local magnetic field distribution $P_{id}(B)$ in a vortex lattice. (Figure credit: [67])

a frequency proportional to the strength of the field at the local site in the material. If the internal field profile of the material is uniform, the implanted muons will retain polarisation over the course of a measurement, as the presence of a transverse magnetic field cause the spins to all precess at the same Larmor precession frequency

$$\omega_\mu = \gamma_\mu B, \tag{2.28}$$

where $\gamma_\mu/2\pi = 135.5342\,\text{MHz/T}$ is the muon gyromagnetic ratio. On the other hand, if there exists a significant site-to-site field variation, the muon ensemble will progressively become depolarised. By observing this depolarisation and measuring the precession rate, the profile of the internal magnetic field may be inferred.

Information regarding the depolarisation of the muon spins can be detected using the time-dependence of the asymmetry of the muon ensemble, which is in turn extracted by grouping the positron detectors into appropriate directions (e.g. BFUD for TF geometry as shown in Fig 2.6) and summing the counting histograms from the detectors in each group. As an example, here we consider the B and F groups. The number of counts $N_{B,F}$ detected in

the B or F detectors will be given in general by

$$N_B = N_0 \exp(-\frac{t}{\tau_\mu})(1 + A_0 G_Z(t)) \tag{2.29}$$

$$\alpha N_F = N_0 \exp(-\frac{t}{\tau_\mu})(1 - A_0 G_Z(t)) \tag{2.30}$$

where α measures the relative efficiencies between the F and B detectors, $A_0 = A(t = 0)$ is the initial asymmetry assumed to be the same for each set of detectors, N_0 is a constant which normalises the equation, and $G_Z(t)$ is the (unknown) time evolution of the muon polarisation along the field direction. The term $A_0 G_Z(t)$ is called the asymmetry function and contains information about the magnetic environment in the sample of interest. The decay of muons is described by the exponential term.

The experimental asymmetry $A(t)$ can then be calculated by combining the equations of N_B and N_F:

$$A(t) = A_0 G_Z(t) = \frac{N_B(t) - \alpha N_F(t)}{N_B(t) + \alpha N_F(t)}. \tag{2.31}$$

In a type-II superconductor, under an applied magnetic field ($B_{c1} < B \ll B_{c2}$) the shape of the asymmetry function $A(t)$ in the TF configuration is primarily influenced by two effects: (1) Precession of spins due to the applied magnetic field gives a sinusoidal time dependence; (2) Additional effects come from magnetic vortices and nuclear magnetic moments, which create a spatially inhomogeneous local field, causing the muon spins to become depolarised. If the probability distribution of the z-component of the local magnetic field within the sample is p(B_z), then we can write the net polarisation of the muon spin as

$$P_x(t) \propto \int p(B_z)\cos(\gamma_\mu B_z t + \phi) \mathrm{d}B_z, \tag{2.32}$$

where ϕ is the initial phase given by the initial polarisation of spins. This equation shows that $P_x(t)$ and $p(B_z)$ are related by a Fourier transform. Fig. 2.7 shows the typical shape of the distribution of magnetic field strength in the vortex phase under a low external field. Oftentimes, the external field applied in a TF-μSR experiment is high enough that $p(B_z)$ can be approximated as a Gaussian distribution. This allows us to describe the polarisation function $P_x(t)$ as a product of a cosine and a Gaussian component:

$$P_x(t) \propto \exp(-\sigma^2 t^2/2)\cos(\gamma_\mu \langle B_z \rangle t + \phi), \tag{2.33}$$

where $\langle B_z \rangle$ is the average magnetic field strength in z direction at the muon site and σ is the muon spin depolarisation rate.

Different regions exist in a sample in which muons experience different local environment, it may be possible to fit the polarisation function as a sum of the given functions with different σ and $\langle B_z \rangle$. In a non-superconducting phase, the depolarisation rate, σ_n will be mostly determined by the nuclear magnetic moments and can be regarded as temperature-independent. This may be the case if the sample is mounted on a silver sample holder with part of the silver surface exposed to the muon beam. The muons implanted on the silver holder will experience little depolarisation of spin, in which case even σ_n can be taken as zero and we are left with the oscillation term. In the superconducting state of the measured sample, the vortex lattice contributes an additional σ_{sc} term, which varies as temperature is changed below the transition temperature. The overall depolarisation rate is hence obtained by adding the individual contributions in quadrature: $\sigma^2(T) = \sigma_{sc}^2(T) + \sigma_n^2$.

The depolarisation rate due to the presence of a vortex lattice can be related to the variance of the local magnetic field strength, which can be further expressed in terms of the London penetration depth λ [68]:

$$\sigma_{sc}^2(T) = \gamma_\mu^2 \langle \Delta B^2 \rangle, \ \langle \Delta B^2 \rangle = 0.00371 \Phi_0^2 / \lambda^4, \tag{2.34}$$

where $\Phi_0 = h/(2e)$ is the magnetic flux quantum. With these two equations, one obtains a simple relationship

$$\lambda = 327.5 / \sqrt{\sigma_{sc}}, \tag{2.35}$$

where λ is in nm and σ_{sc} is in μs^{-1}.

Since the penetration depth λ, and therefore σ_{sc}, is related to the superfluid electron density n_s, the experimentally determined temperature dependence of $\sigma_{sc}(T)$ can therefore be used to obtain information about the superconducting gap function, for example to check for existence of multigap superconductivity [53].

2.5 Quantum Oscillations

The observation of quantum oscillations provides a set of powerful experimental techniques for mapping out the Fermi surface of metallic materials using a strong magnetic field. Since the first demonstration of quantum oscillations in magnetoresistance and magnetisation of bismuth by Shubnikov and de Haas [69] and de Haas and van Alphen [70] in 1930, the theory behind these measurements has been well developed and has become instrumental in understanding of crucial aspects of the electronic structures and physical properties of many materials [71]. In this section, I provide a brief account of the theory behind these measurement techniques.

In a semi-classical picture, a free electron travelling at speed $\mathbf{v}$ in a homogeneous magnetic field $\mathbf{B}$ experiences the Lorentz force and undergoes a helical motion along the field direction in real space. In momentum space, this motion of the electron forms a circular orbit, which is constrained by the Bohr-Sommerfeld quantisation condition,

$$\oint \mathbf{p} \cdot \mathrm{d}\mathbf{r} = 2\pi\hbar(n+1/2), \tag{2.36}$$

where $\mathbf{r}$ is projection of the electron position vector on the perpendicular plane to the magnetic field, n is an integer, and the canonical momentum of the electron

$$\mathbf{p} = m\mathbf{v} - e\mathbf{A}, \tag{2.37}$$

where $\mathbf{A}$ is the magnetic vector potential. Given the Lorenz force

$$\mathbf{F} = -e\dot{\mathbf{r}} \times \mathbf{B} = m\dot{\mathbf{v}} = \hbar\dot{\mathbf{k}} \tag{2.38}$$
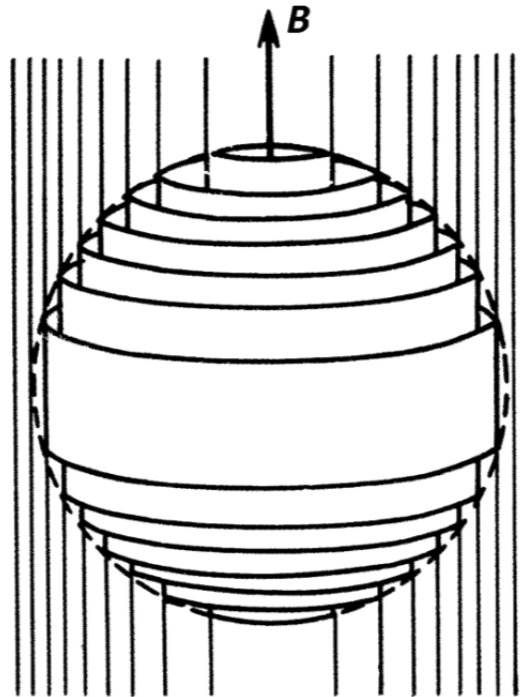

Fig. 2.8 Schematic sketch of Landau tubes indicating electronic k-states within a spherical Fermi surface (dash line) for electrons in an applied magnetic field B. (Figure credit: [71])

and using Stokes' theorem, we can obtain

$$\oint \mathbf{p} \cdot d\mathbf{r} = -e \oint (\mathbf{r} \times \mathbf{B}) \cdot d\mathbf{r} - e \oint \mathbf{A} \cdot d\mathbf{r} \tag{2.39}$$

$$= e \oint \mathbf{B} \cdot (\mathbf{r} \times d\mathbf{r}) - e \int_{area} (\nabla \times \mathbf{A}) \cdot d\mathbf{S} \tag{2.40}$$

$$= eBA_{r_n} = 2\pi\hbar(n + 1/2), \tag{2.41}$$

where A_{r_n} is the orbital area in real space of the cyclotron motion. From 2.38, we expect the orbital area A_{k_n} in momentum space to be related to A_{r_n} by

$$A_{k_n} \equiv \pi k_n^2 = (\frac{eB}{\hbar})^2 A_{r_n} = \frac{2\pi(n + 1/2)eB}{\hbar}, \tag{2.42}$$

where k_n is the orbital radius in momentum space. These orbits form the so-called Landau tubes. For a free electron gas, the Landau tubes are straight coaxial cylinders around the axis of the applied magnetic field. If we assume the independent electron approximation, in a real material, the eigenstates of the system in an applied magnetic field change from the coarse-grained lattice within the Fermi surface to "rings" around the Landau tubes (Fig. 2.8). Each of these rings then holds $\sim BL^2$-fold degenerate states, where L is the sample size. This picture also survives in Fermi liquid theory, namely if the electron-electron interactions are slowly "turned on". This allows the application of our simple picture of ring-like states around Landau tubes to real materials.

As the strength of magnetic field is increased, the radii k_ns of the orbital states in the momentum space grow as $\sqrt{B}$, and their energies E_ns as B. This causes them to cross the Fermi surface one by one. As a Landau level crosses the Fermi energy, it abruptly becomes vacant. Therefore, every time the ring-like states cross the Fermi surface, there will be a peak in the density of states (DOS) at the Fermi energy, leading to an oscillatory behaviour. This behaviour peaks each time the Fermi surface is tangential to a Landau tube. Given that the DOS at the Fermi energy determines the low-temperature thermodynamic and transport properties of the material, we expect all these properties to oscillate with changing magnetic field. This is the basic principle behind all the quantum oscillation measurement techniques.

In this thesis, we are concerned mainly with the field dependence and oscillatory behaviour of magnetisation, which is also known as the de Haas van Alphen (dHvA) effect. The Lifshitz-Kosevich (LK) equation, developed in the 1950s, gives a comprehensive expression for the total magnetisation M of a sample in terms of the applied magnetic field $\mathbf{B}$ and the extremal cross-sectional areas of the Fermi surface. The oscillatory part of the magnetisation

can be expressed as

$$\tilde{M} \propto \sum_{extremal A_F} \frac{FB^{1/2}}{m^* \left| \frac{\partial^2 A_F}{\partial k_z^2} \right|^{1/2}} \sum_{p=1}^{\infty} p^{-3/2} \sin(2\pi p(\frac{F}{B} - \gamma) \pm \frac{\pi}{4}). \qquad (2.43)$$

The detailed derivation of the above equation can be found in Shoenberg's book [71]. Here, $F = F(A_F) = \hbar A_F/2\pi e$ is the de Haas-van Alphen frequency corresponding to an extremal Fermi surface cross-section A_F, and the phase shift in the sine function is positive for minima and negative for maxima in $A_F(k_z)$. m^* is the renormalised quasiparticle mass $\hbar^2/2\pi(\partial A_F/\partial \mu)$ for a particular extremal cross-section (μ is the chemical potential), p is the order of the harmonic (with $p = 1$ for the fundamental frequency) and $\gamma \simeq 1/2$.

In Equation 2.43, we have neglected the effects of finite temperature, finite relaxation time (or impurity scattering) and electron spin. All these factors lead to damping of the oscillation amplitude from the idealised model and must be accounted for. These reduction factors are as follows

- The finite temperature factor:

$$R_T = \frac{2\pi^2 p k_B T m^*/e\hbar B}{\sinh(2\pi^2 p k_B T m^*/e\hbar B)} \qquad (2.44)$$

- The Dingle factor:

$$R_D = \exp(-\pi p m^*/eB\tau) = \exp(-2\pi^2 p k_B T_D m^*/e\hbar B), \qquad (2.45)$$

which is inversely related to the impurity scattering lifetime of the electrons τ in the sample. The Dingle temperature $T_D = \hbar/2\pi k_B \tau$ can be used for estimating the mean free path $l = \sqrt{2e\hbar^3 F}/(2\pi m^* k_B T_D)$.

- The spin-splitting factor:

$$R_s = \cos(\frac{1}{2}p\Delta\phi) = \cos(\frac{1}{2}p\pi g \frac{m^*}{m_e}), \qquad (2.46)$$

is due to the effect of the Zeeman splitting, which induces a phase difference betweeen oscillations from electrons with opposite spins. $g \approx 2$ is the electron g-factor.

As revealed by Equations 2.44 and 2.45, the magnitudes of the oscillations are severely damped unless high-purity samples are used, and a strong and homogeneous magnetic field is applied at low temperatures.

The relation between the dHvA frequencies and the extremal Fermi surface cross-sectional areas provides a tool for the accurate determination of the shape of the Fermi surface. However, the inverse mapping to infer the shape of the Fermi surface sheets from their cross-sectional areas is not necessarily unique – usually, one has to combine the dHvA measurements with band structure calculation predictions to obtain the correct topology of the surface. For more information and the detailed derivations of the equations in this section, I refer readers to [71].

Chapter 3

Experimental methods

3.1 Crystal growth

High quality samples are key to the success of any condensed matter research project. The discovery of new physical phenomena in the realm of low-temperature condensed-matter physics often goes hand-in-hand with the success in improvements or refinements of crystal sample qualities.

In general, large, homogenous and pure crystals are highly desirable, because they enable a broad range of experiments. Single crystals are often more useful than polycrystalline ones, mostly because they allow the investigation of orientation-dependent anisotropic material properties. They also facilitate better refinement of crystal-structural information in diffraction experiments. However, the growth of single crystals with reasonable quality and sizes is not always straightforward, and innovation in growth procedures or techniques may be required. Sometimes, polycrystals are all that can be obtained, and they usually offer a more easily-accessible alternative to study isotropic properties. Polycrystals also provide easier access to off-stoichiometric compositions for compounds which form as solid solutions. In this section, I describe the main crystal growth techniques which have been employed to produce the poly- and single-crystal YFe_2Ge_2 samples described in this thesis.

3.1.1 Induction heating

The main growth technique I have used for synthesising polycrystalline YFe_2Ge_2 is induction heating. The radio frequency (RF) induction furnace (Fig. 3.1) provides a means of contactless heating. By inducing eddy currents, it allows direct heating of metallic materials, such as yttrium and iron, to temperatures beyond their melting and reaction temperatures. Alternating currents with frequency ranging between 50 and 120 kHz are passed through a
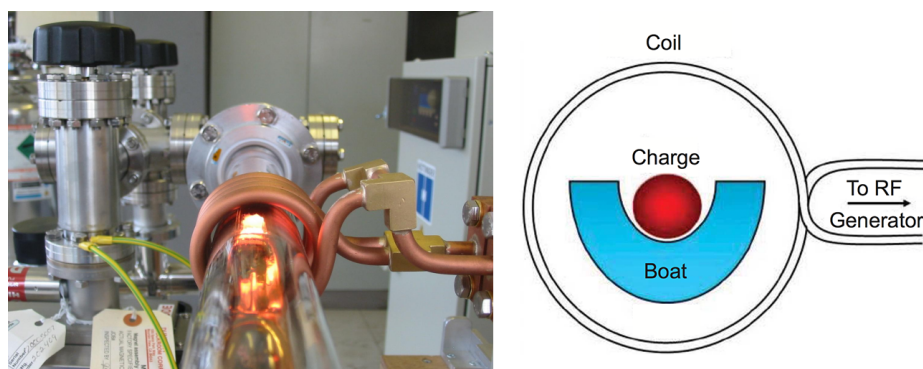
Fig. 3.1 (Left panel) Photo of a radio-frequency induction furnace during sample growth. (Right panel) Schematic sketch of a radio frequency induction furnace showing the essential components. (Figure credit: [72])

copper coil, as shown in the right panel in Fig. 3.1, creating a rapidly changing magnetic field in the coil space. Through electromagnetic induction, eddy currents are induced within the metallic samples, which gradually heat up due to resistive dissipation as the output power on the copper coil increases.

Growth takes place on a water-cooled copper boat, which is composed of several depressions. Materials to be melted can be placed inside such depressions. The copper boat is then enclosed and sealed off from the atmosphere by a large quartz tube during growth. For prevention of contamination and oxidation, we connect the growth space to a vacuum system which consists of a sorption pump for rough pumping (e.g. down to 10^{-3} mbar) and an ion pump for further pumping to ultra-high vacuum (e.g. down to 10^{-8} mbar). The system is also connected to a high-purity pressurised argon (99.999% pure) bottle, allowing growth in an inert atmosphere. For further purification of the argon gas, a titanium ingot is usually placed in one of the depressions on the copper boat, and is heated up in the argon environment before growth for gettering (absorbing) any residual oxygen or nitrogen gas contents.

To perform a growth, high-purity starting materials of carefully weighted amounts are placed on one of the depressions on the copper boat. After pumping the system to high vacuum of around 10^{-7} mbar, the starting materials are baked out by heating them to a few hundred degrees Celsius for outgassing any moisture absorbed on the surface. During the outgassing process, the ion pump continuously pumps on the quartz tube section. Once all moisture is baked out and the pressure inside the chamber drops back down, argon gas with pressure of slightly above 1 bar is introduced into the system. The titanium getter is then heated until it becomes slightly red hot and the power is held for more than 30 minutes to purify the argon gas.

With a clean argon environment, the starting materials can be heated gradually to start a reaction. Iron is usually the easiest to heat up as it couples best to the magnetic field produced by the copper coil. Once the iron pieces are melted, they quickly dissolve and react with the other input materials. Before all the starting materials are molten together, there is usually a sudden exothermal reaction, at which point the shape of the lump of material changes rapidly, and slightly expands. After the sample is completely molten, further increases in power result in a pronounced stirring of the melt, which allows thorough mixing of the materials to produce a more homogeneous mixture. Such effect is called electromagnetic stirring. During the growth, the temperatures of the materials can be monitored using a Marathon Infrared Thermometer MR1S. This provides a quick and convenient measurement of temperatures above $\approx 1000\,^{\circ}\mathrm{C}$, provided that the visual path to the measured object is not badly obstructed.

After complete melting and mixing of the input materials, the melt gets quenched by switching off or quickly lowering the power to the copper coil. Samples grown using the RF induction furnace are typically polycrystalline. Such as-grown crystals usually contain significant amount of crystal defects, caused by the sudden quenching and the prominent thermal gradient inside the samples due to the cold boat system. To reduce the amount of defects, annealing of the grown samples at elevated temperatures is often necessary. Annealing of the sample can be performed directly inside the RF induction furnace. However, when longer period of annealing is required, a box furnace with samples sealed in a quartz ampoule may be a better option. Further description of the annealing process is given in Section 3.1.4.

3.1.2   Flux growth

The technique of growing single crystals using metallic fluxes is probably one that requires the least resources in terms of equipment set-ups. The method of flux growth is analogous to precipitating sea salt from sea water, or, more accurately, making rock candy by cooling down hot sugar-saturated water solution. The "flux" selected is often a metallic element with a relatively low melting point, such as bismuth, tin, indium and antimony, etc, although more complex flux materials are also widely used in special cases.

Flux growth exploits the temperature-dependent solubilities of different elements and the differences in stability of the compound materials in the molten flux. To create a protective atmosphere for the reaction to take place, a setup illustrated in the sketch Fig. 3.2 is commonly used, whereby the starting materials are placed in an alumina crucible which is in turn enclosed inside a quartz ampoule. On top of the first crucible, an alumina disc filter and another empty crucible can be placed up-side-down for catching the molten flux at the
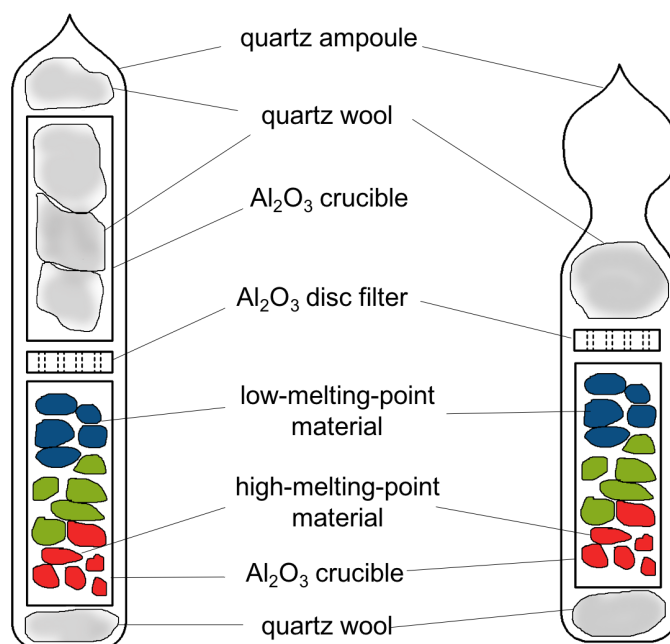
Fig. 3.2 Schematic pictures showing two flux-growth setups which allows centrifugation of molten flux at the end of the growths.

end of a growth. The ampoule is then placed inside a larger crucible holder and put into a box furnace, for which a temperature-versus-time profile will be programmed.

The quartz ampoule is usually filled with argon gas with a partial atmospheric pressure, e.g. around 0.1 bar, to allow for pressure balance with the ambience when heated to high temperatures. This is because quartz tends to soften when heated above 1000 °C and, if a large pressure imbalance exists, the quartz ampoule may explode or implode. Quartz shards or quartz wool placed below the crucible, as shown in Fig. 3.2, are necessary for avoiding firm contacts of the crucible to the inner wall of the quartz ampoule. This prevents a build-up of stress on the ampoule due to differential thermal expansions with the alumina crucible, stopping cracking at high temperatures.

Inside the bottom crucible, starting materials with higher melting points are generally packed underneath ones with lower melting points to ensure the complete submersion of all starting materials when the flux is molten. Once the desired crystals have precipitated and grown from the flux, they have to be separated from the flux. A centrifuge is often used for removing the excess flux. At the end of the growth, the ampoule is kept at an elevated temperature above the melting point of the flux. By quickly taking the hot ampoule out of the box furnace and loading it up-side-down into the centrifuge holder, we can use the large

centrifugal force from the spinning to detach the flux from the alumina crucible, leaving only the crystals behind. An alumina filter disc is very useful at catching the crystals, while allowing the flux to flow through. Alternatively, chemical etchants which react with the flux but do not attack the product crystals can also be used for removing the flux. Often the two methods are used together, where the latter is used for removing a small residual of flux on the crystal surfaces.

For further information about the flux growth technique and the comparisons between different fluxes, I refer to [73–75].
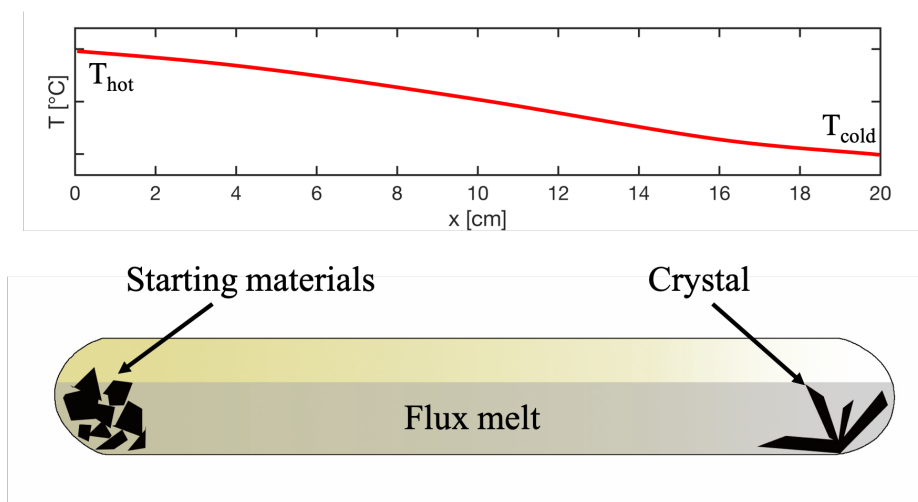
Fig. 3.3 (Upper panel) Temperature profile along the horizontal axis in a liquid transport growth. (Lower panel) Schematic picture of a liquid transport growth.

3.1.3   Liquid transport growth

Conventional flux growths adopt an upright configuration with a uniform temperature profile inside the quartz ampoule which gradually changes as a function of time. While requiring minimal set-up, this method may present two major drawbacks:

- In a conventional flux growth, the yield tends to be limited to only a few hundred milligrams of crystals per growth. This is due to the combination of the constrained crucible sizes, the need for high concentrations of flux for ensuring complete dissolution and the need for relatively high centrifugation temperatures.

- Precipitation and growth of crystals tends to occur at continuously varying temperatures. This can be detrimental for certain material families, as the thermodynamically stable

composition which precipitates may be different at different temperatures. This can cause the growth of undesirable secondary phases and/or inhomogeneous crystals. Inhomogeneity can appear both within each crystal and also across different crystals in a single batch.

The modified flux technique used for improving YFe_2Ge_2 single-crystal qualities, which is discussed later in Section 5.1, has similar problems. In those growths, the growth temperatures have to be kept below the point of complete dissolution of the charge materials, which led to an even lower yield.

One way to tackle the above weaknesses of a conventional flux method is to instead perform a flux growth in a horizontal configuration with a temperature gradient along the horizontal axis. This method has been tested for growth of a wide range of materials in both self-flux and halide flux growths [76]. The flux growth in the horizontal configuration can be effectively thought of as a liquid analogue to the vapour transport technique, in which the flux becomes the transport agent. In these liquid transport growths, the charge-to-flux ratio is no longer constrained by the solubility of the charge materials in the flux at any given temperature. This allows a much larger yield in each growth. Furthermore, both the growth temperature and the composition of the charge at the growth site can be kept constant, allowing the most homogeneous conditions.

Fig. 3.3 shows the temperature profile and schematic diagram of a liquid transport growth. The charge materials together with the flux are placed at one end of a sealed quartz ampoule.

Fig. 3.4 Pictures showing an ampoule enclosing crystal-containing Sn flux before (upper panel) and after (lower panel) centrifugation.

When temperature is increased, the flux then spreads evenly across the ampoule. The length of the ampoule is around 20 cm, allowing its ends to be positioned at the zone centres of a two-zone furnace. In order to ensure the diffusion of the charge across the length, a large amount of flux is needed to partially fill the ampoule. The charge dissolves at the hot end and is then transferred to the cold end driven by a composition gradient. When the composition of the charge reaches the solubility limit at the cold end, precipitation of the thermodynamically stable phase occurs. During a growth the temperature profile along the quartz ampoule is kept constant. Therefore, until the charge at the hot end dissolves completely, the growth at the cold end takes place at a nearly constant temperature and composition. As discussed later in Section 5.1, this has a significantly positive effect on improving the sample quality of YFe_2Ge_2 crystals.

Since the growth takes place in a long quartz ampoule, extracting the crystals from the flux has to be done in a separate step. After breaking off the quartz ampoule, the cold end of the flux, where the crystals are embedded, is sawed off and resealed under vacuum in another quartz ampoule (see Fig. 3.4). The ampoule is heated to above the melting point of the flux and the majority of the flux is separated from the crystals in a centrifuge. The thin neck and the quartz wool (Fig. 3.4) helps trap the crystals in place while allowing the hot flux to flow towards the upper compartment during the centrifuge. The excess flux coating the surface of the extracted crystals is further removed by soaking the crystals in diluted hydrochloric acid.

3.1.4   Annealing

As mentioned in Section 3.1.1, the as-grown samples produced in the induction furnace may contain significant levels of disorder. Broadly speaking, lattice disorder can be understood as the absence of perfect long-range order of atoms from their equilibrium crystal lattice sites. When the effect of disorder is pronounced, it can significantly change the measured properties of the crystalline samples. For samples produced in the induction furnace, such disorder can easily result from the rapid cooling when the melt gets in direct contact with the cold copper boat during quenching. Crystal defects, such as interstitial point defects, vacancies and anti-site disorder, can form during solidification when rapidly cooling from high temperatures. Annealing, namely a heat treatment of a sample at elevated temperatures below its melting point, can be an effective method for partially removing lattice disorder.

The optimum annealing conditions are difficult to predict and are usually dependent on problems of concern. So far, we have been relying on empirical experience for finding the best annealing procedures. The RF induction furnace allows for annealing at a relatively high temperature for metallic samples (up to their melting point), but it is relatively unsafe for keeping it running for a long time while unattended. An alternate way of annealing is to

use a box furnace. With the samples sealed inside a quartz ampoule, which is either pumped to low vacuum or filled with partial argon atmosphere, it can be safely left in a box furnace and heated for a prolonged period of time to temperatures as high as $1000\,^\circ$C. The problem of increasing the temperature further (the highest temperature for our box furnace is around $1300\,^\circ$C) is that the quartz ampoule becomes soft as its melting temperature is approached and may break as a result. Another advantage of using the box furnace is that multiple samples can be annealed at the same time if they are sealed in several quartz ampoules and/or separated by placing them within different alumina crucibles.

3.2 Physical property characterisations

3.2.1 Cryostats

Quantum Design Physical Property Measurement System

The commercially available Quantum Design (QD) Physical Property Measurement System (PPMS) is an easy-to-operate and versatile platform on which resistivity, heat capacity and other measurements can be carried out down to low temperature and in high magnetic fields. The PPMS used in this work operates through the use of liquid ^{4}He. By evaporative cooling through pumping on the vapour above the ^{4}He bath and using a heater, this ^{4}He cryostat allows reliable temperature control to within ± 0.005 K at sweep rates from $0.01\,\mathrm{K\,min^{-1}}$ to $20\,\mathrm{K\,min^{-1}}$ between 1.9 K and 400 K. With an installed superconducting magnet, magnetic fields between -9 T and 9 T can be applied to the samples.

One of the defining features of the PPMS is its use of a standardised "puck" for each measurement option. Fig. 3.5 shows the schematic of the PPMS cryostat insert design. Electrical access to the measurement hardware is conducted through a 12-pin connector at the base of the PPMS sample chamber. Different measurement options are accessed by using specific measurement pucks, on which the samples are mounted.

To enable a lower base temperature than the standard 1.9 K limit, an additional helium-3 refrigerator option can be added. This includes a closed-cycle ^{3}He probe which extends the minimum experimental temperature to below 0.4 K, thanks to the lower boiling point of ^{3}He. The 12-pin connector again plugs into the base of the ^{3}He probe. Along the probe, thermal anchoring contact fingers help keep the probe cool and maintain its temperature at 1.9 K. Through the length of the probe, there are two gas-handling lines: one pump line and one return line. Near the base of the probe is a reservoir, into which ^{3}He gas, which flows down the return line, condenses. The reservoir and the thermally linked sample stage are cooled when a turbo pump pumps on the liquid ^{3}He. The sample stage consists of a thermometer,

HEAD

RODS

BAFFLES

MAGNET

HELIUM
LEVEL METER

SAMPLE SPACE
COOLING ANNULUS
SUPER INSULATION
VACUUM

SAMPLE CHAMBER

INNER
VACUUM
TUBE

HEAT
SHIELD

OUTER
VACUUM
TUBE

MAGNET

CENTER OF
MAGNETIC FIELD

BOTTOM OF SAMPLE CHAMBER
WITH SAMPLE PUCK CONTACTS

THERMOMETERS
AND HEATERS

IMPEDANCE
HEATER AND
THERMOMETER

PROTECTIVE CAP
(OPEN TO HELIUM)

IMPEDANCE
TUBE

BELLOWS

Cross Section

Fig. 3.5 Schematic diagrams showing (on the left) the Quantum Design PPMS insert which includes a vacuum sample space and a superconducting magnet, and (on the right) the detailed components of the probe. (Figure credit: [77])

a heater and the interface of the sample-mounting platform. Only eight connections are available for sample measurements in the ^{3}He probe, since the thermometer and heater take up the other four. Similarly, various standardised pucks can be swapped and attached to the sample stage for different types of measurements.

Cryogenic SQUID

DC magnetisation measurements described in this thesis have been performed using a Cryogenics S700X magnetotometer. Fig. 3.6 shows a schematic diagram of its cross-section. Measurements are taken inside the variable temperature insert (VTI) which is connected to a ^{4}He reservoir via a needle valve. The combination of helium flow and a heater control allows measurements across a temperature range from 300 to 1.8 K. This can be further extended down to < 350 mK using a ^{3}He insert. The system is equipped with a superconducting magnet, which can apply magnetic fields up to ± 7 T. Two operating modes for the applied

field are available, namely the "low-field" and "high-field" modes which operate with the more and less sensitive power supplies respectively. In the low-field mode, it is possible to operate at a resolution of $\sim 0.05\,\text{mT}$.

The ^{3}He insert (Fig. 3.7) allows the extension of our measurements down to $< 350\,\text{mK}$. It consists of an enclosed ^{3}He space, which couples to the sample through a silver sample holder. The sample space is further enclosed in an evacuated copper can and is therefore only coupled to the VTI via a weak thermal link. Fig. 3.7 shows schematically the operating procedure for reaching the base temperature. This comprises the following steps:

- The ^{3}He probe is inserted into the VTI space after the sample is mounted and the vacuum can evacuated. As the insert is cooled, ^{3}He gas is drawn and absorbed onto the internal surfaces of the charcoal sorb.

- As the temperature of the charcoal sorb is cooled to $1.8\,\text{K}$, it absorbs most of the ^{3}He gas.
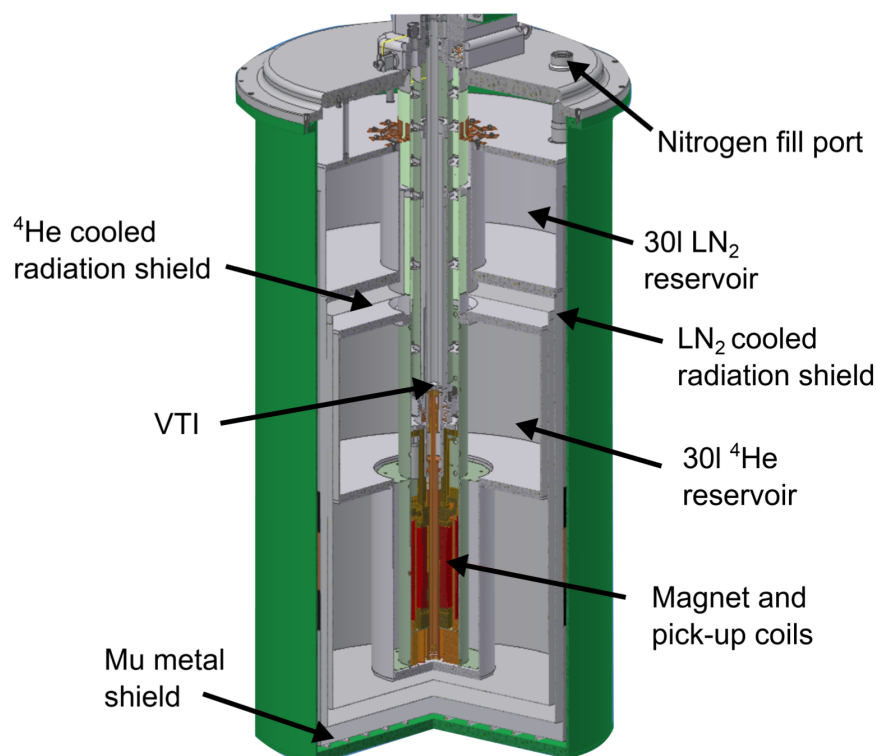
Fig. 3.6 Schematic view of the cross-section of the S700X magnetometer. (Figure credit: [78])
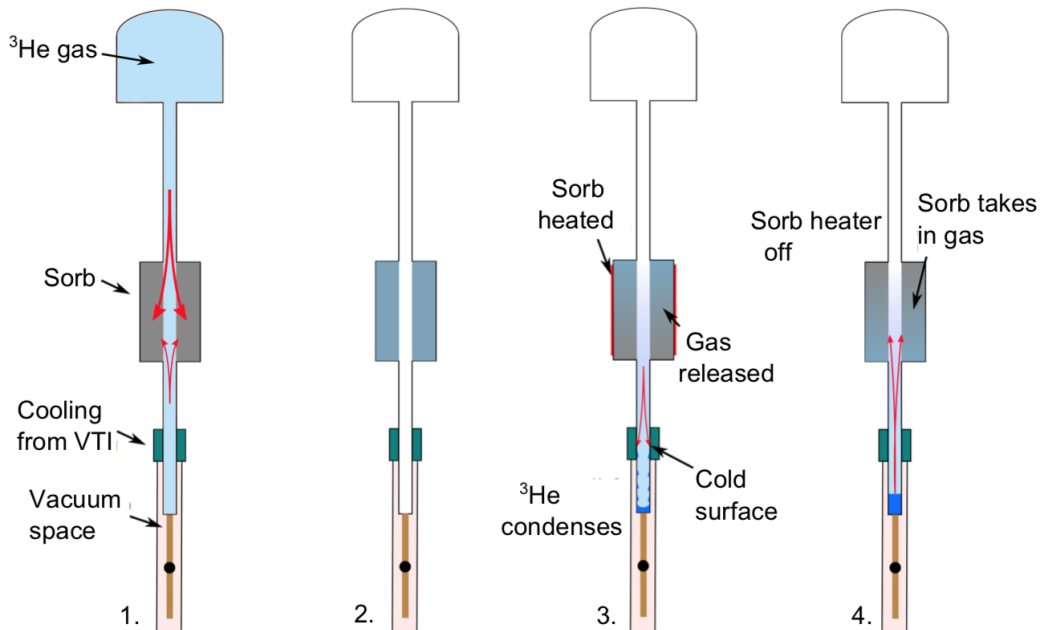
Fig. 3.7 Schematic diagram showing the operation cycle of the ^{3}He probe to the Cryogenic S700X magnetometer. (Figure credit: [78, 79])

- By heating the charcoal up to 50 K, the ^{3}He is released. As the sample holder and the gas is cooled to the VTI temperature, the gas starts to condense onto the cold surfaces. A puddle of liquid ^{3}He aggregates at the bottom of the enclosed space.

- Finally the heater is ramped back down, such that the charcoal re-absorbs the ^{3}He gas. This causes the pressure to drop, hence reducing the boiling point of ^{3}He and further reducing the temperature of the sample holder until the base temperature.

3.2.2   Resistivity measurement

Electrical resistivity is one of the most commonly studied material properties. The temperature dependence of the resistivity allows the detection of various phase transitions, a typical example being the superconducting transition, in which a sudden drop of the resistivity value to zero can be observed.

A common way for measuring resistivity ρ is by a four-point method, where the resistance R of a rod-shaped sample with known geometry (e.g. length l and cross-section A) is measured by passing a known current I through the current-contacts and measuring the voltage V across the voltage-contacts. The four wire contacts are placed along the length of

the sample so that the current contacts are nearer to the two ends and the voltage contacts are in between but also near the ends of the sample. The resistivity is therefore deduced from the resistance by:

$$\rho = R\frac{A}{l} = \frac{V}{I}\frac{A}{l}.$$ (3.1)

Compared to a two-point measurement, the four-point method has the advantage that it prevents the pickup of contact resistance. Additionally, to circumvent the effect of thermoelectric voltages, low-frequency (e.g. 23 Hz) AC-currents, rather than DC-currents are used.

On the ^{3}He probe of the PPMS, two samples can be mounted on a detachable 8-pin puck which is then plugged onto the sample stage on the probe. AC-currents between 0.1 and 3 mA are passed through the samples and the in-phase voltages are measured via an inbuilt lock-in amplifier. Thin gold wires (e.g. 25 μm in diameter) are typically used for electrical connections between the samples and the measurement puck. To attach the gold wires to the samples and to ensure low-resistance point contacts, precision spot-welding is used. During spot-welding, the gold wire is trapped between the sample and a sharp tungsten tip. By discharging a sharp current through the tungsten tip and the sample, the wire is heated up and bonded to the sample. This method allows contact resistance of less than 0.1 Ω at room temperature.

3.2.3   Heat capacity measurement

Heat capacity is a bulk property of a material which, at low temperatures, is closely related to the electronic properties of a metallic sample and provides a measure of the quasi-particle mass for a Fermi-liquid material.
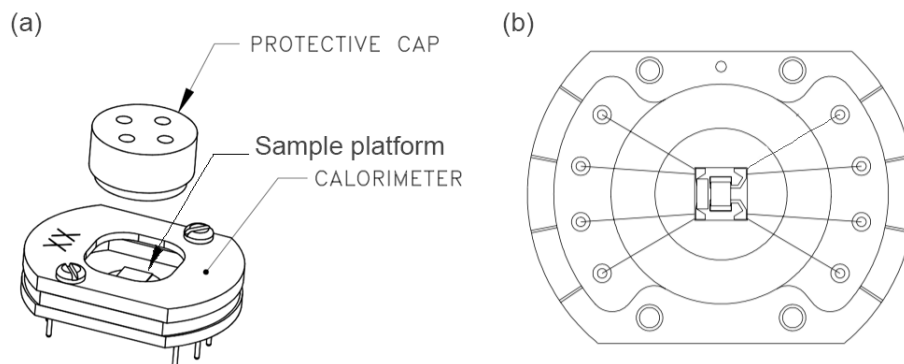

Fig. 3.8 (a) PPMS ^{3}He heat capacity puck. (b) Schematic showing the bottom view of the sample platform with wires connecting to the puck pins. (Figure credit: [77])

Measurements of the heat capacity can be carried out in the PPMS ^{3}He probe down to around 370 mK. Fig. 3.8 shows the PPMS ^{3}He heat capacity puck. Usually, a sample with mass ranging from 0.4 to 12 mg is mounted onto the sample platform using Apiezon N grease. Four wires suspend the sample platform, which serve as the electrical leads for the attached heater and thermometer. The four wires also provide a well-defined thermal connection between the platform and the puck, which allows a quasi-adiabatic environment of the platform. During a measurement, the PPMS high-vacuum system maintains the pressure in the sample chamber to below 0.01 µbar.

A pulse-relaxation method is used for measuring sample heat capacity. Taking each data point involves several steps. The sample platform temperature is first stabilised towards the set puck temperature. With a current passed through the sample platform heater for a predetermined time period, the platform temperature rises and then relaxes back when the current is terminated. By monitoring the sample platform temperature and the heater power throughout the process, heat capacity of the sample can be calculated.

Two fully automated algorithms are performed by the PPMS software for analysis of the raw data. The general analysis, called the two-tau model [80], assumes a non-ideal thermal contact between the sample and the platform. By optimising a least-square fitting of measured data to the two-tau model, the values of heat capacity and other parameters, such as the thermal conductance of the wires, can be determined. This model can be expressed as follows:

$$C_p \frac{dT_p}{dt} = P(t) - K_w(T_p(t) - T_b) + K_g(T_s(t) - T_p(t)) \tag{3.2}$$

$$C_s \frac{dT_s}{dt} = -K_g(T_s(t) - T_p(t)) \tag{3.3}$$

where C_p is the heat capacity of the sample platform, C_s is the heat capacity of the sample, and K_g is the thermal conductance between the two due to the presence of the grease, whereas K_w is the thermal conductance of the supporting wires. The respective temperatures of the platform and sample are given by $T_p(t)$ and $T_s(t)$. T_b denotes the temperature of the thermal bath (puck frame). $P(t)$ is the power applied to the heater.

The second analysis (one-tau method) involves a simpler model which assumes perfect thermal coupling between the sample and the sample platform and can be expressed by the equation:

$$C_{tot} \frac{dT}{dt} = -K_w(T - T_b) + P(t), \tag{3.4}$$

where C_{tot} is the total heat capacity of the sample and the platform. Before each run, heat capacity of addenda (i.e. the sample platform with the added grease) is measured. This is then treated as the background and is later subtracted from the data for accurate measurement of the sample heat capacity. The one-tau method is primarily used for determining the addenda heat capacity.

3.2.4   Magnetisation measurement

The Meissner effect, namely the expulsion of magnetic flux in the superconducting state, is one of the key characteristics exhibited by a superconductor. The measurement of a sample's magnetisation as it transitions from the superconducting to normal state can provide both strong evidence for bulk superconductivity and an estimate for the superconducting volume fraction.
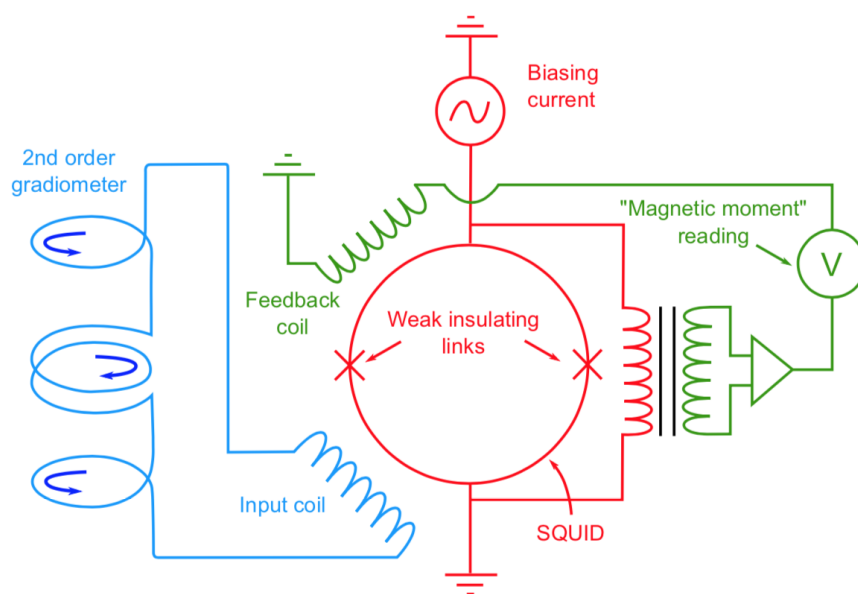
Fig. 3.9 Schematic diagram showing the coil sets of the detection circuit and the SQUID in the Cryogenic S700X magnetometer. (Figure credit: [78, 79])

The Cryogenic S700X magnetometer has been used for precision measurement of sample magnetisation. A key component of this magnetometer is a set of coils arranged in a second-order gradiometer configuration shown on the left-side of Fig. 3.9, whereby a two-turn coil is sandwiched between two counter-wound single coils. The pick-up coils form a closed loop with the input coil, which couples the flux in the pickup coil to the superconducting quantum

interference device (SQUID). A bias current larger than the critical current is applied to the SQUID, which allows a voltage to develop across the device. This voltage is dependent both on the current and the magnetic flux. It is a periodic function of the flux through the SQUID ring. During operation, the SQUID is put in "locked mode", in which the feedback system provides a flux which is applied in the opposite direction, keeping the output from the SQUID constant. The voltage across a resistor in the feedback loop is then read out [78]. As a sample is pulled through the set of counter-wound coils, magnetic flux through the coils changes as a result of the sample's magnetization, which in turn triggers the SQUID and the feedback circuits. The measurement of voltage $V(z)$ across the feedback loop resistor as a function of sample position z can then be compared to that expected for an ideal dipole, providing an absolute value of the sample's dipole moment. Three different resistors are present in the feedback loop, corresponding to the three standard sensitivity range settings. The typical sensitivity of such a magnetometer is $10^{-12}\,\text{Am}^2$.

The output voltage for an ideal dipolar point-like sample $V^I(z)$ can be modelled exactly [78]. A common approach for determining the sample magnetic moment is to perform a least-square fit to the voltage output of the SQUID $V^R(z)$ to match the closest resembling $V^I(z)$. However, the S700X magnetometer use an alternative approach, in which the voltage $V^R(z)$ is not only fitted to $V^I(z)$, but also to a weighted summation of its derivatives as follows:

$$V(z) = \sum_{i=0}^{n} c_i \frac{\mathrm{d}^I V^I(z)}{\mathrm{d} z^i}, \tag{3.5}$$

where the coefficients c_i are determined via singular value decomposition (SVD). Such a "multi-pole" fitting has the advantage over the traditional fitting method in that it is less sensitive to influence of the sample geometry [78].

3.3   Muon spin rotation spectroscopy

Muon spin rotation is particularly useful for studying the mixed state of a type-II supercon-ductors. As a microscopic probe, μSR is advantageous compared with macroscopic methods, such as SQUID magnetisation measurements, in that it provides additional structural in-formation. However, it should still be regarded as a bulk measurement, as the muons can typically penetrate around 100 to 200 μm into the sample. Transverse-field (TF)-μSR can be used for measuring the internal magnetic field distribution and determine the temperature dependence of the London penetration depth λ in the vortex state of a type-II superconductor as described in Section 2.4.
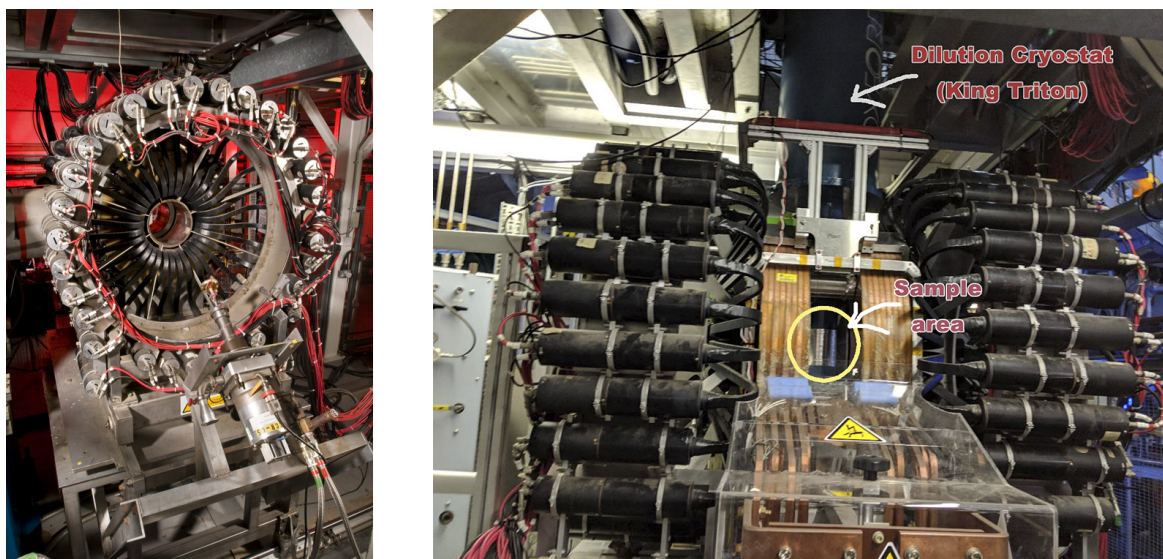
Fig. 3.10 (Left panel) Photo showing one half of the MuSR instrument at the ISIS Neutron and Muon Source. (Right panel) Side-view of the same instrument showing the sample space in the centre of two Helmholtz coils and the cryostat which is craned in from above. The black cylinders are the detectors.
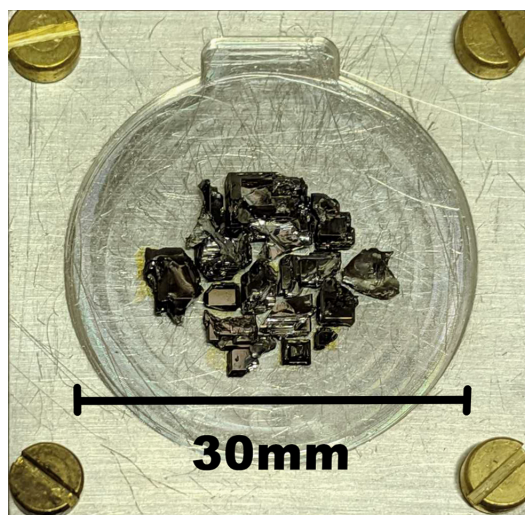

Fig. 3.11 Samples of YFe_2Ge_2 mounted on a silver sample holder using GE varnish, prepared for a μSR experiment.

The TF-μSR experiment on YFe_2Ge_2 took place at the ISIS Neutron and Muon Source, Rutherford Appleton Laboratory. The MuSR instrument at ISIS, RAL is a 64-detector spectrometer. Each detector consists of a piece of plastic scintillator joined by an acrylic light-guide to a photomultiplier tube. The detectors are arranged into two circular arrays (see Fig.3.10) which are centred around a hollow sample space where the muon beam is focused. MuSR is fitted with an active zero-field system made up of three pairs of compensation coils aligned in the x-, y- and z-direction correspondingly. This allows the cancellation of any stray fields from the Earth magnetic field and other nearby instruments. It is possible to achieve a zero-field stable to within $1\,\mu T$. There is also a primary magnet on MuSR, which is a water-cooled, conventional electromagnet, cable of producing a magnetic field of $0.25\,T$. The MuSR spectrometer can be rotated through 90°, which changes whether the primary magnetic field is applied parallel or perpendicular to the initial spin polarisation direction, allowing either a longitudinal-field or a transverse-field μSR experiment.

Samples are mounted on a high-purity silver sample holder using small amount of GE varnish, as shown in Fig. 3.11. The silver holder adds a non-depolarising background signal to the measured asymmetry, which can be easily accounted for in the data processing procedure as discussed later in Section 5.3. The sample holder can then be mounted onto various cryostats and inserted into the hollow sample space. In our case, a dilution refrigerator was used, which allowed a base temperature of around $50\,mK$.

3.4 Powder X-ray diffraction

Solid crystalline materials are formed from an ordered arrangement of atoms which can be described by their crystal structures. Powder X-ray diffraction is a common experimental technique employed for determining the structural characteristics of crystalline solids. It is also a useful tool for identifying impurity phases in crystalline samples.

The basis for all X-ray diffraction techniques is the scattering of X-ray beams from uniformly spaced planes of atoms as illustrated in Fig. 3.12. When the interplanar spacing, d, between the atomic layers satisfies the Bragg condition $n\lambda = 2d\sin\theta$, where λ is the wavelength of the incident X-ray, constructive interference occurs leading to a high intensity of the outgoing beams at the diffraction angle θ. Here θ is the angle between the incident beam and the crystallographic plane. The Miller indices, h, k and l, can be used to describe the families of parallel planes within the lattice. The values of the three indices correspond to the reciprocal of the planes which intercept on the a, b and c axis respectively.

In a powder X-ray diffraction (PXRD) measurement, a sample is powderized into small crystallites typically of a few microns in size and spread across a glass coverslip. A thin
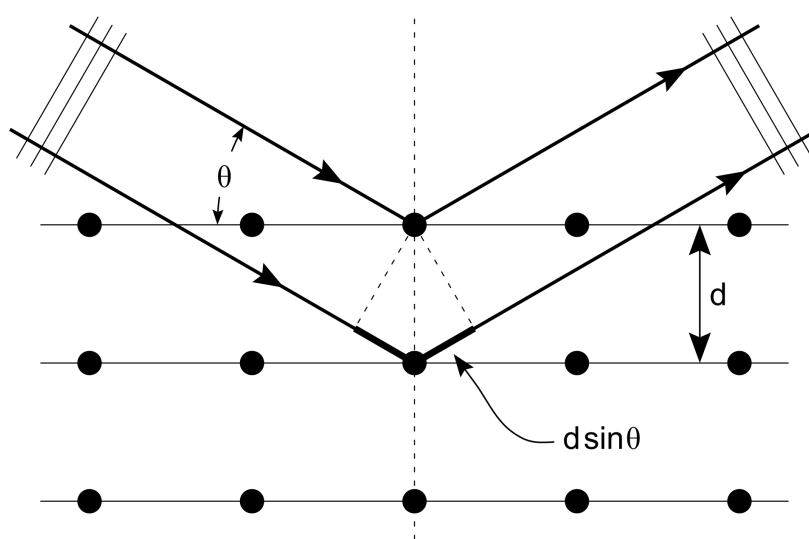
Fig. 3.12 Figure showing elementary derivation of Bragg's Law, with incident radiation beams reflecting off the lattice points whose path length difference equals to $2d\sin\theta$. Constructive interference occurs when the path difference is equal to an integer number of the wavelength. (Figure credit: [81])

layer of vacuum grease can be used to hold the crystallites in place to prevent preferential alignment of the flat facets with the coverslip. When illuminated with an X-ray beam, the random orientations of these small crystallites allow the Bragg condition to be met by a proportion of the different spacing d's present in the lattice structure. Bragg condition further ensures that for a beam of constant λ, diffraction spots are only observed for certain discrete angles related to the lattice structure and lattice parameters. In a typical PXRD instrument, the detector is moved through different values of the scattering angle 2θ along a constant azimuthal angle ϕ. And the intensity of the scattering radiation is collected at each position for a set duration. By comparing to the expected theoretical XRD spectra, structural information can be extracted for a particular sample.

PXRD studies described in this thesis have been carried out using a Bruker D8 X-ray diffractometer (Cu Kα radiation, Bragg-Brentano geometry, 40mA and 40kV beam). In the Bragg-Brentano geometry, the diffraction vector, which bisects the angle between the incident and scattered beam, is always normal to the surface of the sample holder. This is achieved by keeping the sample fixed in the horizontal position while rotating the X-ray source and detector by θ and $-\theta$ respectively. A Cu Kα source ($\lambda_{K\alpha_1} = 1.540\,56\,\text{Å}$, $\lambda_{K\alpha_2} = 1.544\,39\,\text{Å}$) is used due to the closeness of the atomic spacings d_{hkl} to the wavelengths.

A PXRD pattern carries two sets of crucial information. Firstly, the positions of the peaks at $2\theta_{hkl}$ provide information regarding the lattice parameters and space group symmetry. Secondly, the intensity and the shape of the peaks encode knowledge of the different atoms, including their positions, the lattice site occupancies and the thermal vibration parameters. Once the powder diffraction pattern was obtained, Rietveld analysis [82], which is a least square fitting method, was used to extract information of the crystal structure. Such fitting method is well incorporated into analysis softwares such as FullProf [83], which has been used for the analysis shown in this thesis. Starting with a pre-existing trial structure (either from prior knowledge or from an educated guess of the crystal structure), the program calculates a powder diffraction profile and compares it to the experimentally obtained data, which then allows it to iteratively refine for the selected parameters, such as lattice constants, atomic positions, site occupancies, etc. The good-ness of the fit to the modelled trial structure is then measured numerically using a R values [84]. The presence of additional unintended peaks in the PXRD pattern is often an indication of secondary phases. Further refinement can be performed simultaneously for multiple phases once the peaks for the major phase have been identified.

When the modelled intensities in the diffraction pattern deviate significantly from the actual data or only a partial structural model is available, it is possible to carry out a "structure-free" LeBail refinement [85]. In this analysis, the intensities of the individual peaks are not treated as least-square parameters and are not refined. This allows us to obtain the profile parameters, such as unit cell parameters, peak shapes, etc, which can serve as initial values for a complete structural Rietveld refinement. This analysis is also very useful when the accurate determination of lattice parameters is the main objective of the experiment.

In order to carry out a Rietveld or a LeBail refinement, the background contribution to the diffraction pattern is estimated and subtrated using linear interpolation between background data points. The peak shapes observed depend on both the instrument parameters (such as apparatus geometry, type of radiation source, etc) and the sample (due to size or strain effects). For the analysis in this thesis, a pseudo-Voigt function, which is the convolution of a Gaussian and a Lorentzian function, was used to model the peak shape. The full-width at half maximum (FWHM) for the Gaussian component was modelled by a Caglioti function:

$$\text{FWHM} = U\tan^2\theta + V\tan\theta + W \tag{3.6}$$

and that for the Lorentzian component was modelled by:

$$\text{FWHM} = X\tan\theta + \frac{Y}{\cos\theta} \tag{3.7}$$

The initial values of U, V, W, X and Y were obtained from an instrument resolution function (IRF) file, generated by collecting the diffraction pattern for a well-characterised highly crystalline sample on the instrument (e.g. Al_2O_3).

Chapter 4

Bulk superconductivity in YFe_2Ge_2 polycrystals

The study of superconductivity in YFe_2Ge_2 has proceeded similarly to early work on the exemplary unconventional superconductors $CeCu_2Si_2$ and Sr_2RuO_4 [86, 87]: improved sample quality achieved via modification of growth methods has over time enabled more probing experiments, which in turn have led to a more thorough understanding of superconductivity in these materials. The highly detrimental effect of disorder on superconductivity in YFe_2Ge_2 complicated the growth of adequate crystals for the study of its superconducting properties, and, in the early days, caused controversies regarding the intrinsic nature of superconductivity in this compound [24, 25].

In this chapter, I present the results obtained during a systematic attempt to optimise the growth parameters for synthesising high-quality, polycrystalline YFe_2Ge_2 samples. Thermodynamic, magnetic and transport measurements provide the first conclusive evidence for bulk superconductivity in this compound. Potential causes of disorder, which are detrimental to its superconductivity, are further discussed in light of results from both powder X-ray diffraction (XRD) and energy dispersive spectroscopy (EDS) measurements.

4.1 Crystal growth and characterisation of $Y_{1+x}(Fe_{1+y}Ge_{1+z})_2$ polycrystals

Background

Resistive and magnetic evidence for superconductivity in YFe_2Ge_2 was first reported by the Cambridge Quantum Matter group in 2014 [22]. However, the lack of thermodynamic evi-

dence brought about controversies and raised the possibility of filamentary superconductivity caused by alien phases [24, 25]. Measurements in [22] were collected in polycrystalline samples with a maximum residual resistivity ratio (RRR = $\rho_{300\,K}/\rho_{2\,K}$) of around 50. It was noted that samples with lower RRRs did not show superconductivity. This suggests that disorder may play a role in limiting superconductivity in this compound.

Isostructural to YFe$_2$Ge$_2$, the famous heavy-fermion superconductor CeCu$_2$Si$_2$ is known to exhibit magnetic and superconducting properties which are extremely sensitive to small changes in sample composition. Minor increases in the Cu concentration can change it from the A type (antiferromagnetic with no superconducting transition) to the A/S type (AFM competes with SC without microscopic coexistence), or to the S type (superconducting with no AFM transition) [88]. Anticipating the existence of a narrow homogeneity range of the '122' phase in the ternary Y-Fe-Ge phase diagram, similar to that observed for Ce-Cu-Si, we decided to experiment with systematically changing the nominal composition in the polycrystalline samples of YFe$_2$Ge$_2$.

Crystal growth

Polycrystalline Y$_{1+x}$(Fe$_{1+y}$Ge$_{1+z}$)$_2$ ingots (with $-0.1 < x, y, z < 0.1$) were grown in a radio-frequency induction furnace on a water-cooled copper boat under a high-purity Ti-gettered Ar atmosphere. To limit the precipitation of stable Y-Ge alloys, Y (3N, Alfa Aesar) and Fe (4N, vacuum remelted, Alfa Aesar) were melted first and thoroughly mixed to form ingots of YFe$_2$. Ge (6N, Alfa Aesar), and Y or Fe were then added and melted together with YFe$_2$ to obtain the desired nominal composition. The mass losses due to evaporation were less than 0.3%, and homogeneity was ensured by electromagnetic stirring and repeated flipping and remelting of the ingots. The ingots were quenched to the cooling water temperature within seconds and then heated up again to near 1250 °C for a first annealing step in the induction furnace, which was again followed by rapid quenching. Each of the resulting ingots was mechanically broken up into two halves, one of which was subsequently annealed at 800 °C in an evacuated quartz ampoule for 7 days ("annealed"), whereas the other half was investigated without prior annealing ("as-grown"). More than 20 ingots with varying nominal compositions have been prepared for this study.

Characterisation

Heat capacity and electrical resistivity were measured with the helium-3 option of the Quantum Design Physical Properties Measurement System (PPMS) from 300 K to 0.4 K using the pulse-relaxation technique and a standard four-wire ac technique, respectively.
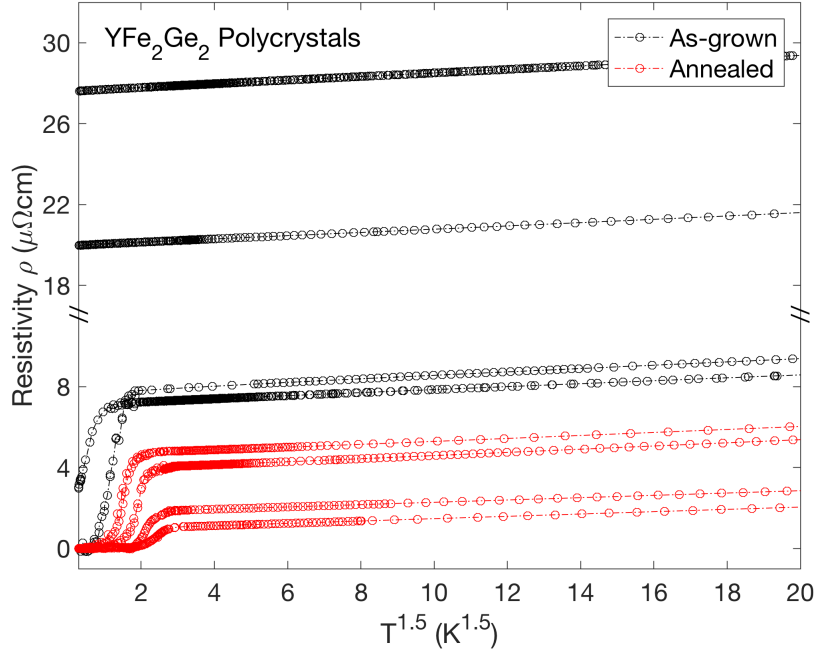
Fig. 4.1 Electrical resistivities versus temperature of a representative set of YFe_2Ge_2 as-grown and annealed polycrystalline samples, showing a wide variation in super-conducting transition temperature T_c and residual resistivity ρ_0 and a $T^{1.5}$ normal-state temperature dependence.

The resistivity data were scaled at 300 K to the published value of $190 \mu\Omega$ cm [34]. All the annealed samples and a selection of as-grown samples were measured to check for evidence of bulk superconductivity.

A representative set of resistivity data of both as-grown and annealed samples with different nominal compositions is shown in Fig. 4.1. At temperatures below 10 K, the normal-state resistivity of all samples displays an anomalous power-law temperature dependence of $\rho(T) = \rho_0 + AT^{3/2}$, suggesting Fermi liquid breakdown. This is similar to those seen in other transition metal compounds such as $MnSi$, $ZrZn_2$, and $NbFe_2$ near the threshold of magnetic order [89–92]. It might be attributed to the proximity of YFe_2Ge_2 to an antiferromagnetic quantum critical point [22, 28]. To quantify the variations in sample quality, we use the residual resistivity ratio (RRR) and the resistive transition temperature T_c (50% point of the transition) as measures. As seen in Fig. 4.1, significant variations in both RRRs and T_cs exist between different samples which differ by their nominal compositions and histories of heat
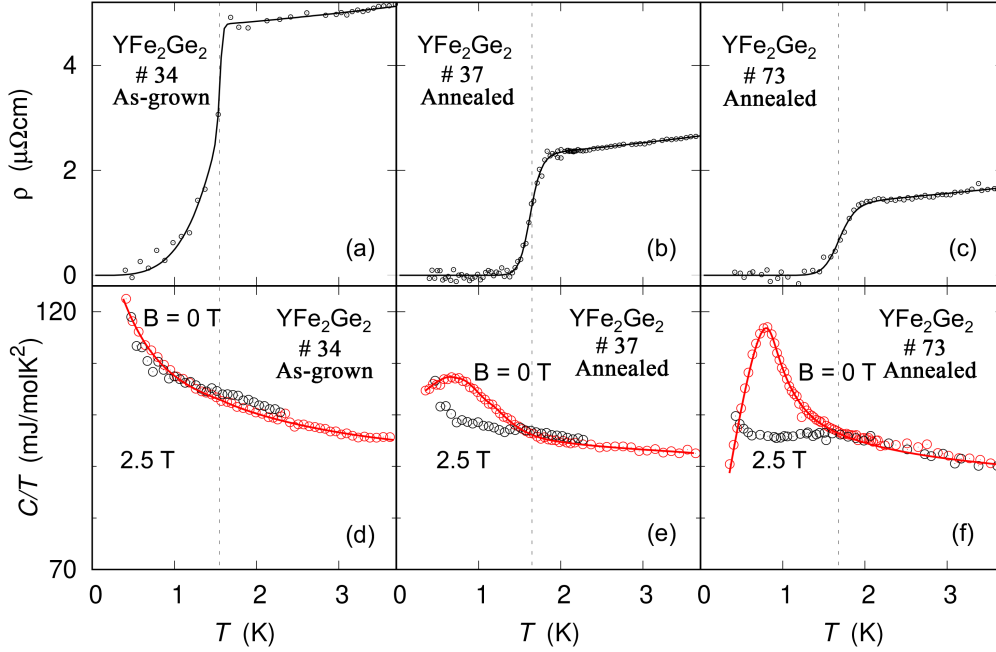
Fig. 4.2 Electrical resistivity ρ (upper panels a-c) and Sommerfeld coefficient of the heat capacity C/T (lower panels d-f) for three typical samples of YFe$_2$Ge$_2$ with different residual resistivity ρ_0. Sample #34 (as-grown) derives from the same ingot as a bulk superconducting annealed sample, for which the data is presented in Fig. 4.5. All three samples show resistive superconducting transitions, but a heat capacity anomaly indicating bulk superconductivity only appears in the purer samples #37 and #73. While a supserconducting heat capacity anomaly is absent, C/T of sample #34 (as-grown) displays a slow increase even in magnetic fields sufficient to suppress T_c fully, suggesting an underlying magnetic contribution.

treatment. Full resistive transitions are observed in most samples with RRR values exceeding 20.

Key features of resistivity and heat capacity data are further illustrated in Fig. 4.2. The as-grown (unannealed) sample (#34) shows a resistive superconducting transition, but no superconducting anomaly in the heat capacity (see Fig. 4.2 (a, d)). This sample derives from the same ingot as the annealed sample that shows the superconducting heat capacity anomaly in Fig. 4.5. We find more generally that unannealed samples have low RRR values, and while some show a resistive transition all lack superconducting heat capacity anomalies. By contrast, all of the annealed samples show resistive superconducting transitions with varying T_c, but not all exhibit signatures of bulk superconductivity in their specific heat (e.g. [22]). Distinct heat capacity anomalies, namely broad jumps in $C(T)/T$ near 1 K, peaking at about
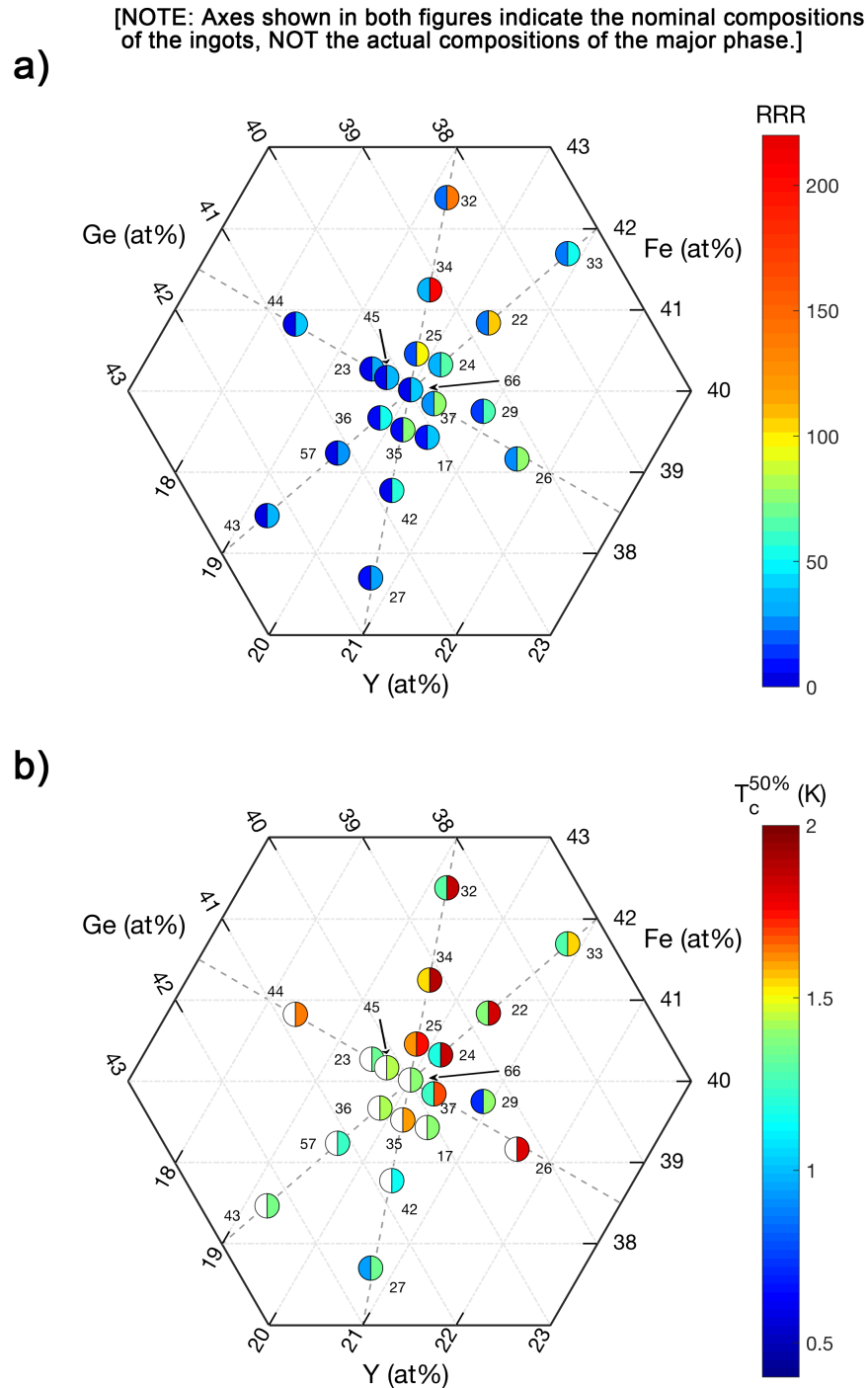
Fig. 4.3   a) Residual resistivity ratio RRR= $\rho(300\,\mathrm{K})/\rho(2\,\mathrm{K})$ and b) Resistive superconducting transition temperature (mid-point) $T_c^{50\%}$ of polycrystalline $Y_{1+x}(Fe_{1+y}Ge_{1+z})_2$ on ternary diagrams. Positions of circles on the diagrams indicate the nominal compositions, with labels corresponding to batch numbers. The colours of the left semi-circles represent RRR or T_c of as-grown samples and those on the right semi-circles correspond to the annealed samples. White colour indicates that no transition is observed. Data plotted in this figure have been summarised in Table B.1 in Appendix B.

20% above the normal state values, are observed in high-quality samples with RRR above 120 (see Fig. 4.2 (c, f) and Fig. 4.5). Less prominent anomalies with peaks roughly 10% above the normal-state $C(T)/T$ can be found in samples with RRR ranging from 60 to 120, as illustrated in Fig. 4.2 (b, e).

To visualise the dependence of sample quality on compositions and heat treatment, we summarise the results of RRRs and resistive $T_c^{50\%}$s for 20 ingots in ternary diagrams Fig. 4.3. The position of each coloured circle on the ternary axes represent the investigated nominal composition. The colours of the left half circles correspond to the as-grown samples, while the right halves give values for the annealed samples. A white half-circle on the T_c plot suggests that the sample did not show superconductivity. Since variations also occur amongst samples selected from the same ingot, all data shown in the ternary plots represent the highest values (of RRR or T_c) observed for the corresponding compositions. Data used for plotting Fig. 4.3 have been summarised in Table B.1 in Appendix B.

The striking effect of heat treatment at 800 °C is illustrated by both the appreciable increases in RRRs and T_cs with annealing and the appearance of superconductivity in samples that did not superconduct (down to 0.4 K) prior to annealing. These improvements in sample quality can be understood in terms of the reduction of disorder, created due to fast quenching during growth. Further annealing at 800 °C for an additional 7 days did not result in noticeable improvements in sample quality of the already annealed samples. It should also be noted that no specific heat superconducting anomalies are found in any of the as-grown samples.

Besides the effectiveness of annealing, Fig. 4.3 also indicates that the primary cause of the differences in sample quality is the ratio of Fe vs. Ge content in the melt: along the line of constant Y content (running diagonally to the top-right of the figure), both RRR and T_c show the largest variation, and growth from an Fe-rich, Ge-poor melt results in higher RRRs and T_cs. In particular, the highest RRR of 211 was observed in a sample selected from the annealed Y(Fe$_{1.05}$Ge)$_2$ ingot (# 34) which also exhibits an enhanced T_c of 1.87 K (Fig. 4.5).

4.2 Superconductivity in YFe$_2$Ge$_2$

Once the best nominal composition (YFe$_{2.1}$Ge$_2$) was identified, samples from this annealed ingot were taken for further investigation. The electrical resistance of the sample with RRR = 211 was measured using a standard four-terminal ac technique in an adiabatic demagnetisation refrigerator to 0.1 K and in a QD PPMS to below 0.4 K (measurements performed by Dr. Konstantin Semeniuk). The magnetisation data of a sample with RRR = 185 were acquired using a Cryogenic SQUID magnetometer to below 0.31 K (measurement
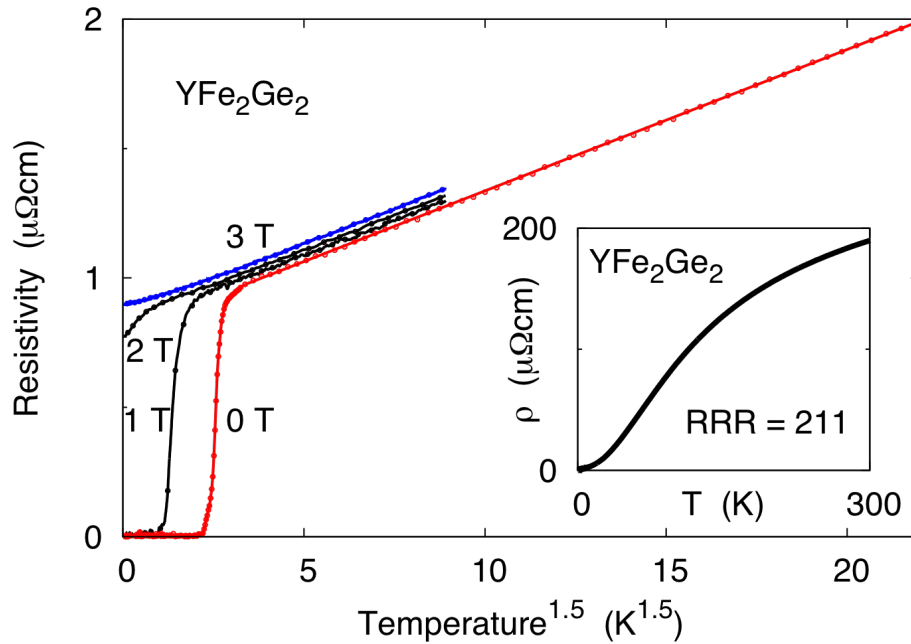
Fig. 4.4 Electrical resistivity of high-quality YFe$_2$Ge$_2$ polycrystal versus temperature, displaying a sharp superconducting drop of the resistivity with midpoint at 1.83 K below a $T^{1.5}$ normal state temperature dependence. (inset) Temperature dependence of the resistivity up to room temperature. (Figure credit: [23])

by Dr. Philip Brown). The data were corrected for the effect of demagnetising fields by approximating an ellipsoidal sample shape. The specific heat of the same sample was measured in a PPMS to below 0.4 K.

A sharp resistive transition is observed below 1.87 K for the sample shown in Fig. 4.4 (# 34, annealed). Under applied fields, the transition is suppressed to lower temperature and diminishes above 2.5 T. Only an insignificant positive magnetoresistivity is observed in the normal state while the resistivity maintains the $T^{3/2}$ anomalous power-law dependence. Fig. 4.5 shows C/T versus temperature for the sample with second highest RRR of 185. The Sommerfeld ratio C/T, which is enhanced by an order of magnitude over the band structure value of $\simeq 10$ mJ/molK^2 [35, 36], rises below T_c, peaks at about 20% above the normal state value near 0.9 K and then decreases rapidly. Applying magnetic field ($B = 2.5$ T) fully suppresses the heat capacity anomaly, allowing a view of the underlying normal state, which is nearly constant below 2 K. SQUID magnetometry on the same sample (Fig. 4.5) reveals a superconducting volume fraction approaching 100%.

More information about the superconducting state can be inferred from its response to applied magnetic field. In these samples, the initial slope of the resistive upper critical field
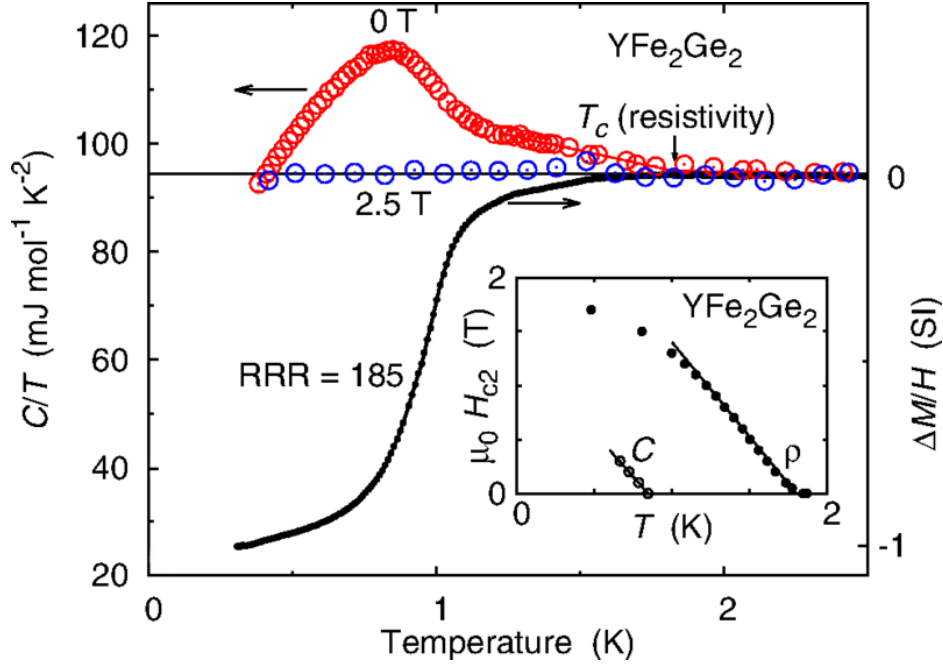
Fig. 4.5 C/T and magnetisation of YFe$_2$Ge$_2$ versus temperature showing anomalies characteristic of bulk superconductivity. The background-subtracted zero-field-cooled low temperature dc magnetisation ΔM divided by the applied field $\mu_0 H = 0.5\,\text{mT}$ of the same sample displays a step with midpoint at $\simeq 0.95\,\text{K}$, which coincides with the steepest descent in C/T. The size of the step corresponds to $(95 \pm 5)\%$ diamagnetic screening. (inset) Temperature dependence of the upper critical field determined from the midpoint of resistive transitions (labeled ρ) and from the peak in C/T (labeled C). (Figure credit: [23])

is determined as $|dB_{c2}/dT| \simeq 1.75\,\text{T/K}$ (inset of Fig. 4.5). This corresponds to an extrapolated clean-limit weak-coupling orbital-limited critical field $B_{c2}^{(o)} \simeq 0.73 T_c |dB_{c2}/dT| \simeq 2.3\,\text{T}$, slightly below the value reported in Ref. [22] for a sample with a lower T_c. In the standard treatment (e.g.[40]), the orbital-limited resistive critical field in YFe$_2$Ge$_2$ of $\simeq 2.3\,\text{T}$ corresponds to a superconducting coherence length $\xi_0 = (\Phi_0/(2\pi B_{c2}^{(o)}))^{1/2} \simeq 120\,\text{Å}$, where $\Phi_0 = h/(2e)$ is the flux quantum. By following the peak in C/T with applied field, which has an initial slope of $\simeq 1.7\,\text{T/K}$, we can similarly extract an estimate of $\xi_0^C \simeq 180\,\text{Å}$ for the coherence length associated with the bulk transition. Such a short coherence length might be expected to result from the enhanced quasiparticle mass and consequently low Fermi velocity indicated by the high Sommerfeld coefficient.

4.3 Disorder effect on T_c

The influence of disorder scattering on superconductivity in YFe_2Ge_2 can be examined
quantitatively using the large number of samples (annealed and as-grown) prepared from
more than 20 ingots grown for this study. The dependence of the resistive T_c on residual
resistivity ρ_0 is summarised in Fig. 4.6, which illustrates that the data can be modelled by the
implicit Abrikosov-Gor'kov expression [57]

$$\ln\left(\frac{T_{c0}}{T_c}\right) = \Psi\left(\frac{1}{2} + \frac{\alpha T_{c0}}{2\pi T_c}\right) - \Psi\left(\frac{1}{2}\right),\tag{4.1}$$

where T_c and T_{c0} are the actual transition temperature and the optimal transition temperature
without impurity scattering, respectively, $\alpha \propto \rho_0$ measures the pair-breaking effect of impurity
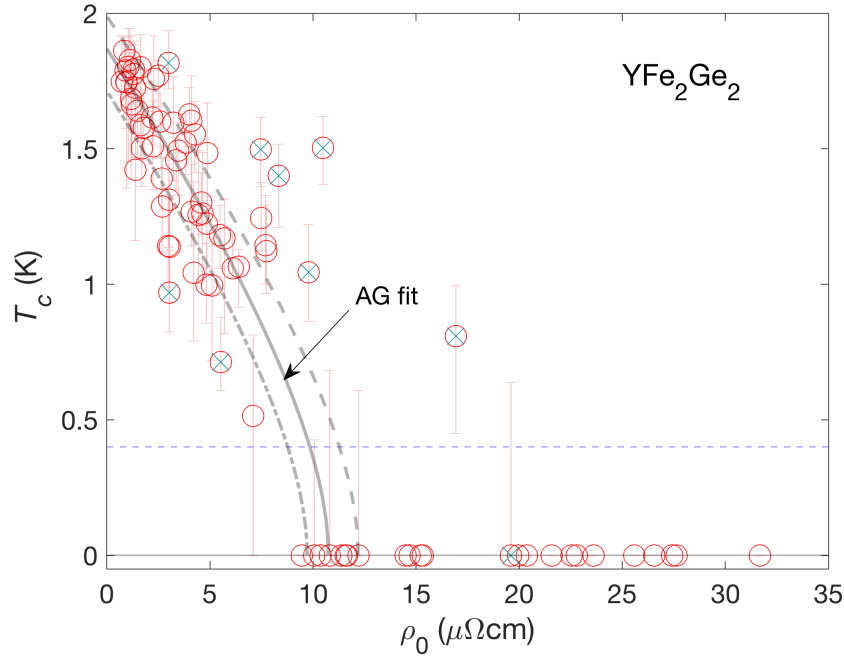
Fig. 4.6 Resistive superconducting transition temperature T_c (50%-point) and
the transition width (80%/20% criterion) versus the residual resistivity ρ_0 for all
YFe_2Ge_2 polycrystalline samples characterised. T_cs below 0.4 K (blue dotted line)
are shown as zero on the plot but not used in the curve fitting. The grey solid,
dash and dash-dot curves are least-square fits of the Abrikosov-Gor'kov function,
described in the main texts, to the 50%, 80% and 20% T_c points correspondingly.
Data points marked by the green crosses are excluded in the fittings.

scattering and $\Psi(z)$ is the digamma function. This approach has been found to describe the experimental data on cuprates [59, 93], the spin-triplet superconductor Sr$_2$RuO$_4$ [94, 87] and the heavy fermion superconductor CeCoIn$_5$ [95]. Impurity scattering is expected to suppress an unconventional pairing state, when the pair-breaking parameter $\alpha = \frac{1}{2}\frac{\hbar\tau^{-1}}{k_B T_{c0}}$ approaches 1 [59, 96, 58], where, τ^{-1} is the quasiparticle scattering rate. Our data suggest an optimal T_{c0} of 1.87 K and show a clear trend for T_c to diminish with increasing ρ_0 and superconductivity to be suppressed when $\rho_0 > 10.7\,\mu\Omega$ cm.

The scattering rate can be estimated from ρ_0 using the Drude result $\tau^{-1} = \varepsilon_0 \Omega_p^2 \rho_0$, where Ω_p is the renormalised plasma frequency, which is reduced with respect to the bare plasma frequency obtained from a DFT calculation, $\Omega_p^{(0)}$, by the ratio of effective mass m^* over band mass m_0: $\Omega_p^2 = (\Omega_p^0)^2 \frac{m_0}{m^*}$. Estimating $(\Omega_p^{(0)})^2 = ((\Omega_x^{(0)})^2 + (\Omega_y^{(0)})^2 + (\Omega_z^{(0)})^2)/3 \simeq (3.43\,\text{eV}/\hbar)^2$ on the basis of DFT calculations [36], and taking the mass enhancement from the ratio of experimental Sommerfeld coefficient $\gamma_{exp} \simeq 100\,\text{mJ/molK}^2$ over its DFT counterpart $\gamma_0 \simeq 12.4\,\text{mJ/molK}^2$ [36] to be $\frac{m^*}{m_0} \simeq 8$, we find that $\hbar\tau^{-1} = \rho_0 \varepsilon_0 \hbar \Omega_p^2 = 0.197\,\text{meV}(\rho_0/\mu\Omega\,\text{cm})$. For an optimum $T_{c0} \simeq 1.87$ K, this gives $\alpha = 0.62(\rho_0/\mu\Omega\,\text{cm})$, which would suggest that superconductivity should already be fully suppressed when ρ_0 exceeds about $1.6\,\mu\Omega$ cm. This contrasts with the threshold of $10\,\mu\Omega$ cm for full resistive transitions. The resistive transition, although eventually suppressed, is therefore more robust than might be expected, which may indicate that percolating superconducting paths through high purity regions of a sample can be found even in samples in which the averaged resistivity ratio is comparatively low. The experimental observation that residual resistivities of less than $2\,\mu\Omega$ cm are required to observe *thermodynamic* signatures of the superconducting phase transition, by contrast, is fully in line with this analysis.

An independent criterion for the limiting disorder scattering can be obtained by considering the mean free path rather than the scattering rate, and comparing it to the superconducting coherence length: the BCS coherence length $\xi_{BCS} = \frac{\hbar v_F}{\pi\Delta}$ [40, 97], where v_F is the quasiparticle (renormalised) Fermi velocity and $\Delta = \eta k_B T_{c0}$ (with $\eta = 1.76$ in weak-coupling BCS theory) is an estimate of the energy gap, can be compared to the mean free path $\ell = v_F \tau$ to give:

$$\xi/\ell = \alpha \frac{2 k_B T_{c0}}{\pi\Delta} \simeq \frac{2}{\pi\eta}\alpha \ . \tag{4.2}$$

Taking the critical value for the pair-breaking parameter α to be ~ 1 and $\eta \simeq 2$ then implies that ℓ has to be about four times larger than ξ for superconductivity to be observed. As the experimental value for the coherence length based on the observed upper critical field for bulk superconductivity is $\xi \simeq 180\,\text{Å}$ (see Section 4.2), bulk superconductivity would then require $\ell > 600\,\text{Å}$. An estimate can be obtained for v_F by combining the density of states

per unit volume (from the experimental C/T) and the renormalised plasma frequency, via $\left\langle v_F^2 \right\rangle = \frac{3\varepsilon_0}{e^2} \frac{\Omega_p^2}{g(E_F)}$ (e.g. [98]) as $v_F \simeq 3.3 \times 10^4 \, \mathrm{m/s}$. With the expression for τ given above, we obtain the estimate

$$\ell = \left(\frac{3}{\varepsilon_0 e^2 g(E_F) \Omega_p^2} \right)^{1/2} \frac{1}{\rho_0} = 1100 \, \text{\AA} (\rho_0 / \mu\Omega \, \mathrm{cm})^{-1} \, . \tag{4.3}$$

For a required mean free path of $600 \, \text{\AA}$, this translates to a critical resistivity $\rho_0 = 1.8 \, \mu\Omega \, \mathrm{cm}$, slightly larger than the value found by comparing the relaxation rate to $k_B T_{c0}$ directly.

4.4 Structural investigation

Powder X-ray diffraction (XRD)

For determining the lattice parameters and identifying secondary phases, powder X-ray diffraction (XRD) pattern for all annealed ingots were collected in the Bragg-Brentano geometry with a Cu Kα radiation at 40 kV and 40 mA on a Bruker D8 diffractometer equipped with a Lynxeye XE detector to reduce the effects of Fe fluorescence and Kβ radiation. The XRD spectrum was obtained from $10°$ to $120°$ in 2θ with $0.005°$ step size, 0.5 seconds/step. The FULLPROF program was used for performing Rietveld refinements on the X-ray powder intensity patterns. Quantitative analysis of alien phases' weight-percentages were carried out on patterns obtained without internal standards, while lattice parameters were determined by referring to an internal Ge standard and using the Le Bail method. Multiple measurements were performed on selected batches of samples for determining the typical uncertainties on lattice parameters. Furthermore, energy dispersive spectroscopy (EDS) was used for probing the actual compositions of the highest- and lowest-quality samples. This was performed with an Oxford X-Max detector in an FEI/Philips XL-30 ESEM at 30 kV and analysed with the INCA software.

To sample the ternary phase diagram near the stoichiometric composition of YFe$_2$Ge$_2$, we varied the nominal stoichiometry by approximately $\pm 2\%$, $\pm 5\%$ and $\pm 10\%$ in each of the elements, and also prepared some nominally stoichiometric ingots. Table. 4.1 lists the ingot numbers, their nominal compositions and the impurity phase contents estimated from powder X-ray diffraction. The formation of impurity phases from off-stoichiometric melts is a natural consequence of the narrow homogeneity range of YFe$_2$Ge$_2$.

The partial ternary phase diagram Fig. 4.7 shows the secondary phases found in ingots of different nominal compositions. Away from the 1-2-2 composition, five main secondary phases have been found and only three of them were identifiable from the database of known

Table 4.1 Nominal compositions of all ingots with corresponding labels shown in Figs. 4.3 and 4.7. For each ingot, the table lists the alien phase content as estimated from powder X-ray diffraction measurements.

Ingot No. #	Nominal Composition $Y_{1+x}[Fe_{1+y}Ge_{1+z}]_2$			Impurity Phases (wt.%)				
	x (%)	y (%)	z (%)	YFeGe$_2$	YFe$_6$Ge$_6$	Fe (bcc)	Phase (A)	Phase (B)
26	10.1	0	0.3	-	-	-	10 - 20	10 - 20
29	5.2	0	-1	-	< 1	-	-	-
37	2.1	0	-0.1	-	-	-	-	-
45	-2.1	0	0	-	17.5	-	-	-
23	-3.4	0	0	8.1	21.7	-	-	-
44	-10	0	0	-	32.4	-	-	-
32	0	10.3	0	-	-	2.7	-	-
34	0	5.3	0	-	-	1.5	-	-
25	0	1.9	0	-	-	< 1	-	-
35	0	-2	0	2.7	4.3	-	-	-
42	0	-5.1	-0.1	8.1	4.6	-	-	-
27	0	-9.1	0.2	13.1	-	-	-	-
43	0	-0.1	9	10.8	19	-	-	-
57	0	0	4.9	13.1	44	-	-	-
36	0	-0.1	2	1.8	7.3	-		-
24	0	0	-2.1	-	-	< 1	< 1	< 1
22	0	0	-5.2	-	-	1.1	< 1	-
33	0	0	-10.1	-	-	-	10 - 20	10 - 20
66	0	0	0	-	6.1	-	-	-
72[a]	0	0	0	-	1.4	-	-	-
73[a]	0	5.0	0	-	-	< 1	< 1	-

[a]Samples grown with 4N yttrium
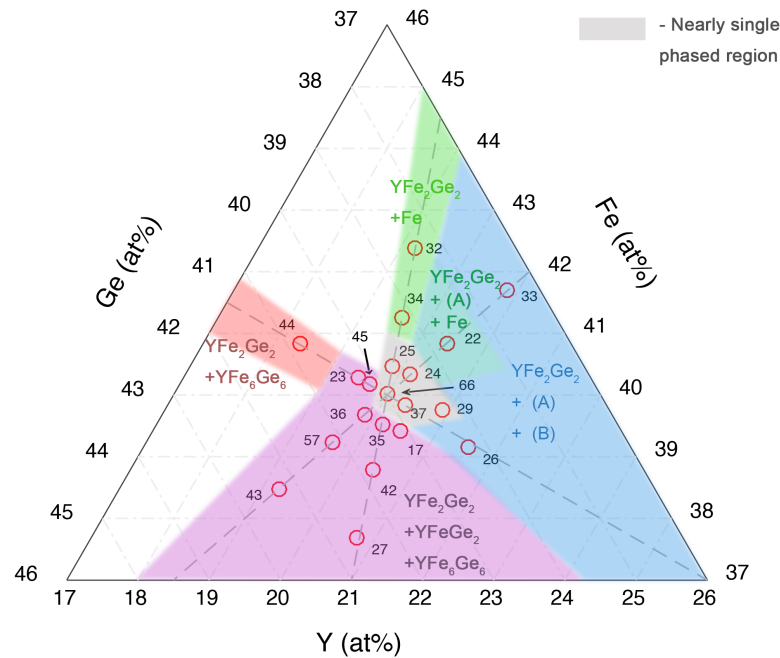
Fig. 4.7 Putative phase diagram of Y-Fe-Ge near stoichiometric YFe_2Ge_2 inferred from powder X-Ray diffraction measurements (Table. 4.1) of polycrystalline $Y_{1+x}(Fe_{1+y}Ge_{1+z})_2$ samples. Phases (A) and (B) have not been successfully identified.

compounds, namely YFe_6Ge_6, $YFe_{1-x}Ge_2$ and Fe (bcc). We denote the two unknown phases (A) and (B). Phase (A) shows spectrum peak positions close to those of YFe_4Ge_2 [99] but with mismatching ratios of peak intensities, whereas phase (B) is likely to be a compound with higher yttrium concentration than YFe_2Ge_2 according to our EDS studies. No potential candidate for phase (B) can be found in the literature. While no clear correlation can be deduced between the amount of impurity phases and the superconducting properties, the best samples featured by their high RRRs and T_cs are mainly located in the nearly single-phased region and the region for which Fe (bcc) is the main impurity phase.

In Fig. 4.8, the lattice parameters of the main phase in the annealed ingots were plotted against their corresponding RRRs (we use the highest measured value for each ingot), with red errorbars indicating the typical scatter observed in selectively repeated measurements. This scatter results mainly from small variations in experimental conditions and sample inhomogeneities. There is a strong correlation between the c-lattice-parameters and the RRRs.
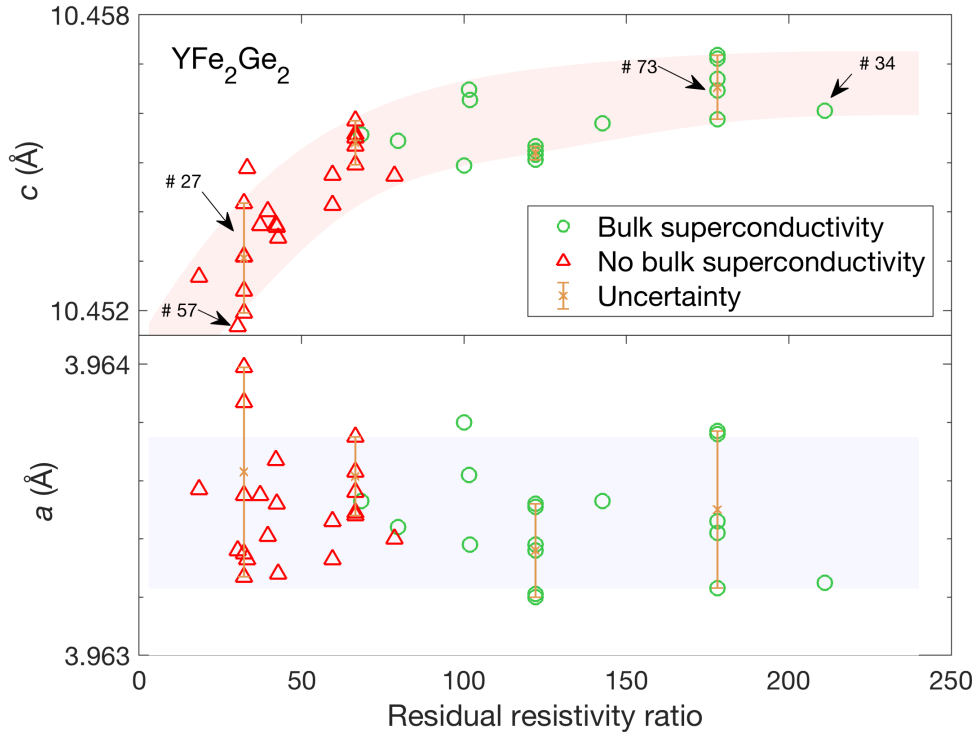
Fig. 4.8 Lattice constants c (upper panel) and a (lower panel) of the majority phase in each annealed batch of sample as obtained by XRD refinement, versus the corresponding RRR values. Green circles (red triangles) indicate that superconducting heat capacity anomalies have (have not) been observed. Errorbars are estimated from repeated measurements on the selected batches. The pink and blue shades are guide to the eyes. Data plotted in this figure have been summarised in Table B.2 in Appendix B.

Larger c-parameter is observed for the higher-quality samples, which show signatures of bulk superconductivity. On the other hand, no clear change is seen in the a-lattice-parameters.

Energy-dispersive spectroscopy (EDS)

To gain further understanding of the cause of varying c-parameters and RRRs, EDS measurements on samples showing the smallest (# 27 and 57) and largest (# 34 and 73) c-parameters were performed. Caution was taken in identifying regions free of secondary phases. Spectra were then obtained at spots of size $\sim 400\,\mu\text{m}^2$ over a few surface sites of each polished sample. Measurements were calibrated against elemental standards, so deviations from

Table 4.2 EDS analysis of four annealed polycrystalline YFe_2Ge_2 samples and polycrystalline $FeGe_2$ and Y_5Ge_3.

Ingot No. #	EDS measured composition [at.%][b]			Atomic ratios[c]		
(Spots probed)	Y	Fe	Ge	Fe:Ge	Fe:Y	Ge:Y
27 (N=88)	20.01(5)	38.50(5)	41.50(3)	0.928(2)	1.924(5)	2.074(5)
57 (N=71)	19.95(5)	38.56(4)	41.50(4)	0.930(1)	1.933(6)	2.080(6)
34 (N=66)	19.92(5)	38.92(5)	41.17(4)	0.945(2)	1.954(5)	2.067(6)
73 (N=59)	19.85(5)	38.98(5)	41.17(6)	0.947(2)	1.964(7)	2.074(7)
$FeGe_2$ (N=27)	-	32.46(3)	67.54(3)	$0.961(1)\times\frac{1}{2}$	-	-
Y_5Ge_3 (N=39)	60.56(6)	-	39.44(6)	-	-	$2.171(4)\times\frac{3}{10}$

[b]Values in brackets denote standard error of mean in the last digit.
[c]Values in brackets denote uncertainty in the last two digits estimated using propagation of error formula.

the actual composition are of the order of 2 at.%, as illustrated by EDS measurements on polycrystalline $FeGe_2$ and Y_5Ge_3 samples (Table. 4.2). However, relative differences in compositions can be measured to a much higher precision.

As shown in Table. 4.2, all four samples have similar Ge:Y ratios, while the Fe:Ge and Fe:Y ratios are noticeably higher in # 34 and 73. Knowing that both # 34 and 73 have relatively higher RRRs and larger c-parameters and assuming they are nearly stoichiometric, the EDS results point towards the presence of Fe-vacancies in samples with lower RRRs. Normalising the Fe:Y and Fe:Ge ratios of # 27 and 57 against the average of # 34 and 73, we estimate the Fe-vacancies to be about 2 to 3%.

4.5 Summary

Our study demonstrates that polycrystals of YFe_2Ge_2 with the lowest level of disorder can be grown by shifting the Fe/Ge ratio in the melt to favour full Fe occupancy on the Fe sites. Followed by annealing, which minimises anti-site disorder, this method produces samples with residual resistivities as low as $\sim 1\,\mu\Omega\,cm$, which exhibit superconducting anomalies in the heat capacity as well as in the resistivity. The strong correlation between the residual resistivity and T_c (Fig. 4.6) found by studying dozens of samples with a wide range of nominal compositions, both as-grown and annealed, is reminiscent of well-known unconventional superconductors such as Sr_2RuO_4 [94], $CeCoIn_5$ [95] and $YBa_2Cu_3O_{7-\delta}$ [100].

Varying the Fe/Ge ratio opens up the possibility of tuning the electronic and magnetic properties of YFe_2Ge_2, which according to DFT calculations [35, 36, 101] and recent neutron scattering experiments [38] is finely balanced close to several types of magnetic

order. However, in contrast to the situation of CeCu$_2$Si$_2$, which can be tuned between magnetically ordered and fully superconducting low temperature states by varying the sample composition [102], no magnetic transitions have been observed in any of our samples of YFe$_2$Ge$_2$. This is consistent with the comparatively high RRR observed in all annealed samples, which points towards a rather narrow homogeneity range that is probably too narrow to allow access to the magnetic sector of the low temperature phase diagram. A putative quantum critical point can be accessed by doping, as in the alloying series (Lu/Y)Fe$_2$Ge$_2$ [28], but no doped samples have shown any signatures of superconductivity, consistent with the view that disorder scattering rapidly suppresses superconductivity in YFe$_2$Ge$_2$.

Even the purest samples, as measured by ρ_0, display a striking separation between resistive T_c, which is as high as $\simeq 1.87\,\text{K}$, and the heat capacity anomaly, which occurs below about 1.1 K. This separation may be attributed to spatial inhomogeneity within the sample, but it will require further investigation to clarify whether the disorder level is inhomogeneously distributed or whether inhomogeneity of the sample strain may cause an enhanced T_c in small parts of the sample, contrasting with a much lower bulk T_c. Strain dependence of T_c and the presence of strained regions at the cut surface of single crystals has recently been shown to underlie the similar separation of resistive and bulk T_c in CeIrIn$_5$ [103].

Chapter 5

High-quality YFe$_2$Ge$_2$ single crystals

Previous studies on high-quality YFe$_2$Ge$_2$ polycrystals [23, 26] have established evidence of bulk superconductivity in this compound. However, polycrystalline samples are often disadvantageous for detailed investigations of the electronic properties and the superconducting pairing mechanisms, since the direction-dependent information is inherently lost due to the random orientations of the crystallites. Advanced experiments probing the low temperature state of YFe$_2$Ge$_2$, such as muon spin rotation, inelastic neutron scattering, and quantum oscillation measurements, had been held back by the lack of bulk superconducting, high-purity single crystals.

An early comprehensive growth study produced flux-grown single crystals [24] with comparatively high residual resistivity ratios RRR $\simeq$ 60 which displayed sharp resistive superconducting transitions. However, no bulk superconducting transition was observed in these crystals. Nevertheless, this growth study provided crucial clues regarding the importance of low growth temperature for the improvement of sample quality. Furthermore, the successful compositional study of YFe$_2$Ge$_2$ polycrystals (presented in Chapter 4) has illustrated the significance of controlling Fe concentration. We therefore devised new growth protocols for the flux growth of YFe$_2$Ge$_2$, which aimed at maintaining a high Fe concentration and a low growth temperature in the flux melt throughout the growth process.

In this chapter, I describe two flux growth methods which have allowed the growths of YFe$_2$Ge$_2$ single crystals with drastically improved sample qualities. Signatures of bulk superconductivity have been observed in thermodynamic, magnetisation and electrical transport measurements of these crystals. The best samples grown display residual resistivity ratios (RRR $= \rho_{300\,\mathrm{K}}/\rho_{2\,\mathrm{K}}$) up to 470 and show notably sharper superconducting specific-heat anomalies than our best polycrystals. Beyond the initial sample characterisations, in the later sections I present results of low-temperature specific heat, muon spin rotation and quantum oscillation measurements on this new generation of single crystals and discuss

their implications for the superconducting order parameter and the electronic structure of YFe$_2$Ge$_2$.

5.1 Crystal Growth and Characterisation

5.1.1 Background

Early literature on YFe$_2$Ge$_2$ [34] showed that single crystals can be produced using the standard method of flux growth as described in Section 3.1.2. The authors started with the elements in an atomic ratio of Y : Fe : Ge : Sn = 1 : 2.4 : 2 : 30. By first heating to 1200 °C and then slowly cooling to between 500 °C and 800 °C over 3-6 days, they were able to obtain sizeable YFe$_2$Ge$_2$ single crystals. However, their study on the properties of this compound was limited to temperatures above 2 K, so superconductivity was not investigated.

After the initial discovery of superconductivity in polycrystalline YFe$_2$Ge$_2$ [22], the flux growth method was revisited by H. Kim and others [24]. They attempted the growth by systematically varying the cooling rates, decanting temperatures and annealing procedures. However, they found no signatures of bulk superconducting transitions in specific heat measurements on any of their samples. Furthermore, a strong sample dependence of the resistive superconducting transition temperature T_c on the residual resistance ratio was observed, similar to what we found in the polycrystalline samples (e.g. in Section 4.3). Our early attempts in using the same flux method yielded similar conclusions.

As noted in Chapter 4, in order to observe the clear signature of bulk superconductivity in specific heat, samples with RRRs higher than ≈ 100 are required. However, the best samples produced with the standard flux method, either in our own attempts or those described in [24], showed highest RRRs of only ≈ 70. The lack of a bulk superconducting transition was hence not so surprising.

In order to devise a better scheme for growing high-quality single crystals, we have further scrutinised the procedures and results of our flux growths. Based on our studies of the polycrystals, YFe$_2$Ge$_2$ tends to grow with an iron-deficient composition, which appears to be detrimental to its superconductivity. Meanwhile, in all the flux growths of YFe$_2$Ge$_2$ performed up to this point, there were always secondary phases present in the products of the growths, most notably YFe$_6$Ge$_6$. This means that, despite having a higher concentration of Fe in the melt to start with, the actual ratio of Y : Fe : Ge in the Sn melt, when YFe$_2$Ge$_2$ crystals start to precipitate, may no longer be Fe-rich. This might have caused a slight change in the crystal composition, leading to their poor quality. With this idea in mind, a modified Sn-flux growth protocol was carried out. Later on, the partial success of this new protocol

also motivated us to perform a horizontal liquid transport growth which resulted in the highest quality single crystals.

5.1.2 Modified flux method

With the expectation that an undesirable change of composition inside the flux melt was the main obstacle to producing high-quality samples, our first objective was to maintain a relatively high Fe-concentration in the melt throughout the growth. To achieve this, the charge, namely the starting materials besides the Sn flux, was replaced with pre-reacted polycrystals, whose compositions were known to produce samples displaying bulk superconductivity. Furthermore, to avoid precipitation of secondary phases, the maximum temperatures of the growths were limited to $1000\,^{\circ}$C. This avoids complete dissolution of the polycrystals in the Sn flux. In fact, if the temperature is raised to $1200\,^{\circ}$C, as was the case in a standard flux method, the result would be the same as if separate elements were used as the charge.

Polycrystalline ingots with iron-rich nominal compositions were first grown using the induction furnace and annealed at $800\,^{\circ}$C as described in Section 4.1. These polycrystals were then powderised, added with additional iron powder, and placed together with Sn in a crucible. The crucible was further sealed in a quartz ampoule as in a normal flux growth. Powderising the polycrystals helps better dissolution in the flux and has the additional benefit that the highly-ordered tiny YFe_2Ge_2 crystals may act as seed crystals to facilitate the growth. In a similar spirit, repeated cooling and heating was carried out during the growth, with the hope that smaller crystals would dissolve during the heating phase, while the larger crystals
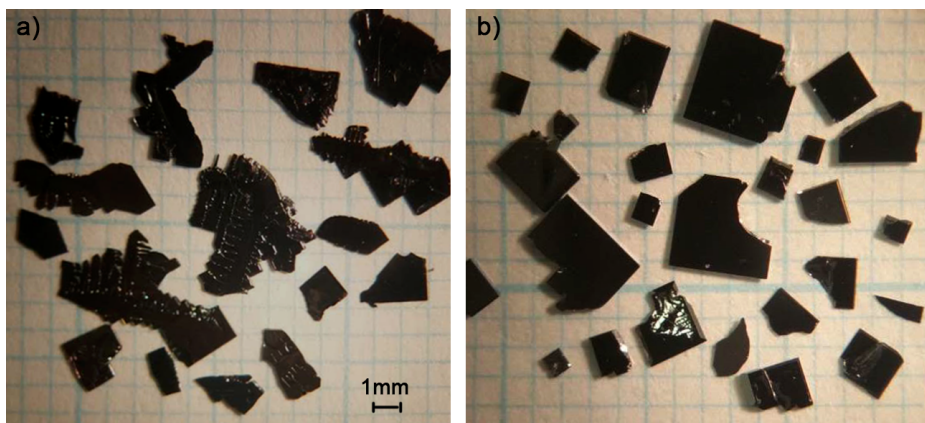
Fig. 5.1 Pictures showing (a) YFe_2Ge_2 single crystals grown with the conventional Sn-flux method using separate element as charge and (b) crystals grown with the modified flux method using polycrystal $YFe_{2+x}Ge_2$ as charge.

Table 5.1 Starting materials and temperature profiles for YFe_2Ge_2 sample batches grown using the conventional and modified Sn-flux methods.

Batch	Composition	Temperature Profile
SR1703	Y : Fe : Ge : Sn = 1.4 : 1.4 : 1 : 34	
SR1704	Y : Fe : Ge : Sn = 1.75 : 2.55 : 2 : 47	
SR1726	$YFe_{2+x}Ge_2$: Fe(powder) : Sn = 1 : 0.19 : 31	
SR1727	$YFe_{2+x}Ge_2$: Fe(powder) : Sn = 1 : 0.14 : 25	
SR1728	$YFe_{2+x}Ge_2$: Fe(powder) : Sn = 1 : 0.38 : 39	
SR1730	$YFe_{2+x}Ge_2$: Fe(powder) : Sn = 1 : 0.2 : 35	
SR1732	$YFe_{2+x}Ge_2$: Y : Fe(powder) : Sn = 1 : 0.1 : 0.1 : 29	
SR1823	$YFe_{2+x}Ge_2$: Fe(powder) : Sn = 1 : 0.4 : 39	

would remain and act as seeds in the cooling segments of the growth. Further details of the growths using this modified flux method are summarised in Table 5.1. This table also shows details of two flux growths using separate elements with atomic compositions significantly different from $Y : Fe : Ge : Sn = 1 : 2.4 : 2 : 30$. These were attempts to test the role of initial composition for the crystal quality. Throughout this chapter, we use sample labels composed of the growth batch label followed by additional numbers or letters which identify a particular piece of crystal from the corresponding growth batch.

Comparing visually the single crystals grown with the normal flux method using separate elements and the modified method (Fig. 5.1), we see that both methods produce platelet crystals, but the growth using the polycrystal charge results in crystals with nicer square edges and flat surfaces. In addition, **no secondary phases** appear in the growths using the modified method when the maximum temperatures were set $\leq 1000\,^\circ$C.

Characterisation

The electrical resistivity and specific heat of samples from the different growth batches listed in Table 5.1 were measured in the PPMS down to 400 mK (see Fig. 5.2). Resistivity was measured with current running parallel to the crystallographic ab-plane. The resistivity data were scaled at 300 K to the published high-temperature resistivity of $190\,\mu\Omega\,$cm [34] for ease of comparison with past results on polycrystals. (The same has been done in later sections for samples grown with liquid transport method.) Looking at the resistivity data, these samples exhibit a large variation in RRRs. Samples with a higher RRR generally also show a sharper superconducting transition and a higher resistive T_c. This is consistent with the study on polycrystalline samples in Chapter 4. Significant variations are also observed in specific heat below 2.5 K for crystals from different growth batches. Clear superconducting anomalies are observed for samples from the batches SR1726, SR1730 and SR1823, while samples from the batches SR1728 and SR1732 show less prominent C/T jumps. On the other hand, C/T of samples from the batches SR1703, SR1704 and SR1727 show only a small upturn down to 400 mK without an obvious transition. While samples within the same batch also display variations in both RRRs and heights of the C/T jump (see e.g. Fig. 5.3), the differences are much less significant than those between samples from different batches, for example, between SR1726 and SR1732.

By viewing the C/T and resistivity data together (Fig. 5.2), it is clear that a sample with a lower residual resistivity, or equivalently a higher RRR, exhibits a more prominent specific heat anomaly. This is again in accordance with the studies on polycrystal YFe_2Ge_2 in Chapter 4, where superconductivity is found to be strongly suppressed by impurity and lattice disorder.
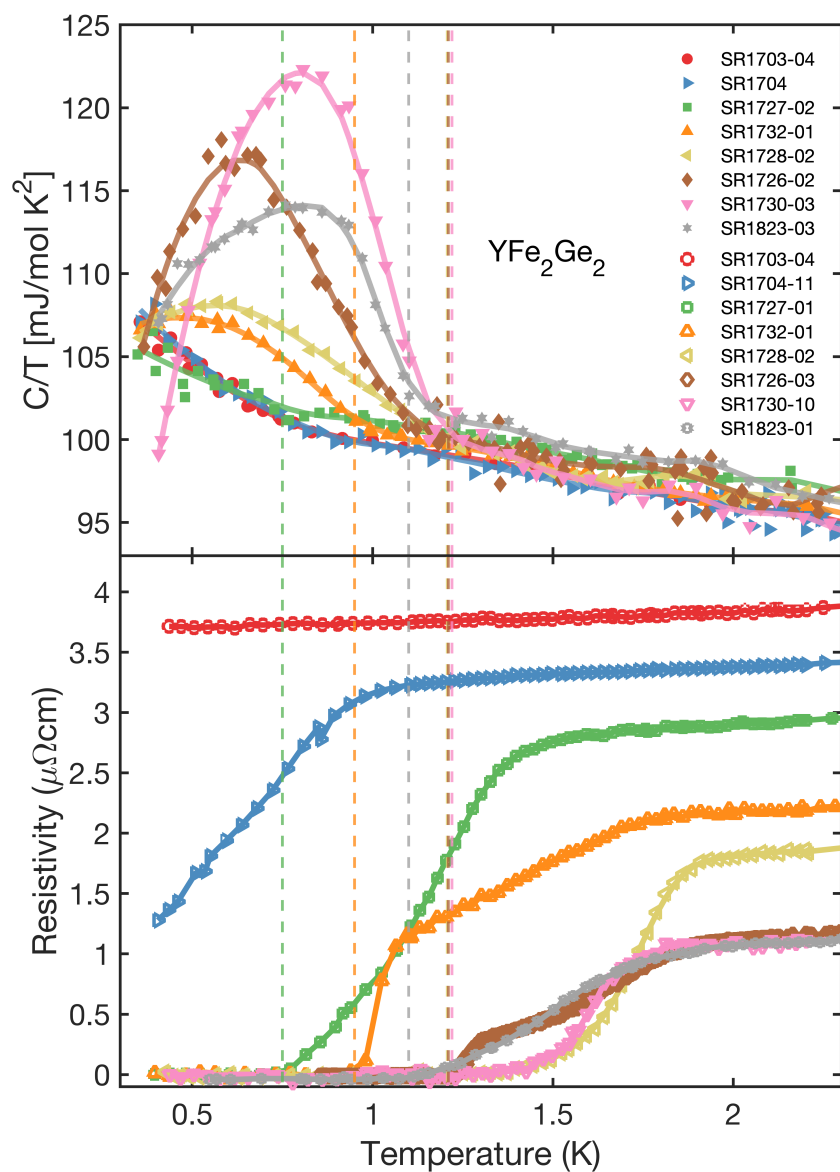
**Fig. 5.2** *C/T* (upper panel) and electrical resistivity (lower panel) of a selection of single-crystal YFe$_2$Ge$_2$ samples produced using the conventional and modified flux methods. These samples show a wide variations in their specific heat superconducting anomalies and residual resistivities. The vertical dashed lines are guide to the eye, indicating the temperatures at which resistivities drop to zero.

Looking at the lower panel of Fig. 5.2, we see that resistivities of all measured samples show either a relatively broad or a two-step superconducting transition. As indicated by the dash lines, the temperatures at which resistivity drops to zero for the intermediate and higher-quality samples coincide roughly with the onsets of the bulk transitions.

Similar to the resistivity of samples SR1732-01 and SR1726-02, two-step features of resistive transitions have also been observed previously in high-quality polycrystals, but only in small samples with dimensions of the order $200\,\mu m \times 100\,\mu m \times 50\,\mu m$ [104]. In the case of these single crystals, the sample dimensions are of the order $2\,mm \times 1\,mm \times 0.1\,mm$ or larger, suggesting that the proportions of the single crystals showing the higher-than-bulk T_c are much smaller than in those polycrystals. This casts some doubt on the validity of Fig. 4.6 as the intrinsic dependence of T_c on impurity and disorder scatterings. These higher-temperature transitions may come from filamentary, strain-stabilised superconductivity as initially suggested in [24] for explaining the lack of bulk transitions in poorer YFe_2Ge_2 samples.
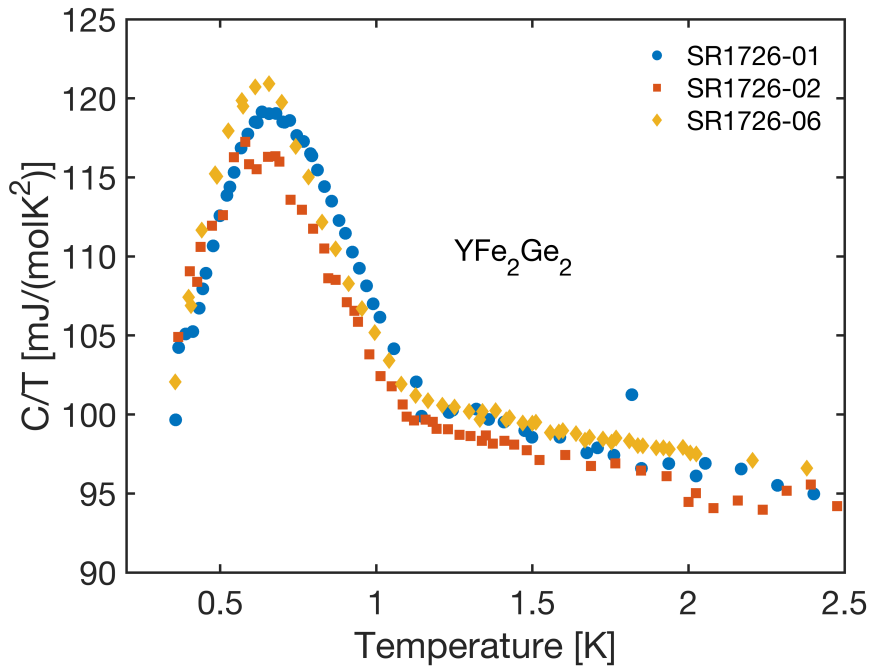

Fig. 5.3 C/T of three YFe_2Ge_2 samples from the growth batch SR1726 versus temperature. (Data for sample SR1726-01 has been scaled to account for a small amount of Sn inclusions.)
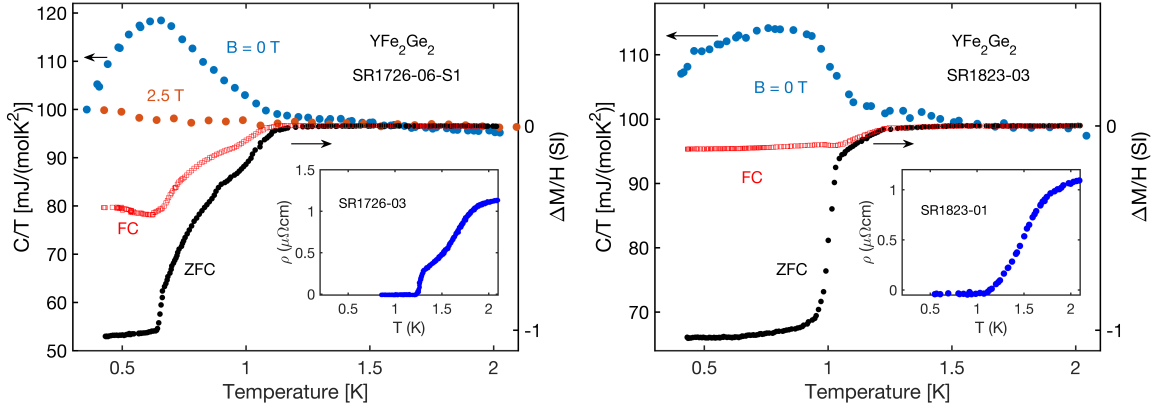
Fig. 5.4 C/T, magnetisation and resistivity (insets) of single-crystal YFe$_2$Ge$_2$ from growth batches SR1726 (left panel) and SR1823 (right panel) versus temperature showing signatures of bulk superconductivity. The field-cooled and zero-field-cooled dc magnetisations ΔM were measured for an applied field $\mu_0 H = 0.2$ mT.

The broadness of the C/T anomalies as shown in the upper panel of Fig. 5.2 is most likely a result of an inhomogeneous distribution of disorder. Compared to YFe$_2$Ge$_2$ polycrystals with RRR ≈ 200 (e.g. Fig. 4.5), the C/T jumps in samples from batches SR1726 and SR1730, which exhibit similar values of RRR, show much narrower widths and lower onset temperatures, suggesting a narrower distribution of disorder.

To further characterise the superconducting properties of the crystals grown using this modified flux method, magnetisation measurements were taken in the Cryogenic SQUID magnetometer with a helium-3 probe. The magnetisation curves $\Delta M(T)$ for samples from batches SR1726 and SR1823 are shown in Fig. 5.4. These data were collected on warm up from base temperature for both a field-cooled (FC) and a zero-field-cooled (ZFC) procedure. In the former case, a magnetic field of 2 G was applied before *cooling* the samples from 2 K, whereas in the latter case the same magnetic field was applied after reaching the base temperature of around 430 mK. Small effects of the demagnetising fields were corrected for both samples by approximating the sample shapes as rectangular prisms [105] – the dimension of SR1726-06-S1 is roughly 3.5 mm × 0.5 mm × 0.25 mm and the dimension of SR1823-03 is roughly 3.5 mm × 3.0 mm × 0.035 mm - with the largest side aligned in the direction of the applied magnetic field. To further account for a small background caused by a remnant field of the order of 0.5 Gauss, the zero-field cooling curve $M(T)$ is subtracted from

the warmup curves. The discrepancies between the ZFC and FC runs are generic features of type-II superconductivity when flux-pinning is present within the sample [106].

As seen in Fig. 5.4, samples from both batches show clear diamagnetic features with complete Meissner screening at the lowest temperatures. This suggests that the superconducting volume fractions reach 100% in both samples, at least below the bulk transition temperatures. Furthermore, the diamagnetic transitions are consistent with the bulk transitions observed in specific heat, with full screening at a temperature just below the peak of the specific heat jump. Comparing between data collected on samples from SR1726 and SR1823, we further notice that, while the RRR and the height of the specific heat jump are smaller in SR1823, the bulk transitions shown by the specific heat and magnetisation data are both much sharper. This may be a combined result of the differences both in the amount and in the distribution of disorder in the two batches.

Finally, in light of the varying specific heat and resistivity data shown in Fig. 5.2, we review the crystal growth conditions for all growth batches shown in Table 5.1. It appears that the key growth parameter which affects the crystal quality is the **maximum temperature reached during the growth**. This may be due to the combination of two factors. Firstly, the lower temperature stops precipitation of secondary phases and allows an Fe-rich concentration to be maintained throughout. Secondly, it is likely that the stoichiometric composition becomes thermodynamically more stable at lower temperatures, resulting in a more ordered lattice.

5.1.3   Liquid transport growth

The successful growth of bulk-superconducting YFe_2Ge_2 single crystals using the modified flux method has demonstrated the importance of controlling the charge composition in the flux melt and the growth temperatures. However, further adjustments of growth conditions in the same method, for examples the cooling rate, maximum temperatures and centrifugation (and hence dwelling) temperatures, did not improve the quality of the grown samples much further. Moreover, the need to stay below the temperature of complete dissolution of the charge meant that the quantity of yield in each growth was rather limited. The inherently continuous variation of the precipitation and growth temperatures also resulted in a relatively wide distribution in sample qualities even within each batch, illustrated by the differences in broadness of their bulk T_cs.

Encouraged by the partial success of the modified flux method and with an aim to produce a larger quantity of single crystals, an attempt was made to grow YFe_2Ge_2 using the liquid transport method introduced in Section 3.1.3. Knowing that the Fe-Ge composition plays an important role in the superconducting properties of the flux-grown crystals (see discussion

Table 5.2 Starting materials and temperature profiles for YFe$_2$Ge$_2$ sample batches grown using the liquid transport method. The upper temperature curve shows the profile of the hot zone of the two-zone furnace, whereas the lower curve shows the profile for the cold zone.

| Batch	Composition	Temperature Profile
JT1901	YFe$_{2+x}$Ge$_2$: Fe(powder) : Sn = 1 : 0.2 : 41	Hot zone: 650 °C, 460.4 h; 13.2 h up, 24.4 h down; Cold zone: 400 °C, 500 h; 20 h up, 40 h down; 25 °C to 25 °C
JT1902	YFe$_{2+x}$Ge$_2$: Fe(powder) : Sn = 1 : 0.13 : 103	Hot zone: 800 °C, 432 h; 9 h up, 18 h down; Cold zone: 500 °C, 459 h; 15 h up, 30 h down; 25 °C to 25 °C
JC1904	Y : Fe : Ge : Sn = 1 : 2.5 : 2 : 80	Hot zone: 700 °C, 444 h; 10 h up, 20 h down; Cold zone: 350 °C, 474 h; 10 h up, 20 h down; 25 °C to 25 °C
JC1908	YFe$_{2+x}$Ge$_2$: Fe(powder) : Sn = 1 : 0.43 : 122	Hot zone: 700 °C, 444 h; 10 h up, 20 h down; Cold zone: 350 °C, 474 h; 10 h up, 20 h down; 25 °C to 25 °C
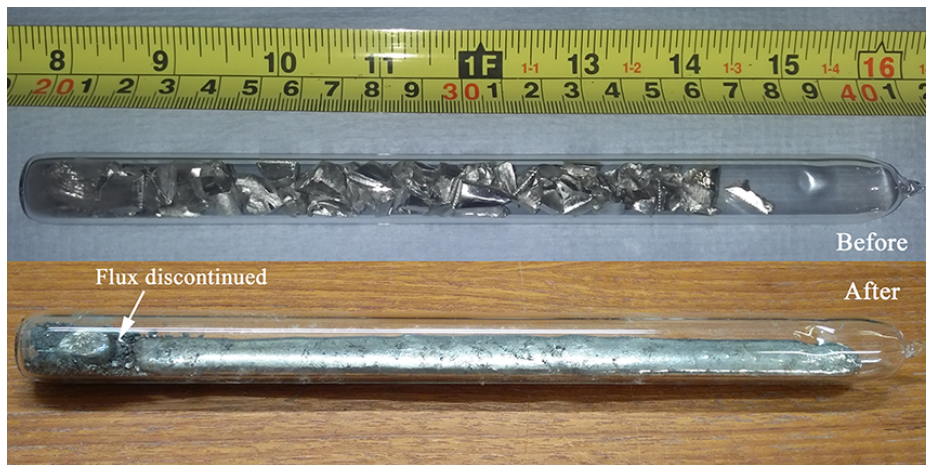
Fig. 5.5 Pictures showing the liquid transport growth ampoule for batch JT1901 before (upper panel) and after (lower panel) the growth. The flux is discontinued during growth due to the low growth temperatures and its insufficient volume.

in Section 5.1.4), annealed polycrystals, grown with the induction furnace, were again used as charge in the initial liquid transport growth. These polycrystals were known to show a broad bulk superconducting transition in specific heat measurements which peaks at around 1.1 K (e.g. in Chapter 4). Extra Fe powder was also added to further ensure an Fe-rich composition in the flux melt. However it was found later that the polycrystal precursors were **not** necessary for growing high quality samples and that using the separate elements as the charge gave the same results. Table 5.2 summarises three attempts using the polycrystal precursors and one attempt using separate elements as the charge. The first two growths were carried out with the help of James Tarrant, who was a Part-III project student in our group at the time.

In the initial attempt (batch JT1901), partially-powderised $YFe_{2.06}Ge_2$ polycrystals and Fe powder was loaded to one end of the quartz ampoule, and lumps of Sn were added to fill the length of the ampoule. The materials were then sealed under vacuum, as shown in the upper panel in Fig. 5.5. According to [24] and our previous experience with the modified flux-growths, a lower growth temperature tends to allow better quality single crystals, so the two zones of the tube furnace were set at 650 °C and 400 °C respectively. Due to the irregular shapes of the Sn lumps, the amount of Sn, when melted, only covers about 30% of the quartz ampoule volume. This has caused a disruption of the transport of charge halfway during the growth. In the lower panel of Fig. 5.5, it can be seen that the flux was discontinued near the cold end. As a result, most of the charge was unreacted and remained in the "hot end".
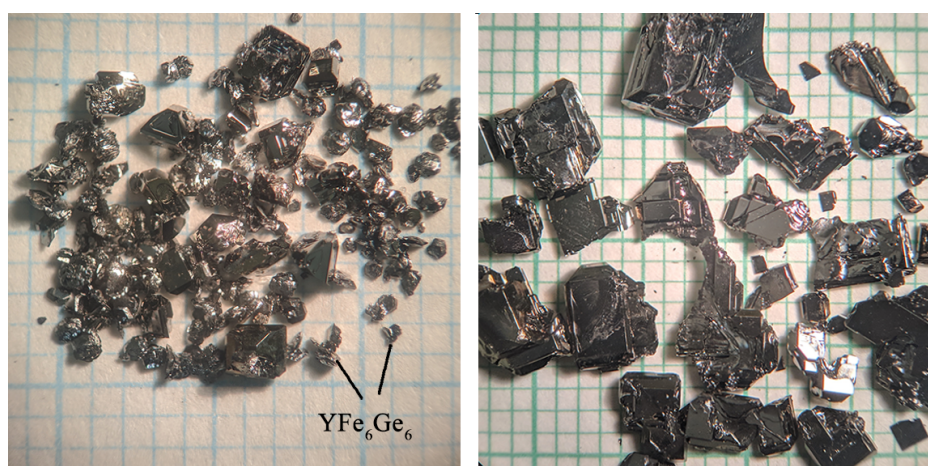
Fig. 5.6 Pictures showing YFe_2Ge_2 single crystals from the liquid transport growth batches JT1901 (left panel) and JT1902 (right panel). A significant amount of the secondary phase YFe_6Ge_6 are found in batch JT1901.

Crystals of YFe_6Ge_6 and a small amount of partially grown YFe_2Ge_2 crystals were found in the "cold end".

The undesirable outcomes of the first growth prompted us to set up a second attempt (batch JT1902) with a significantly increased amount of Sn flux and higher growth temperatures for ensuring continuous dissolution and transport of the charge. At the procedure of adding Sn into the quartz tube, Sn lumps were first loaded, up to the desired length, then the quartz tube was pumped out and heated with a flame torch to slightly above the melting point of Sn. This allowed close-packing of the Sn flux, freeing space for additional Sn to be added. Repeating this procedure enabled the increased volume of Sn in the second attempt. This procedure was also performed for the subsequent liquid transport growths.

Fig. 5.6 shows the resulted crystals from the two liquid transport growths. In JT1901, due to the disruption of the flux during growth, only part of the charge managed to diffuse to the cold end, resulting in a rather low yield. This most likely also caused an alteration of the charge composition in the melt. As a result, a large proportion of the crystals produced were YFe_6Ge_6. On the other hand, large crystals were produced in the batch JT1902, in which no YFe_6Ge_6 secondary phase was found. In a single growth, JT1902 yielded more than 1.5 g of YFe_2Ge_2 single crystals. Most of the larger crystals in JT1902 visually appear to be composed of multiple "grains" stacked together. However X-ray Laue imaging showed that the orientations of the "grains" within each crystal were indistinguishable within the resolution of our apparatus, suggesting that they are indeed single crystals.

The growths of batches JC1904 and JC1908 were carried out at the same time by placing both ampoules side-by-side in the tube furnace. The cold-zone temperature was set at $350\,^{\circ}\mathrm{C}$ while the hot zone was kept at $700\,^{\circ}\mathrm{C}$. The key difference between these two batches is the charge materials. For batch JC1904, separate Y, Fe and Ge elements were used as charge, whereas JC1908 started with polycrystals with nominal composition of $YFe_{2.06}Ge_2$. Samples from batches JC1904 and JC1908 have similar appearance to those from JT1902 as shown in the right panel of Fig. 5.6.

Characterisation

Specific heat measurements were taken for samples from all four growth batches listed in Table 5.2. Fig. 5.7 provides a direct comparison of the specific heat superconducting anomalies of four samples - one from each batch. Comparing data shown in Fig. 5.7 with those in Figs. 4.5 and 5.2, it is immediately obvious that samples grown with the liquid transport method display significantly shaper bulk transitions than previous samples. In addition, the jump heights at the transitions are around twice as large as those displayed by the best polycrystal samples and the best single crystals grown with the modified flux
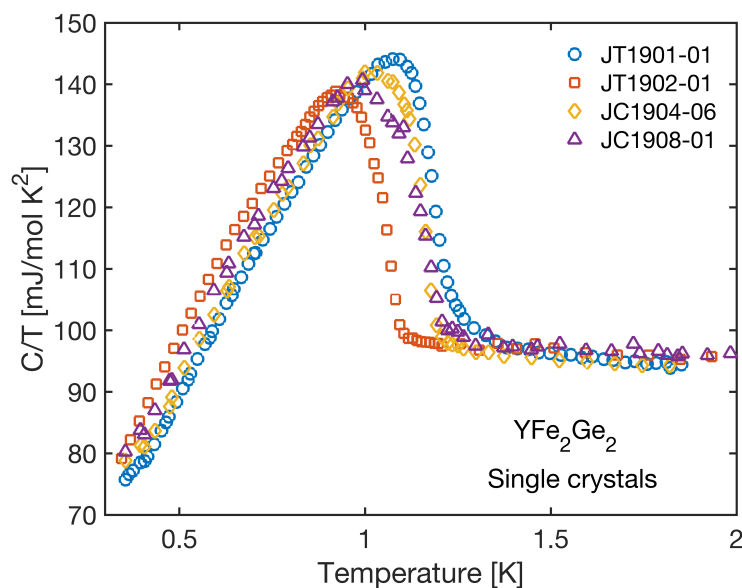

Fig. 5.7 C/T of YFe_2Ge_2 samples from four different batches grown using the liquid transport method, displaying differences in their bulk superconducting properties. (Data for sample JT1901-01 has been scaled to account for a small amount of Sn inclusions.)
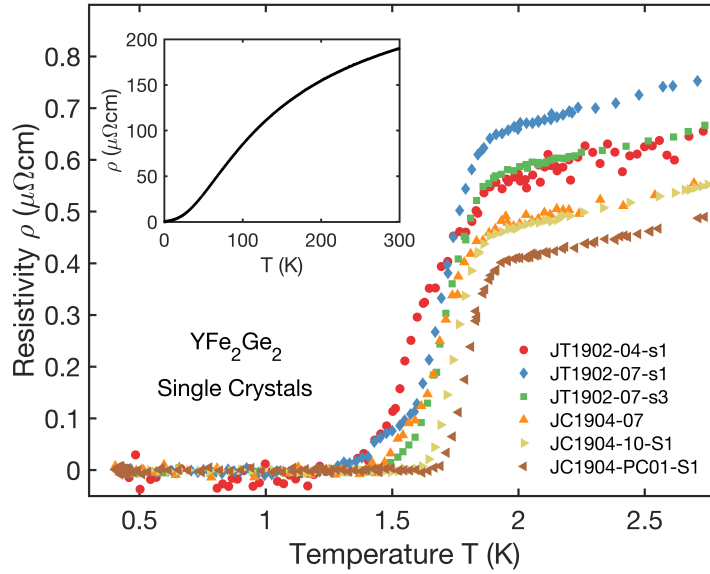
Fig. 5.8 Electrical resistivity ρ of multiple YFe$_2$Ge$_2$ samples from growth batches JT1902 and JC1904, displaying sample-dependence of electrical properties within each batch. (Inset) Typical high-temperature resistivity of YFe$_2$Ge$_2$ samples grown with the liquid transport method.

method. Surprisingly, samples from batch JT1901 show the highest T_c at around 1.2 K, while the batch JT1902 gives the lowest bulk transition temperature at around 1.1 K. This would suggest that, similar to the modified flux method described in the earlier sections, a low growth temperature may be the most crucial factor for producing high-quality samples.

Fig. 5.8 shows the results of resistivity measurements on a number of samples from batches JT1902 and JC1904. Again, when comparing with Fig. 5.2, it is easy to notice that samples grown with the liquid transport method exhibit a significantly lower residual resistivity. For example, the RRR of samples from JT1902 reaches as high as 330, whereas those from JC1904 is around 450 which is more than twice those shown by samples from SR1726. Both the specific heat and resistivity results indicate a drastic improvement in sample quality of crystals grown using the liquid transport method.

Magnetisation measurements (Fig. 5.9) also show very sharp superconducting transitions in the bulk of samples from batches JT1902 and JC1904. Full Meissner screening is observed at temperatures below the peak of the respective specific heat anomaly. Note that the applied magnetic field for the ZFC curve on the right panel in Fig. 5.9 is 5 G, rather than the 2 G field
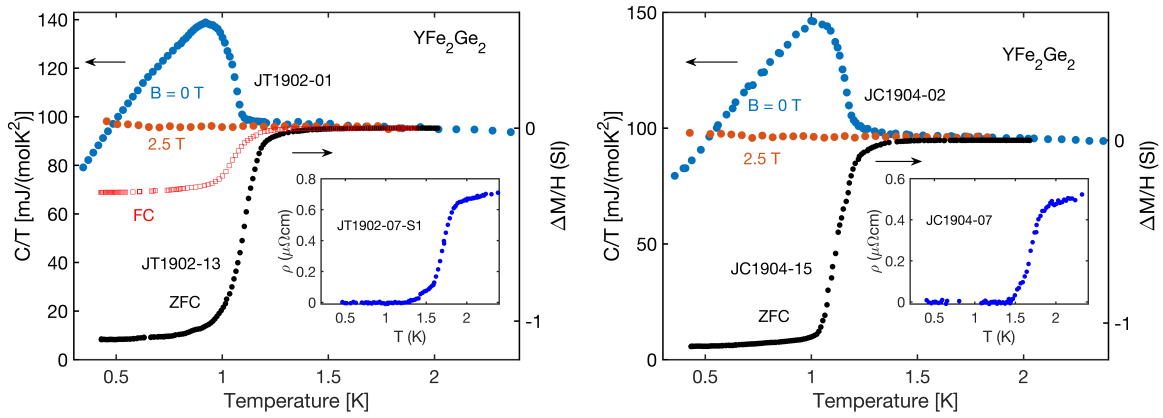
Fig. 5.9 C/T, magnetisation and resistivity (insets) of single-crystal YFe_2Ge_2 from growth batches JT1902 (left panel) and JC1904 (right penal) versus temperature showing clear signatures of bulk superconductivity. For sample JT1902-13, the field-cooled and zero-field-cooled dc magnetisations ΔM were measured with an applied field $\mu_0 H = 0.2$ mT, while for sample JC1904-15 ZFC ΔM was measured with an applied field $\mu_0 H = 0.5$ mT.
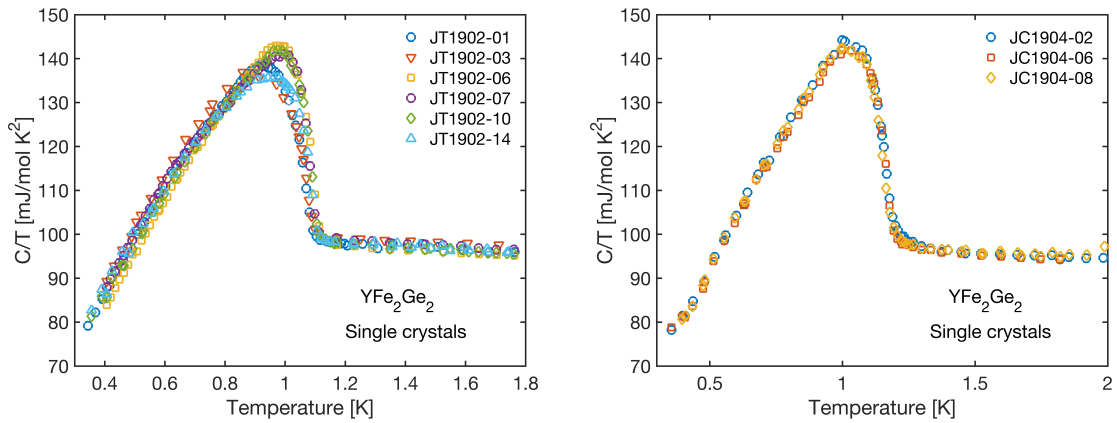

Fig. 5.10 C/T of multiple YFe_2Ge_2 samples from growth batches JT1902 (left panel) and JC1904 (right panel), displaying a slight sample-dependence of specific heat properties within each batch.

used in the measurements of the other samples. This may have caused the magnetisation transition to shift slightly to a lower temperature in the sample JC1904-15.

To check the homogeneity of samples grown using the liquid transport method, specific heat measurements were taken on multiple crystals from the batches JT1902 and JC1904. Fig. 5.10 show the results of these measurements. We see that only small variations occur in the specific heat anomalies displayed by the different samples in the batch JT1902, whereas data match up very well for samples taken from batch JC1904.

Due to the use of Sn flux in the liquid transport growths, it is rather common for the grown samples to enclose a small amount of Sn inclusions. For the specific heat measurements using the pulse-relaxation method, it is important to use samples with relatively large masses (e.g. above 5 mg) in order to reduce the measurement error due to the addenda. Therefore it can sometimes be difficult to avoid measuring samples which contain some Sn inclusions. From the specific heat data, the presence of Sn inclusions can be easily spotted, since the calculated normal-state C/T values per mole will be reduced. In cases where Sn inclusions are unavoidable (for example, all YFe$_2$Ge$_2$ samples in batch JT1901 contain trapped Sn), I have rescaled the C/T data by a constant factor to account for its reduction. This is justified for samples containing less than 5% of Sn inclusion, because even in the normal state, C/T of Sn is only ≈ 2 mJ/molK^2 below 2 K [107]. Its contribution to the total specific heat is therefore much less than the systematic error expected for the pulse-relaxation method, which is around 2%. In the magnetisation and resistivity measurements, samples have been carefully chosen, then cut or polished before measurement to remove any Sn inclusions.

5.1.4 Structural investigation

Single-crystal X-ray diffraction measurement

Obtaining single crystals with considerably different superconducting properties allows us to probe the structural causes of these differences through single crystal X-ray diffraction (SXRD) measurements. These measurements have been carried out on samples both showing and not showing signatures of bulk superconductivity. The measurements and analyses were performed by Dr. Monika Gamza from University of Central Lancashire. By the time this thesis is written, only samples grown with the standard and modified flux method, but not the ones from the liquid transport growth, have been probed with SXRD. Fig. 5.11 shows the typical single crystal diffraction pattern collected for two samples. For each pattern, over 95% of the reflections belonging to a single I4/mmm lattice can be indexed after neglecting Bragg peaks originating from the obviously different orientations.

The isotropic atomic displacement factor $B_{iso} = 8\pi^2 \langle \mu^2 \rangle$, where $\langle \mu^2 \rangle$ is the root mean square displacement of the atoms from their average position, can be related to reductions in intensity of the diffraction peaks due to atomic vibrations. It is expected that atoms with larger
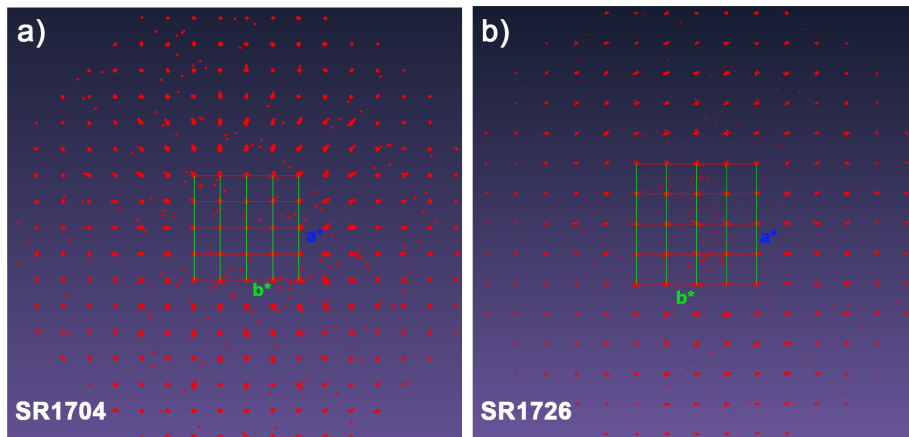
Fig. 5.11 Typical single-crystal XRD patterns in the reciprocal $a^* - b^*$ plane of YFe$_2$Ge$_2$ crystals, showing reflections mainly belonging to the I4/mmm lattice.

masses will exhibit lower values of B_{iso} at a given temperature. During the refinement of X-ray diffraction data, one method of checking whether a material has a near-stoichiometric composition is to allow the refinement of B_{iso} while setting all lattice sites at full occupancy. If there exists anti-site disorder or vacancies at certain site, B_{iso} for the element site will show an anomaly, which suggests the need for further refinement of the site occupancy. Therefore, through refinement of B_{iso}, the actual compositions of the crystals can be estimated. For example, for YFe$_2$Ge$_2$ samples with RRR $\approx$ 60 (from batch SR1704), initial refinement assuming full site occupancy results in B_{iso} factors which are nearly the same for Ge site with 0.3448(20) and Fe site with 0.3439(21), whereas that for the Y site has a smaller value of 0.3096(24), which is reasonable. A further refinement to achieve the lowest R value and more realistic ratios of B_{iso} for all sites is obtained when allowing a mixed but full occupancy of the Fe site by Fe and Ge atoms.

Table 5.3 shows the refined parameters for samples from four different batches. The refinement reveals a significant anti-site disorder with Ge occupying the Fe sites in the sample

Table 5.3 Results of refinement to single-crystal XRD data.

Sample	R(%)	B_{iso} for Y	B_{iso} for Fe	B_{iso} for Ge	Composition
SR1704	3.76	0.3029(25)	0.3562(25)	0.3362(21)	YFe$_{1.93(1)}$Ge$_{2.07(1)}$
SR1726	3.93	0.3422(19)	0.3762(18)	0.3537(17)	YFe$_2$Ge$_2$
SR1728	5.76	0.4451(27)	0.4997(26)	0.4747(23)	YFe$_2$Ge$_2$
SR1730	3.63	0.3817(27)	0.4322(20)	0.4015(18)	Y$_{0.991(2)}$Fe$_2$Ge$_2$

from batch SR1704 which is known to have a relatively low RRR ≈ 60, whereas no indication of such anti-site disorder is observed for the other samples from batches showing RRRs above 100. On the other hand, refinement on the sample from SR1730 shows a 1% yttrium vacancy. This is likely to be the result of the etching process for removing Sn-flux, which has inevitably reacted with the surface layer of the sample. Since only very thin samples were obtained from the batch SR1730, it was unavoidable that the surface layer would contribute significantly to the X-ray data.

Powder X-ray diffraction measurement

Powder XRD measurements have also been taken for single-crystal samples from different growth batches, which include samples grown with the liquid transport method. The lattice
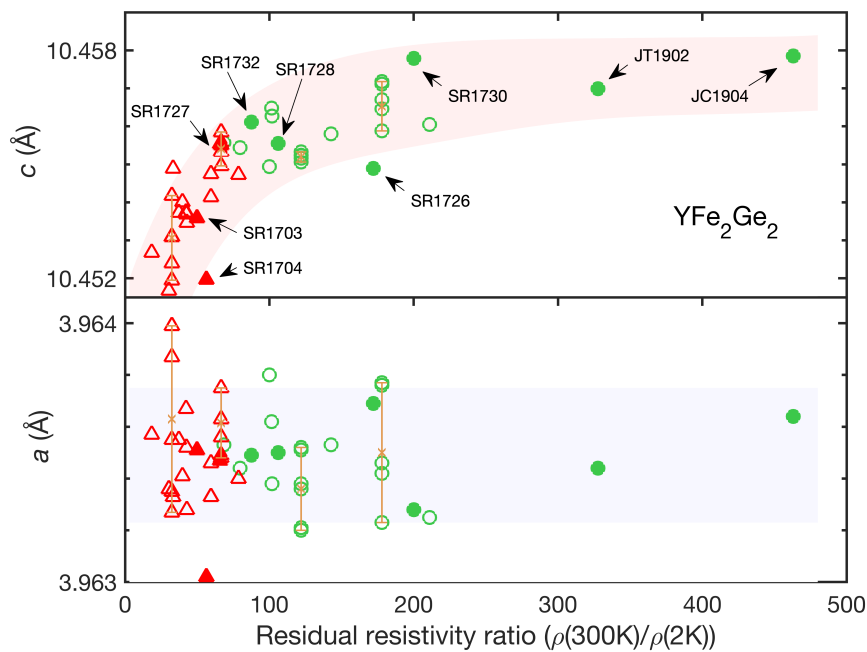
Fig. 5.12 Lattice constants c (upper panel) and a (lower panel) of both poly-crystal YFe$_2$Ge$_2$ (open symbols) and single-crystal YFe$_2$Ge$_2$ (solid symbols) samples, as obtained by powder XRD refinement, versus the corresponding RRR values. Green circles (red triangles) indicate that superconducting heat capacity anomalies have (have not) been observed. Errorbars are estimated from repeated measurements on the selected batches. The pink and blue shades are guide to the eyes. Data for the single crystal samples are summarised in Table B.3 in Appendix B.

constants against the typical RRR measured for the corresponding single-crystal batch are plotted in Fig. 5.12, together with earlier data obtained for the polycrystalline samples. We see that the c lattice parameter follows the general trend found in the study of the polycrystals [26]: larger c lattice constants are observed for samples with higher RRRs which are also more likely to show bulk superconductivity, whereas the a lattice parameter remains largely constant at $3.9535(5)$ Å.

Setting aside the fact that yttrium vacancy seems to be more significant in the sample from SR1730, the refined compositions from SXRD shown in Table 5.3 suggest that the dominant disorder effect which is detrimental to superconductivity in YFe_2Ge_2 results from anti-site disorder, in which the Fe-sites are partially occupied by Ge ions. This conforms with the trend observed in Fig. 5.12, in which samples with lower RRR have smaller c-lattice constants, since Fe-ions are larger in size than Ge-ions. The fact that samples with higher RRRs seem to have closer-to-stoichiometric compositions also further enhances confidence in the intrinsic nature of superconductivity in YFe_2Ge_2.

5.1.5 Critical fields

The upper and lower critical fields, B_{c1} and B_{c2}, are important fundamental parameters characterising a type-II superconductor. These values describe the field regime in which Abrikosov vortices are present inside the superconductor. In this subsection, we will investigate both of these quantities in the YFe_2Ge_2 samples grown by the liquid transport method.

The field dependence of the magnetisation in the superconducting state of a sample from the batch JT1902 was measured at a range of temperatures, with the external magnetic field applied along the crystallographic ab-plane. The left panel in Fig. 5.13 shows the different magnetisation isotherms. In the low-field region, a clear linear variation of the magnetisation (blue dash line) is seen, which is a signature of the Meissner state. The deviations of the magnetisation isotherms from this linear response are plotted in the right panel of Fig. 5.13. (Small kinks in the lower temperature data between 1.3 mT and 2.2 mT were due to saturation of the measured signal when using the high sensitivity setting on the magnetometer.) Estimates of the lower critical field B_{c1} at each temperature were determined by taking the fields at which such deviations cross $\Delta M = 10$ A m^{-1} (as shown by the yellow dash line). The extracted field values are plotted against the corresponding temperatures in Fig. 5.14. $B_{c1}(T)$ shows an upward curvature just below T_c and continues to increase as temperature is dropped. With the currently available data, it is difficult to predict the lower temperature behaviour of $B_{c1}(T)$ and estimate $B_{c1}(0)$.

Resistivity and specific heat below 2.5 K have been measured under applied magnetic field for several samples from batch JC1904 to investigate the temperature dependence of
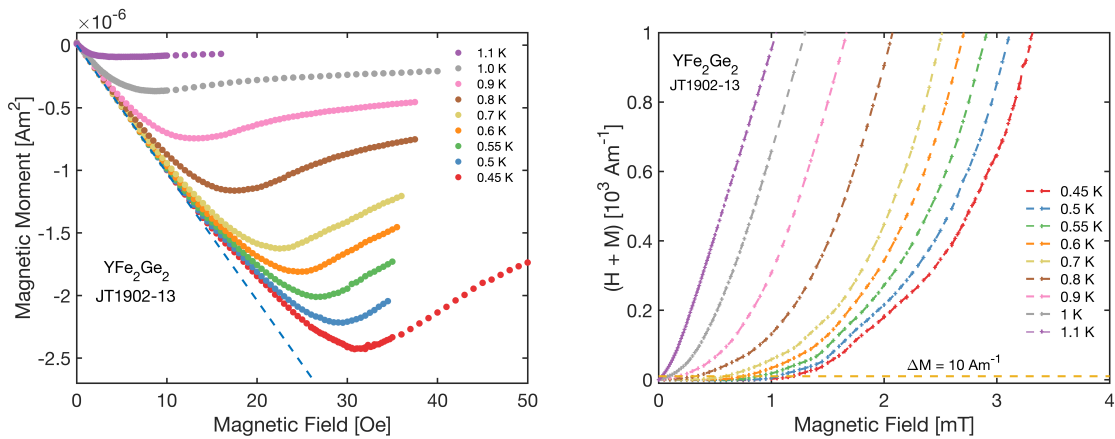
Fig. 5.13 (Left panel) The field dependence of the magnetic moment isotherms at different temperatures. Measurements were taken after zero-field-cooling to the corresponding temperatures. (Right panel) Deviation of magnetisation from the linear low-field *M-H* slope at different temperatures. The fields at which the curves cross $10\,\mathrm{Am}^{-1}$ are taken as estimates for $\mu_0 H_{c1}$ for the respective temperatures.
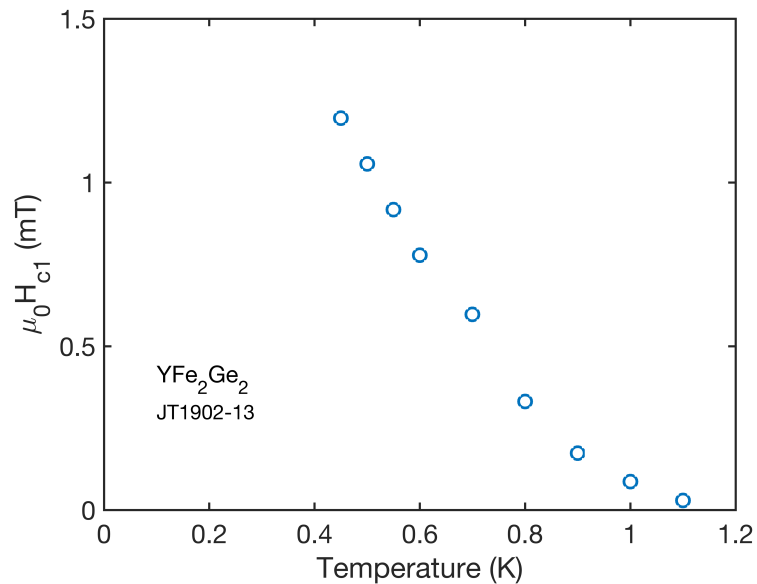
Fig. 5.14 Temperature dependence of the lower critical field $\mu_0 H_{c1}$ of YFe$_2$Ge$_2$ extracted from the right panel in Fig. 5.13.

the upper critical field $B_{c2}(T)$ in YFe$_2$Ge$_2$. These measurements have been carried out with the help of our summer project student Yue Tang. Fig. 5.15 shows the behaviour of the resistive transition with magnetic field applied both parallel and perpendicular to the crystal c-axis. This particular sample (JC1904-PC01-S1) shows one of the highest zero-field resistive transition temperature among all measured samples from batch JC1904 with $T_c \approx 1.8$ K. In contrast with the resistive transition temperatures which vary noticeably between different samples from the growth batch (see e.g. Fig. 5.8), the bulk specific heat transition temperature remains relatively constant across samples. In Fig. 5.16, we see the gradual suppression of the superconducting specific heat anomalies of two different samples by the applied magnetic field.

The applied magnetic field is plotted against the resistive transition temperature (determined by an 80%/20% criterion) for JC1904-PC01-S1 as shown in Fig. 5.17. The inset of the figure is a zoom-in plot of the 50% resistive T_c at low fields, which reveals an upward curvature of the upper critical field $B_{c2}(T)$. Similar behaviours near T_c have been observed for other superconductors and have been taken as evidence for two-gap superconductivity [108]. Here, due to the obvious discrepancy between the resistive and bulk T_c in YFe$_2$Ge$_2$, whose origin is still unclear, and the lack of a similar upward curvature in $B_{c2}(T)$ of the bulk transition, we did not attempt to fit any model to $B_{c2}(T)$ of the resistive transition. We should, however, note the rather isotropic temperature dependence of B_{c2} with magnetic field applied in both orientations for the resistive transition, which is consistent with the fairly isotropic Fermi surface of YFe$_2$Ge$_2$.
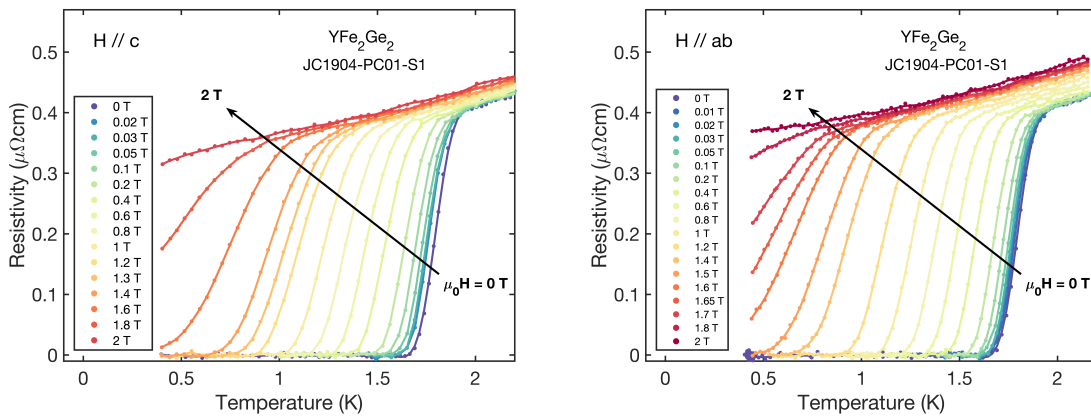

Fig. 5.15 Electrical resistivity of YFe$_2$Ge$_2$ versus temperature under various applied magnetic fields with **H** $\parallel$ c (left panel) and **H** $\parallel$ *ab* (left panel).
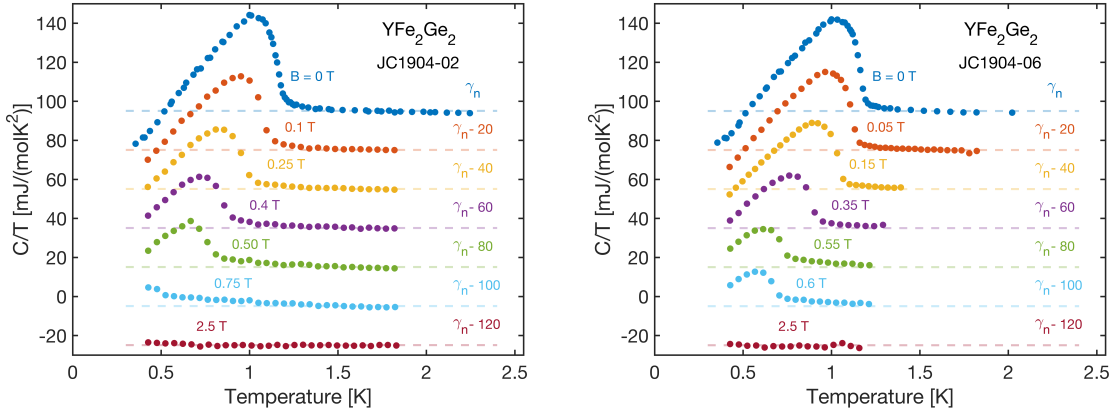
Fig. 5.16 C/T of two YFe$_2$Ge$_2$ samples versus temperature under various applied magnetic fields with **H** $\|$ c, showing the gradual suppression of the superconducting anomaly.

Fig. 5.17 also shows $B_{c2}(T)$ against the onset temperatures of the specific heat superconducting anomalies for three samples (JC1904-02, 06 and 15) with magnetic field applied along the crystal c-axis. The onset temperature is extracted by extending the normal state and the sharpest ascent of C/T and finding the temperature at which they cross. The transition temperatures extracted from the three samples show little deviation from one another. The initial slope of the upper critical field $|dB_{c2}/dT| \approx 1.34\,\mathrm{T\,K^{-1}}$, which corresponds to an extrapolated clean-limit weak-coupling orbital-limited critical field of $B_{c2}^{(0)} \approx 0.73T_c|dB_{c2}/dT| \approx 1.2\,\mathrm{T}$.

The lower critical field, B_{c1} can be related to the characteristic length scales, the London penetration depth λ and the coherence length ξ by [109]

$$B_{c1} = \frac{\Phi_0}{4\pi\lambda^2}(\ln\frac{\lambda}{\xi} + 0.497). \tag{5.1}$$

Since the coherence length ξ can be estimated from the orbital limited upper critical field $B_{c2}^{(o)} = \Phi_0/(2\pi\xi^2)$, we can further obtain an estimate of the London penetration depth λ from B_{c1}. From $B_{c2}^{(o)} \approx 1.2\,\mathrm{T}$, we found $\xi \simeq 167\,\text{Å}$, similar to those obtained from polycrystalline samples in Section 4.2. $B_{c1}(T = 0.45\,\mathrm{K}) \approx 1.12\,\mathrm{mT}$ therefore sets an upper bound for the London penetration depth λ at around 800 nm.
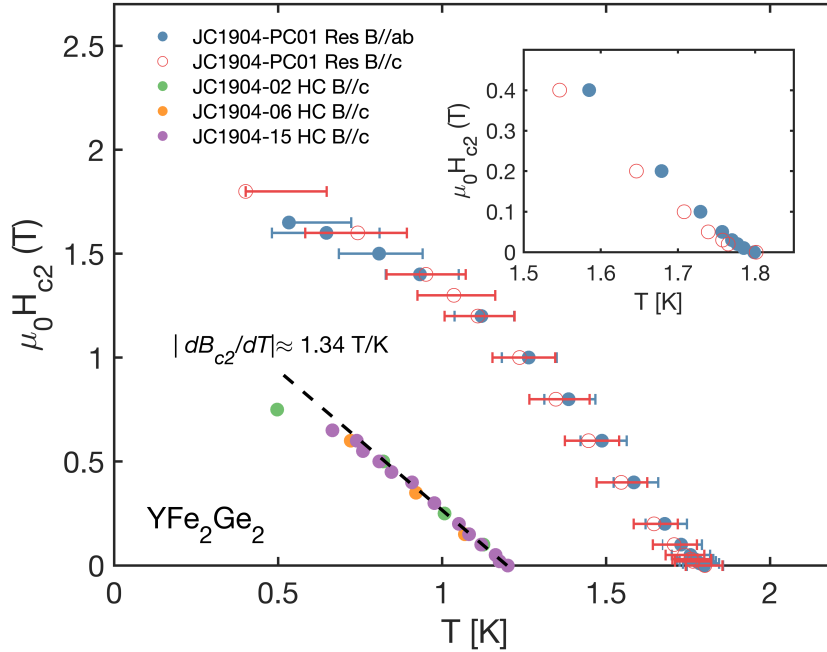
Fig. 5.17 Temperature dependence of H_{c2} of YFe_2Ge_2 samples from batch JC1904 for the resistive transition with $\mathbf{H} \parallel c$ and $\mathbf{H} \parallel ab$ and for specific heat transition with $\mathbf{H} \parallel c$. (inset) Zoomed in plot of the resistive H_{c2} near T_c at 50% transition.

5.1.6   Summary

In this section, I have introduced two flux methods for growing single-crystal YFe_2Ge_2. Both of these methods have produced high-quality crystals which showed signatures of bulk super-conductivity in thermodynamic and magnetisation measurements. Using polycrystals as the charge materials and changing the temperature protocols, samples showing varying degrees of disorder were produced with the modified Sn-flux method. SXRD measurements indicated Fe-Ge antisite defects as the main source of disorder, which suppresses superconductivity in the lower quality samples. On the other hand, by adopting a horizontal configuration and using a two-zone furnace, the liquid transport method has allowed the growth of samples not only with significantly improved quality but also in larger quantities. Both of these growth methods have demonstrated that, at least in Sn-flux growths, the key to producing high-quality YFe_2Ge_2 is the lowering of the precipitation and growth temperature.

One recurring and puzzling feature of YFe_2Ge_2 is the discrepancy between the bulk and resistive T_c. In the early days, this feature led to the doubt of intrinsic superconductivity in this material when bulk transitions were absent. However, even in our best single crystals,

this feature still remains. Currently, we do not have a detailed explanation for the origin of the higher resistive T_c. Evidence from the single crystals suggests that these higher-temperature transitions only occur in small regions of the samples. Given the strong dependence of its superconductivity on disorder, one possibility maybe that the optimum T_c intrinsic to YFe$_2$Ge$_2$ is actually at a higher temperature, e.g. 1.9 K as measured in the polycrystals, and that only part of the sample contains low enough concentration of disorder for this to occur. Alternatively, it could be due to a filamentary strain-stabilising effect, which increases T_c in small regions of the samples. Furthermore, it is possible that the resistive transition is sensitive to properties of the surface of the sample, while the heat capacity transition is more robust as it is a bulk property. Further investigation is needed to elucidate the real cause of the discrepancy between the resistive and bulk T_c.

5.2   Low-temperature specific heat

Specific heat measurement is one of the most widely used experimental probes for investigating superconducting properties of materials. In Section 5.1, we have seen specific heat data for a range of single-crystal YFe$_2$Ge$_2$ samples at temperatures above 0.4 K. To further study the superconducting gap structure in this material requires measurements into much lower temperatures.

Thanks to our collaborators Jacintha Banda and Dr. Manuel Brando at the Max Planck Institute in Dresden, Germany, the low-temperature specific heat of two single-crystal samples (SR1726-02 and JT1902-11) have been measured down to 100 mK in a dilution refrigerator. (In fact, specific heat data were originally measured down to 30 mK. However, below 100 mK, there appeared to be an anomalous field-dependent upturn in the measured C/T, which can not be simply explained by nuclear Schottky anomalies and may be due to systematic errors in the measurement. We therefore only focus on the more reliable data above 100 mK. Plots of the original data can be found in Appendix B.) The specific heat measurements were performed using a compensated heat pulse method [110] on a customised silver platform with a RuO$_2$ thermometer.

Fig. 5.18 and Fig. 5.19 show the the measured C/T of the two samples at various magnetic fields. At this temperature range, the contribution of the phonon specific heat is negligible. For both samples, we observe that the low-temperature $C(B = 0)/T$ appears to extrapolate to a non-zero value at zero temperature. This is not normally expected for a superconductor with a 100% superconducting volume fraction. Under zero applied field, both samples show a nearly linear C/T at low temperatures. Extrapolating the linear behaviour below 100 mK, we obtain a residual Sommerfeld coefficient γ_{res} of around 69 mJ/molK^2 for sample SR1726-02
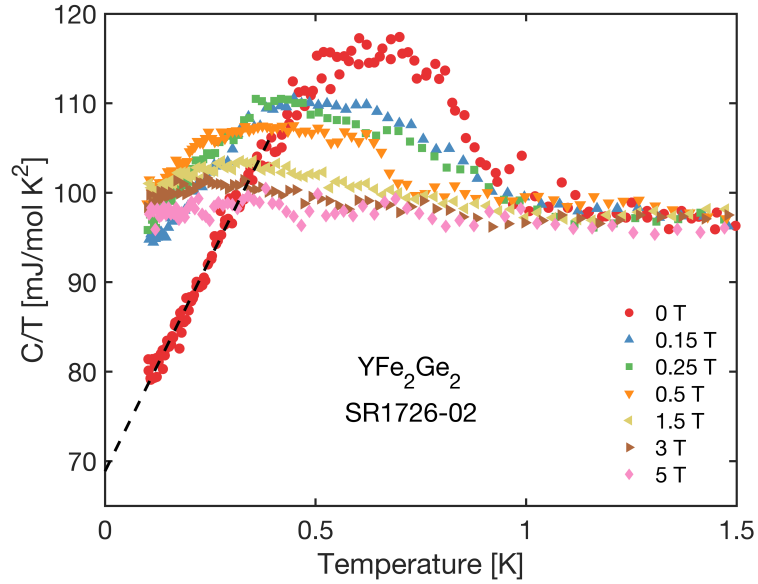
Fig. 5.18 C/T of YFe$_2$Ge$_2$ single crystal sample SR1726-02 versus temperture at zero field and at various applied magnetic fields. Black dash line shows a linear extrapolation of the zero-field low-temperature C/T to zero temperature.
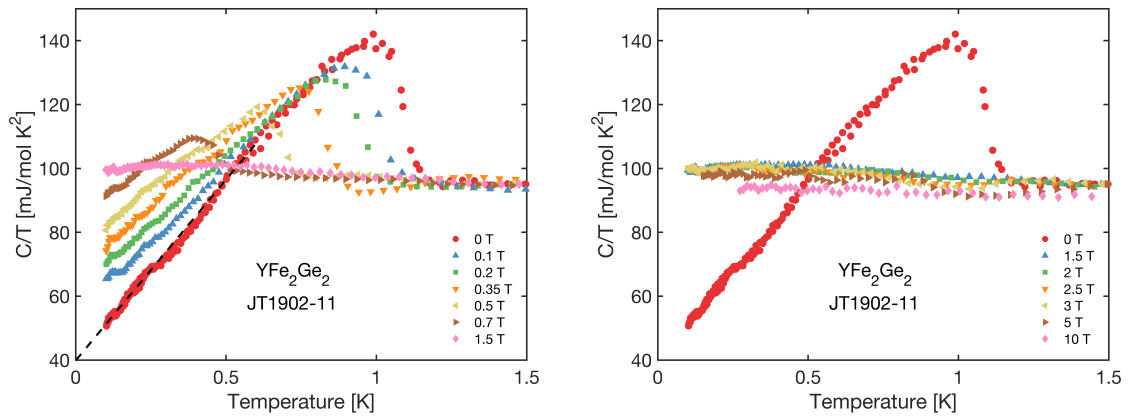

Fig. 5.19 C/T of YFe$_2$Ge$_2$ single crystal sample JT1902-11 versus temperature at zero field and at various applied magnetic fields. Black dash line (left panel) shows a linear extrapolation of the zero-field low-temperature C/T to zero temperature.

and around $42\,\text{mJ/molK}^2$ for sample JT1902-11. Both of these values account for significant fractions of the normal-state Sommerfeld coefficient, $\gamma_{\text{norm}} \approx 100\,\text{mJ/molK}^2$.

As we have seen so-far both in Section 5.1 and in Fig. 5.19, despite the sharp superconducting anomaly observed in the specific heat of samples from batch JT1902, the height of the specific heat jump, $\Delta C(T_c)$ is only around 40% that of the normal state value at T_c, C_{norm}. This is significantly smaller than $\Delta C(T_c) = 1.43 C_{\text{norm}}$ expected for a conventional s-wave superconductor in the weak-coupling regime. The jump height is even less pronounced for sample SR1726-02, although in this case, the superconducting anomaly is also much broader.

At first glance, especially at the specific heat data of SR1726-02, one may turn to a simple explanation that there exists a significant non-superconducting volume fraction in the sample. However, evidence from other measurements argues against such an explanation. First of all, we can rule out the possibility that the superconducting anomaly is attributed to an alien phase: powder X-ray diffraction has excluded the presence of secondary phases in these crystals, besides the occasional Sn inclusions. From the normal-state C/T, we can easily exclude the possibility of more than 5% Sn inclusion. Therefore, any non-superconducting volume fraction would have to be intrinsic to YFe$_2$Ge$_2$. Secondly, even for samples from batch SR1726, which show relatively broad specific heat transitions, magnetisation measurements showed a complete Meissner screening of magnetic field at low temperatures, suggesting a full superconducting volume fraction (Fig. 5.4). To allow the full diamagnetic screening while containing a significant non-superconducting volume, the normal-state volume must be enclosed inside the sample. However, in the liquid transport growth method, the temperature
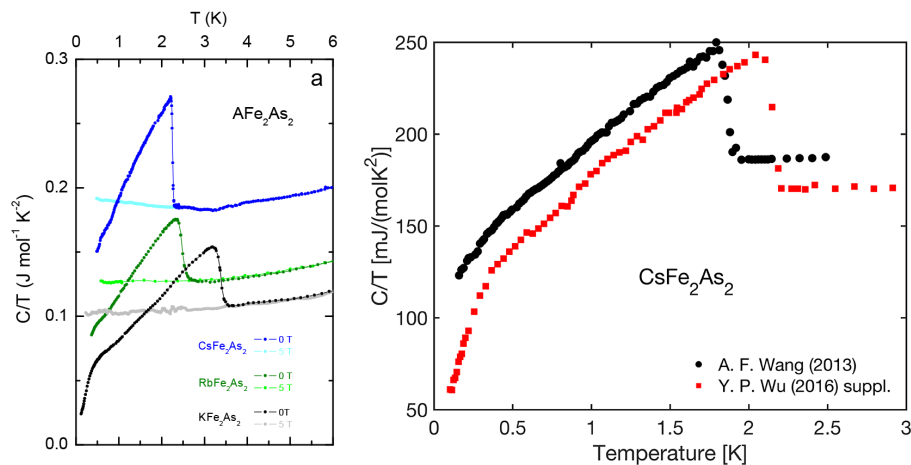

Fig. 5.20 C/T of alkali-metal iron arsenides K/Rb/CsFe$_2$As$_2$ versus temperature. (Figure and data from [111, 112].)
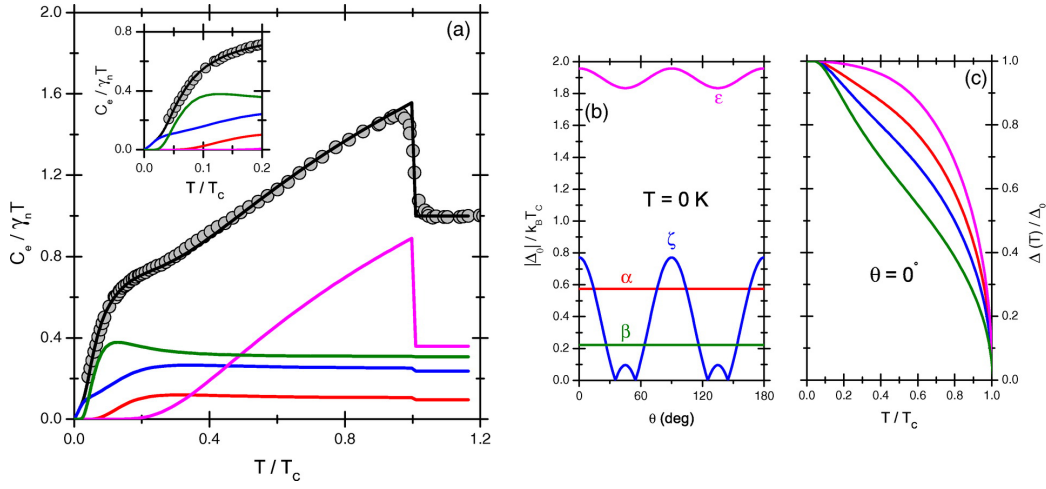
Fig. 5.21 (a) Temperature dependence of normalised heat capacity of KFe_2As_2 and the fitting to a 4-band BCS model (black lines) described in [20]. The colored curves represent contributions from the individual bands. The inset shows data below $0.2T_c$. (b) Angular dependence of the individual gaps at $T = 0$ K. (c) Temperature dependence of the individual gaps for $\theta = 0$. (Figures credit: [20])

and concentration conditions are maintained throughout the growth, except when cooling down to room temperature at the end of the growth. Therefore, any significant difference in lattice composition is likely to occur at the surface rather than inside the crystals. Given the sharp transitions shown in specific heat and magnetisation measurements, it is unlikely that samples grown with the liquid transport method contain a large non-superconducting fraction.

In fact, the combination of a low $\Delta C(T_c)/C_{norm}$ and a large apparent residual C/T down to low temperatures is a common feature of the alkali-metal iron arsenides, K/Rb/CsFe$_2$As$_2$ [20, 111, 112]. Fig. 5.20 shows C/T data of these hole-doped 122 iron-based superconductors. For all three materials, the normal-state Sommerfeld coefficient γ_{norm} is similarly enhanced as observed in YFe$_2$Ge$_2$ [111] and $\Delta C(T_c)/(\gamma_{norm}T_c)$ shows a similar value between 0.4 and 0.5. Among these compounds, KFe$_2$As$_2$ has been studied in the greatest detail. Its specific heat has been measured to below 100 mK, revealing a kink in C/T at around 300 mK, below which it sharply reduces towards zero [20]. The interpretation for such a feature is the presence of multiple superconducting gaps on different Fermi surface sheets. Fig 5.21 shows the fitting of the specific heat data of KFe$_2$As$_2$ to a four-gap model described in [20], in which it shows how each gap influences the temperature dependence of $C_e(T)$ separately. In particular, the presence of a 'Lilliputian' gap on the β Fermi surface sheet (i.e. the largest
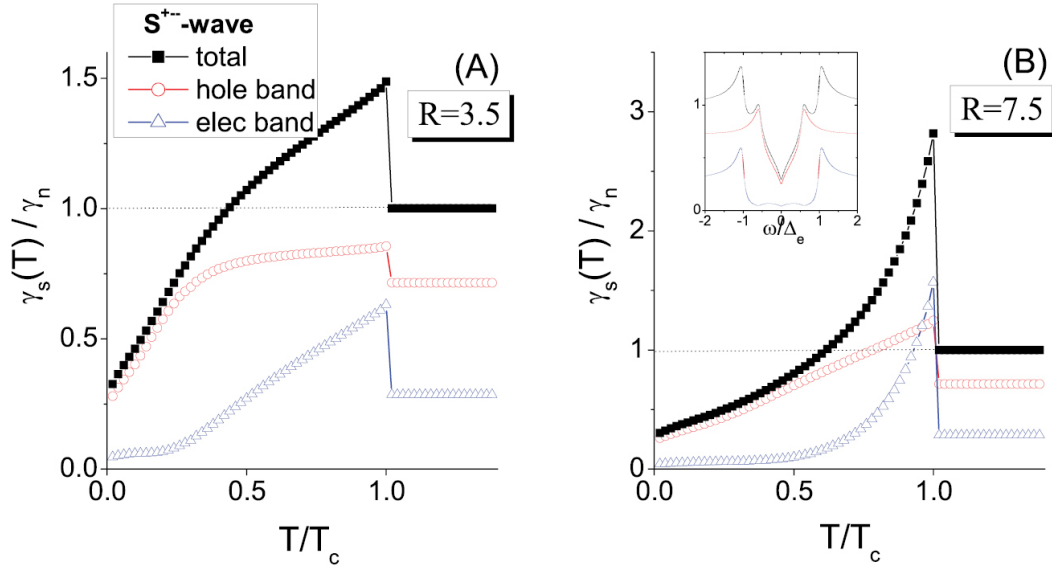
Fig. 5.22 Simulated normalised specific heat of an s$^\pm$-wave superconductor with impurity scattering. The red circles and blue triangles indicate the hole and electron band contributions respectively. Common parameters used for the simulation of (A) and (B) are: (1) the electron to hole gap ratio at zero temperature $|\Delta_e/\Delta_h| = 2.5$, (2) the density of state ratio $N_h/N_e = 2.5$, and (3) the scattering rate $\Gamma_{imp} = 0.1\Delta_e$. For (A) $R = 2\Delta_e/T_c = 3.5$, and for (B) $R = 7.5$. (Figure credit: [55])

hole sheet around the Γ point of the Brillouin zone - see Fig. 1.3) contributes significantly to C_e, causing its high value to low temperatures before the downturn at around 300 mK. In the right panel of Fig. 5.20, we observe the onset of a similar downturn in C/T of CsFe$_2$As$_2$. This downturn appears to shift to a lower temperature in a sample with a lower transition temperature T_c.

YFe$_2$Ge$_2$ also hosts multiple Fermi surfaces. The similarities in the specific heat properties between YFe$_2$Ge$_2$ and the alkali-metal iron arsenides raise the possibility of a similar pairing mechanism. In YFe$_2$Ge$_2$, because of the lower bulk-transition temperature at $T_c \approx 1.1$ K, a similar downturn in C/T, if it exists, would occur at temperatures below 100 mK. Therefore, accurate measurements to lower temperatures are necessary for testing this idea.

A theoretical study by A. Subedi [35] has pointed out the possibility of an s$^\pm$ superconducting pairing state in YFe$_2$Ge$_2$ as a result of the nesting between the hole sheet around the Z point and the electron cylinder around the X point (see Fig. 1.3). An alternative explanation for the residual γ may come from the consideration of impurity and disorder scattering. In a review article by Y. Bang and G. R. Stewart [55], the influence of impurity scattering on the

superconducting properties of s$^{\pm}$-wave superconductors has been investigated theoretically for a two-gap model. It was pointed out that non-magnetic impurities can cause the development of impurity bound states inside the energy gap (e.g. Fig. 2.4). Beyond a critical level of impurity scattering, the zero-energy density of state becomes non-zero due to the presence of these bound states, which can lead to quasi-particle excitations even at very low temperatures. Similar conclusions have been made by other theoretical studies [113, 114]. Furthermore, C/T can display a linear T dependence at low temperatures in an $s^{\pm}$-wave superconductor beyond a critical impurity scattering level [55]. Fig. 5.22 shows the calculated normalised specific heat for different gap parameters of modelled systems with significant impurity scattering. The figure on the left panel is qualitatively very similar to the specific heat of YFe$_2$Ge$_2$ at low temperatures. This suggests the possibility of s$^{\pm}$-wave pairing in YFe$_2$Ge$_2$, which is affected by disorder.

5.3 Low-temperature μSR study

The temperature dependence of the superconducting gap function dictates the low-temperature behaviour of experimental properties in superconductors. It determines the amount of thermal excitations which may break the Cooper pairs. In this section we investigate one of these
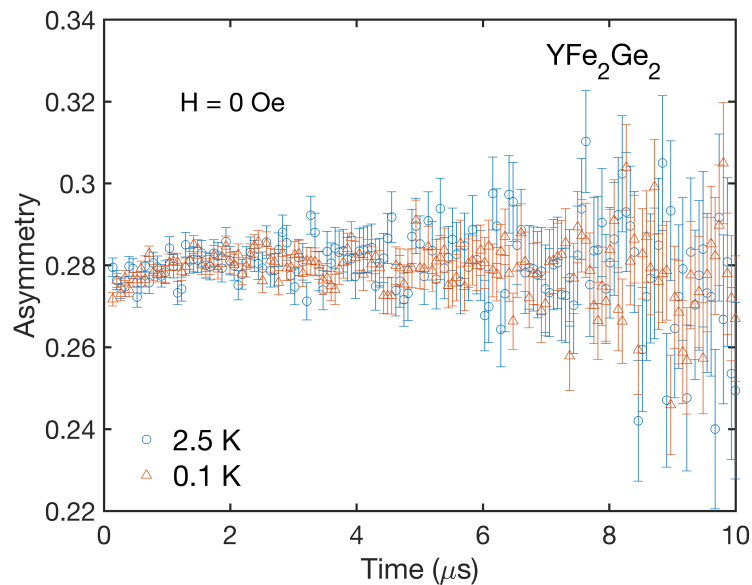

Fig. 5.23 Muon spin relaxation asymmetry signals collected in zero field, above and below the superconducting transition temperature of YFe$_2$Ge$_2$.

properties, namely the London penetration depth, in the superconducting state of YFe$_2$Ge$_2$ using the technique of muon spin rotation. From the penetration depth data, we will try and infer information regarding the superconducting gap structure.

The μSR experiment was carried out on the MuSR spectrometer in the ISIS pulsed muon facility in collaborations with Dr. Devashibhai T. Adroja and our local contact Dr. Pabitra K. Biswas. Details of this technique are described in Sections 2.4 and 3.3. Single-crystal YFe$_2$Ge$_2$ samples used in this experiment have been selected from the batch JT1902, which show bulk $T_c \simeq 1.1$ K. These samples were aligned by eye under an optical microscope and glued down onto a silver holder using a small amount of GE varnish. The alignments of the crystals were further checked, adjusted and confirmed using a Laue X-ray camera. The crystallographic ab-plane of the samples was aligned parallel to the surface plane of the silver holder while the c-axis was in the perpendicular direction. As a result, in the transverse-field μSR (TF-μSR) measurements, the magnetic field was applied in the a-direction of the crystals. Fig. 3.11 shows the samples used in the experiment, glued on the silver holder. A thin sheet of silver film was further glued onto the sample holder to prevent accidental detachment of samples. The holder was then secured at the end of the measurement probe which monitors the temperature and inserted into an Oxford Instrument dilution refrigerator (King Triton).

Zero-field μSR (ZF-μSR) was first performed both above (2.5 K) and below (100 mK) the superconducting transition T_c of YFe$_2$Ge$_2$ to detect the presence of any weak internal magnetism. Fig. 5.23 shows the ZF-μSR signals measured at the two temperatures respectively. Data taken above and below T_c both show very little relaxation of the asymmetry, indicating the absence of an internal field. This is consistent with the fact that YFe$_2$Ge$_2$ is a paramagnetic metal. The lack of noticeable changes in the asymmetry signal as the samples are cooled below T_c also indicates the absence of any spontaneous internal field at the muon sites and hence suggests that time-reversal symmetry is preserved.

The TF-μSR experiment was conducted with an applied field of 200 Oe which was first applied well above T_c (i.e. field-cooled), allowing the investigation of the sample in the vortex state. TF-μSR precession signals above and below T_c are shown in Fig. 5.24. In the normal state the signal decays very slowly, while the decay is significantly faster in the superconducting state due to the inhomogeneous field distribution from the flux-line lattice. The behaviour of the asymmetry time spectrum can be modelled using an oscillatory decaying Gaussian function:

$$A_{TF}(T) = A_0 \exp(-\sigma^2 t^2/2) cos(\gamma_\mu B_{sc} t + \phi) + A_{bg} cos(\gamma_\mu B_{bg} t + \phi). \qquad (5.2)$$
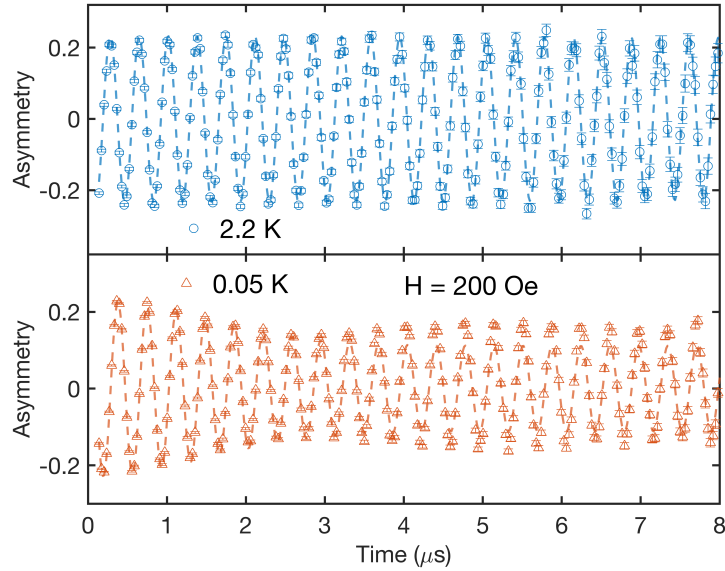
Fig. 5.24 Representative TF-μSR signals collected above (upper panel) and below (lower panel) T_c in YFe$_2$Ge$_2$ under an applied magnetic field of 200 Oe. The dash lines are fits to the signals using Eq. 5.2.
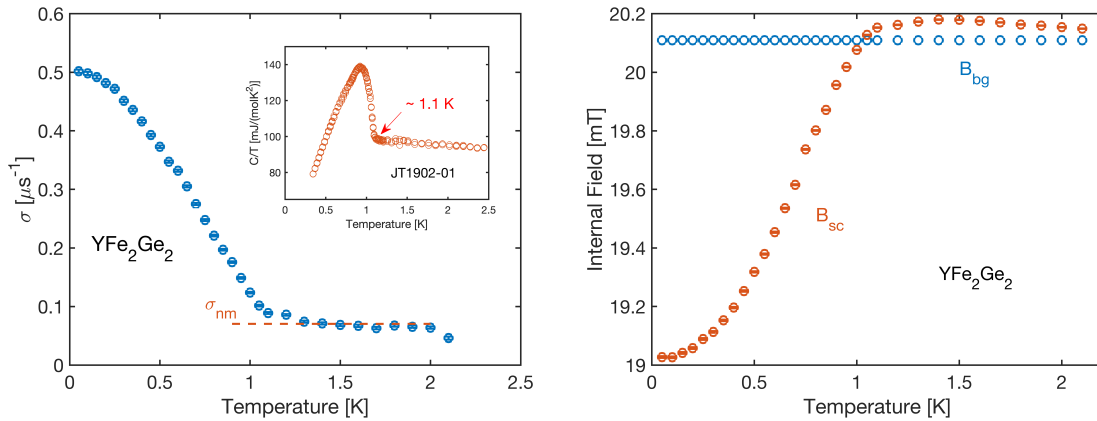
Fig. 5.25 (Left panel) Temperature dependence of the Gaussian depolarisation rate σ extracted from the transverse-field μSR asymmetry signals collected in an applied magnetic field $H = 200$ Oe. (Inset in left panel) C/T of YFe$_2$Ge$_2$ showing the onset of bulk transition temperature. (Right panel) Temperature dependence of the associated field parameters B_{sc} and B_{bg}. B_{bg} has been fitted to data at 50 mK and taken to be temperature-independent.

The two terms on the right-hand-side of the above equation represent contributions from muons implanted in the YFe$_2$Ge$_2$ samples and from those on the silver holder respectively. A_0 and A_{bg} are the amplitudes of the oscillations, $\gamma_\mu/2\pi$ is the muon gyromagnetic ratio, B_{sc} and B_{bg} represent the average internal fields in the sample and the silver holder respectively, ϕ is the initial phase offset, and σ is the Gaussian muon spin relaxation rate.

The asymmetry signal at 50 mK was used as the reference (starting point) for a sequential least-square fitting of Equ. 5.2 using the software Mantidplot. After all parameters were fitted for the data at 50 mK, the oscillation amplitudes, A_0 and A_{bg}, the phase factor, ϕ, and the internal field at the silver holder, B_{bg}, were fixed for the fittings of data at the other temperatures. The fitted values for the rest of the parameters at each temperature were then used as starting values for the subsequent fitting at a higher temperature.

Fig. 5.25 shows how the fitted values of σ and B_{sc} vary as a function of temperature. B_{bg}, whose value is taken from the fitting for data at 50 mK, has been assumed to be temperature-independent. As expected, $\sigma(T)$ increases noticeably as temperature drops below T_c. The small and nearly constant relaxation rate σ_{nm} between 1.3 and 2 K arises mainly from the temperature-independent background field distribution due to the nuclear dipole moments. An additional kink in σ above 2 K is caused by the presence of a small amount of tin inclusions inside the YFe$_2$Ge$_2$ samples. The superconducting transition temperature of tin under a 200 Oe applied field is around 2 K [115].

The superconducting Gaussian muon-spin depolarisation rate σ_{sc} caused by the flux-line lattice can be further extracted as $\sigma_{sc}(T) = \sqrt{\sigma^2(T) - \sigma_{nm}^2}$. The temperature dependence of the London magnetic penetration depth, $\lambda(T)$, is related to the $\sigma_{sc}(T)$ by the Equ. 2.35: $\lambda = 327.5/\sqrt{\sigma_{sc}}$. In order to infer information on the superconducting gap structure, $\lambda(T)$ was fitted using either a single- or a two-gap model on the basis of the α-model [51, 53] which is described in Section 2.2. Fits to the data using four different gap models are shown in Fig. 5.26, with the best fitted parameters summarised in Table 5.4. The poor fit of the s-wave model to the data at low temperature provides strong evidence that the superconducting gap function differs significantly from the conventional single-band s-wave type in the BCS theory. The data also deviates noticeably at the lowest temperatures from the fitting to the single-gap d-wave model. On the other hand, the two-gap models provide much better fitting to the low-temperature penetration depth data, suggesting a multi-gap nature of the superconductivity in YFe$_2$Ge$_2$. From this analysis, phase information between two gaps cannot be inferred.

Due to the constraint imposed by the shape of the crystals, it was much easier to mount samples with c-axis perpendicular to the silver holder than the alternatives, which meant that London penetration depth in the ac plane was probed (a- and b-axes are equivalent). Given
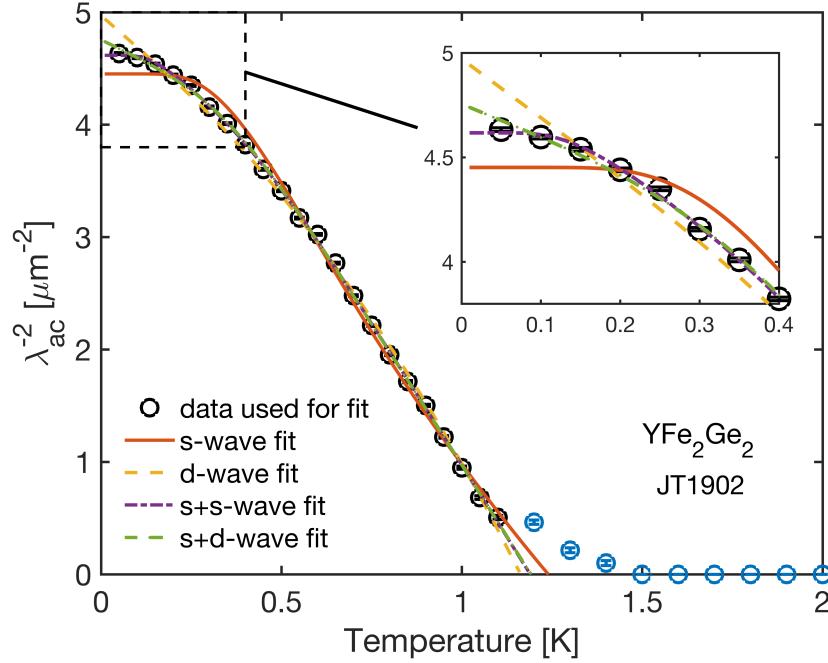
Fig. 5.26 Temperature dependence of λ_{ac}^{-2} for magnetic field applied along the a-axis of YFe$_2$Ge$_2$. The four curves are fits to $\lambda_{ac}^{-2}(T)$ using different single- and two-gap models. (inset) Zoom in of the low-temperature region, showing a poor fitting of the single-gap s-wave model to the data.

Table 5.4 Fitted parameters to the $\lambda_{ac}^{-2}(T)$ data of YFe$_2$Ge$_2$ using four different models for the superconducting gap function. The respective meaning of the parameters: Δ: zero-temperature value of superconducting gap, T_c: transition temperature; $\lambda(0)$: zero-temperature value of magnetic penetration depth; and ω is the relative weight of the larger gap.

Model	Gap value (meV)	ω	$\lambda(0)$ (nm)	T_c
s-wave	$\Delta = 0.134$		445	1.24
d-wave	$\Delta = 0.212$		497	1.16
$s+s$-wave	$\Delta_1 = 0.158, \Delta_2 = 0.057$	0.795	462	1.19
$s+d$-wave	$\Delta_1 = 0.160, \Delta_2 = 0.010$	0.72	476	1.19

that $\lambda_{ac}^{-2}(T)$ consists of both an in-plane and an out-of-plane component of the magentic penetration depth [116], this calls for caution on any conclusions based solely on λ_{ac}, as large anisotropy may exist between these two components. Further experiments will be needed to investigate the temperature dependence of λ_{ab} (with $\mathbf{H} \parallel c$) to disentangle these two components.

5.4 Quantum Oscillations

One of the many interesting and puzzling properties of YFe$_2$Ge$_2$ is its sizeable normal-state Sommerfeld coefficient $C/T \simeq 100\,\mathrm{mJ/molK^2}$ at low temperatures. To investigate the origin of the strong electronic correlations which cause the enhancement of the specific heat, we set out to probe its Fermi-surface structures through quantum oscillation (QO) measurements.

As discussed in Section 2.5, high-purity crystals are essential for the observation of quantum oscillations. Multiple previous attempts at detecting QO in both poly- and single-crystal YFe$_2$Ge$_2$ with RRR up to 200 have failed - the Dingle factor dominates and suppresses the oscillation amplitude. Fortunately, the new generation of single crystals obtained from
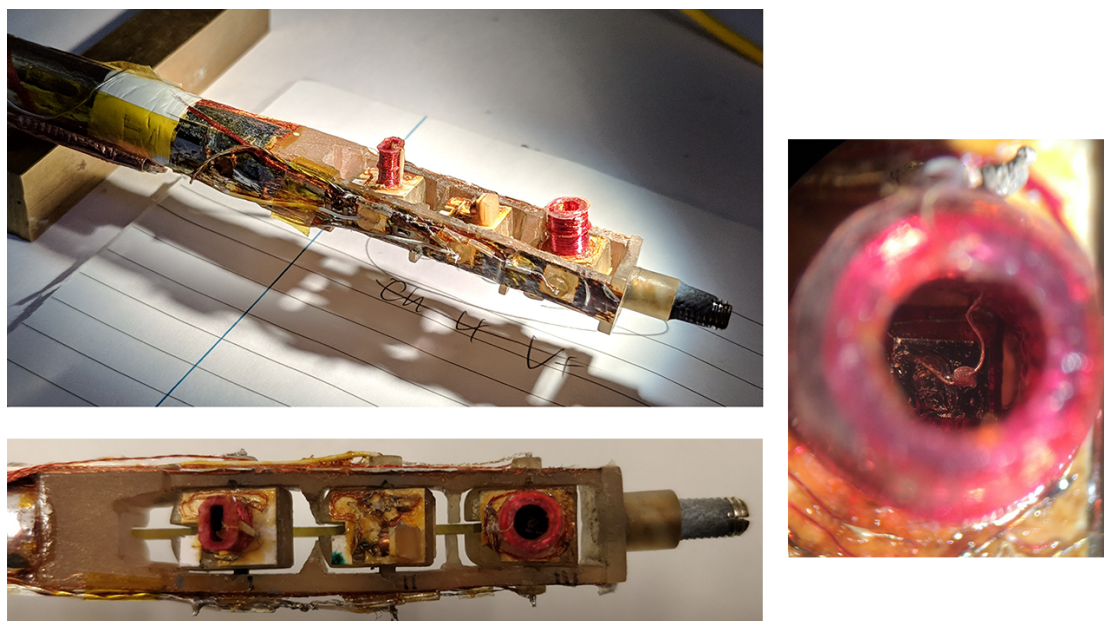

Fig. 5.27 Pictures showing the side (top left panel) and top (bottom left panel) views of the plastic rotation mechanism for the dilution refrigerator, which contains three rotatable bobbins, and (right panel) the top view of the coil sets which contain the YFe$_2$Ge$_2$ single crystal sample used in the dHvA measurements.
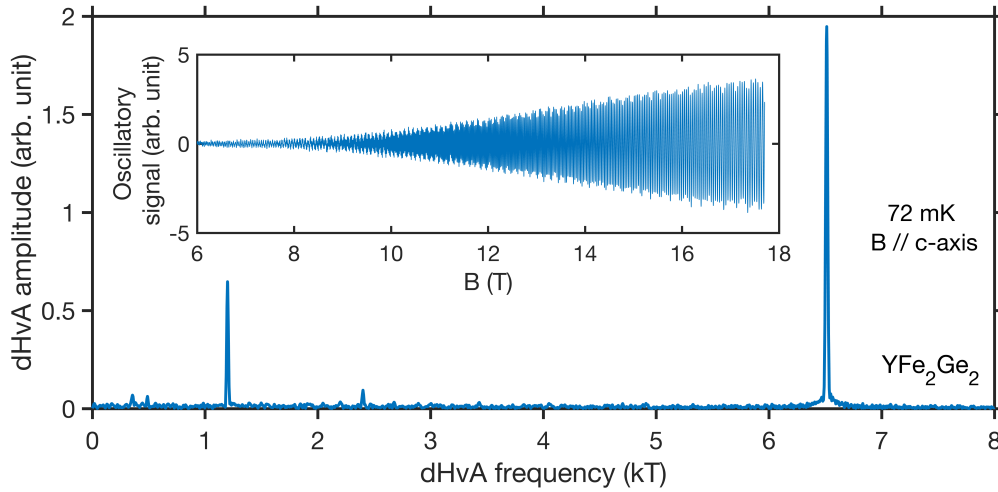
Fig. 5.28 The typical background-subtracted de Haas-van Alphen signal in YFe_2Ge_2 and its Fourier spectrum in $1/B$. The oscillatory signal is clear even at magnetic field as low as $6\,T$, demonstrating the high quality of the crystal.

the liquid transport method described in Section 5.1.3 showed even higher RRR between 300 and 470. The significantly improved quasi-particle mean free paths in these crystals have finally enabled the detection of quantum oscillations.

Quantum oscillation measurements on YFe_2Ge_2 were carried out in the dilution refrigerator in the Quantum Matter group. It is equipped with a superconducting magnet capable of producing a $20.4\,T$ magnetic field. So far, the experiments have been performed with the lambda point refrigerator off, limiting the maximum field to below $18.4\,T$. Preliminary measurement of de Haas-van Alphen (dHvA) effect in ac susceptibility and the tunnel-diode oscillation (TDO) measurement at fixed angles with magnetic field $\mathbf{B} \parallel c$ (dHvA) and $\mathbf{B} \parallel a$ (TDO) were performed on samples from growth batch JT1902 for initial testing. The results of these early measurements have been summarised in Appendix A. More recently, further dHvA measurements have been performed on a rotation mechanism, which allowed the angle dependence of the oscillation frequencies to be investigated. Besides winding of the dHvA coils, all credit for setting up and performing the dHvA and TDO experiments go to Dr. Jordan Baglo and fellow PhD student Keiron Murphy.

The rotation mechanism of the dilution refrigerator measurement probe is shown in Fig. 5.27. On the third bobbin of the rotation mechanism, a pair of cylindrical dHvA pickup coils (each with around 1500 turns, and resistance of $\approx 400\,\Omega$ at room temperature) was mounted. The two coils are connected with opposite polarity, and care was taken to adjust
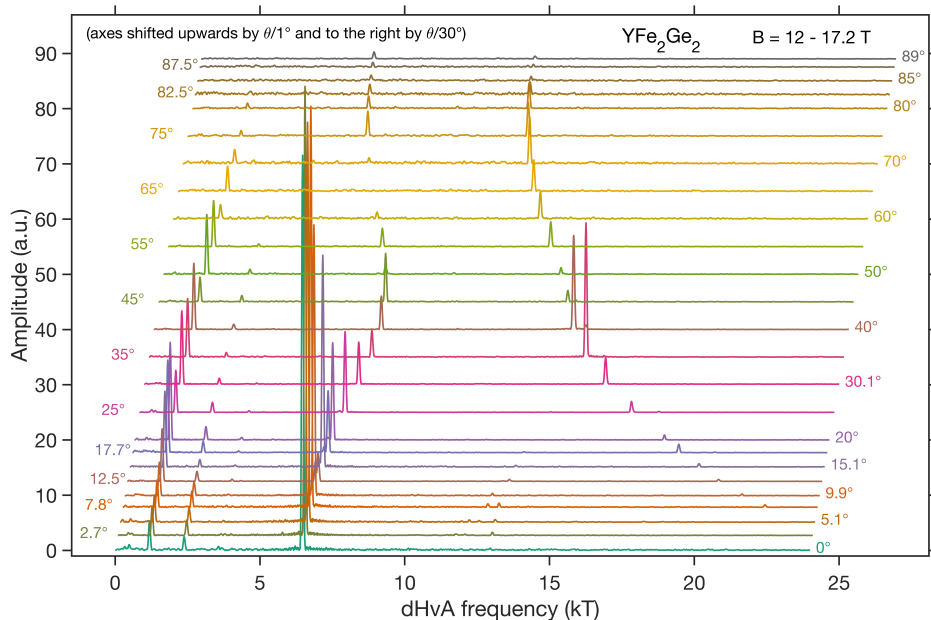
Fig. 5.29 The FFT spectra in $1/B$ between 12 and 17.2 T of the background-subtracted dHvA signals at base temperature obtained for different rotation angle θ. The axis of each spectrum has been shifted upwards by $(\theta/1°)$ and to the right by $(\theta/30°)$kT for clarity. θ is the angle between the magnetic field direction and the c-axis within the crystal ac-plane.
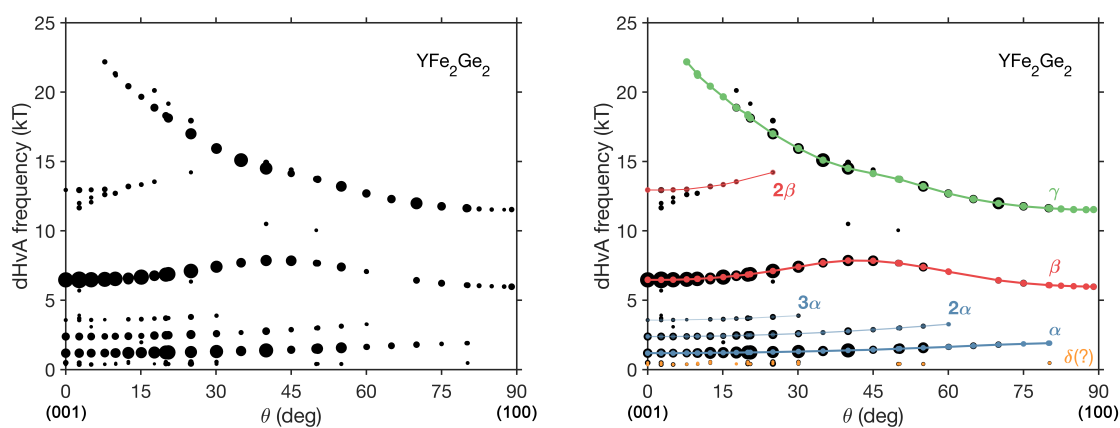
Fig. 5.30 The extracted peak positions from the FFT spectra at different angles and (right panel) the groupings of the peaks according to the DFT calculations.

the windings of the two coils so that they are well compensated when no sample was present. Inside the lower coil, a single-crystal YFe_2Ge_2 sample (JC1904-08, 31.3 mg) was placed with its crystal c-axis parallel to the axes of the pickup coils. The a- and b-axes of the crystal are aligned to the rectangular edges of the bobbin, so that as it rotates, the applied magnetic field points within the ac-plane of the crystal lattice during the measurement. To provide good thermal conduction between the sample and the dilution refrigerator, a $50 \mu m$ silver wire was spot welded to the sample (see right panel in Fig. 5.27) and the contact was further reinforced by a droplet of silver epoxy H20E cured at $80 \degree C$. The other end of the silver wire was subsequently soldered onto another thicker silver wire which was heat sunk to the mixing chamber of the dilution refrigerator. To measure the susceptibility signals, a modulation field with amplitude around 3.6 G and frequency of 28.64 Hz was used. The signal from the coil set was fed to a room-temperature transformer and a preamplifier for a $\times 500$ gain and measured by an SR830 lock-in amplifier.

Fig. 5.28 shows the typical background-subtracted dHvA signal and its fast-Fourier-transform (FFT) spectrum in $1/B$. The signal was collected with magnetic field applied along the crystal c-axis direction. The background subtraction was performed by fitting a low-order polynomial to the measured voltage data as a function of magnetic field. The polynomial fit was chosen as to not interfere with the low-frequency oscillations. As seen in the figure, clear quantum oscillations were detected even down to 6 T, indicating very high sample purity.
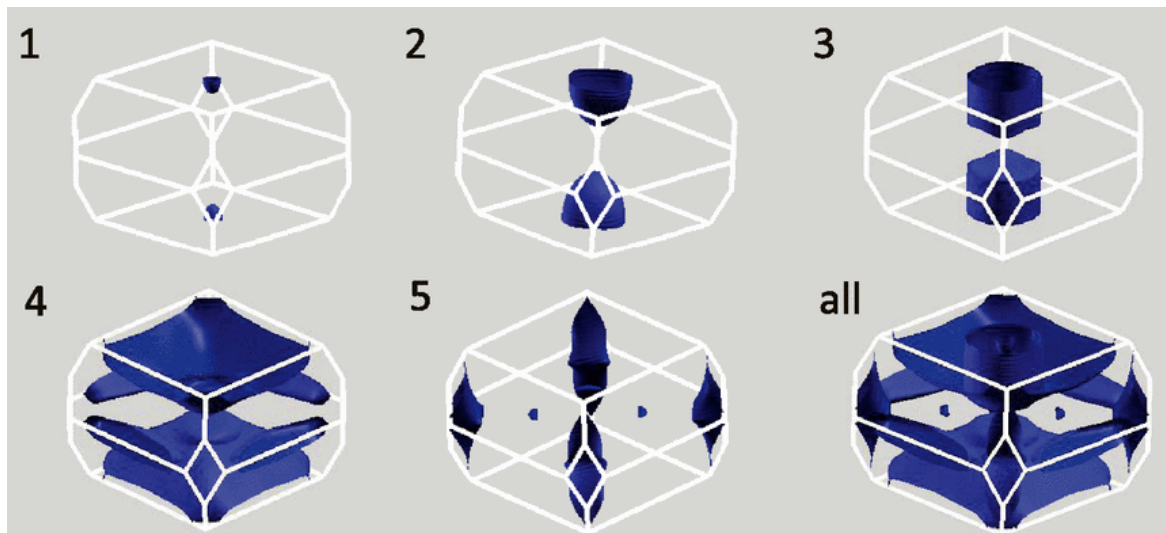
Fig. 5.31 The five Fermi surfaces of YFe_2Ge_2 obtained from DFT calculations by D. J. Singh [36].
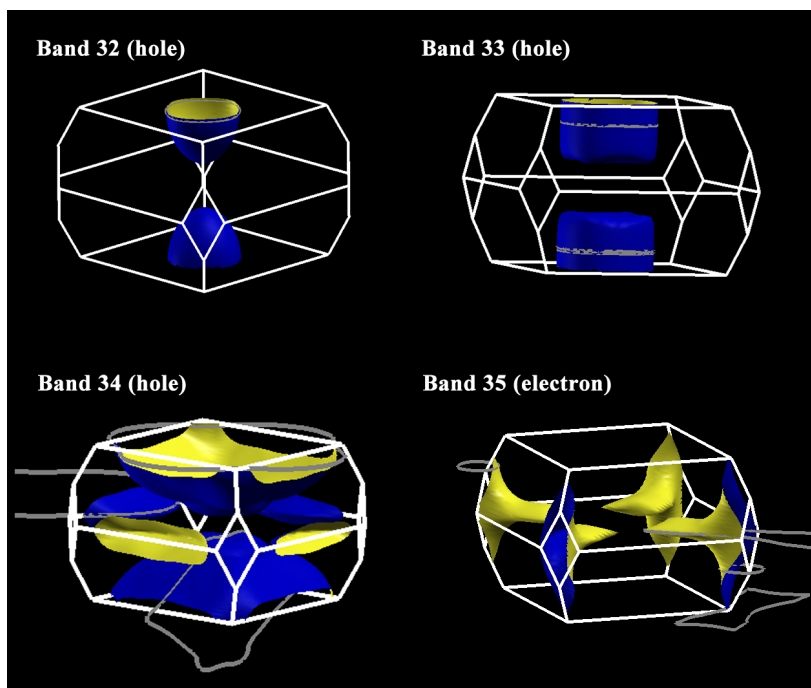
Fig. 5.32 The four Fermi surfaces of YFe$_2$Ge$_2$ obtained from an updated DFT calculation using the experimentally measured z-parameter of Ge.
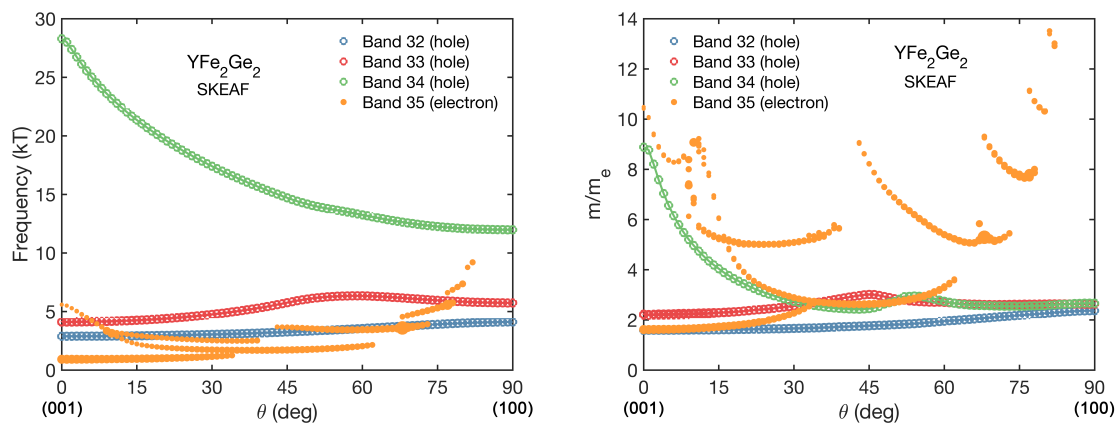
Fig. 5.33 The dHvA frequency (left panel) and quasi-particle mass (right panel) for the four Fermi surface sheets of YFe$_2$Ge$_2$ versus θ, estimated using the SKEAF program based on the DFT calculations using experimentally obtained z-parameter.

To obtain information regarding the Fermi surface topology, the angle dependence of the dHvA oscillations was probed between $\theta = 0°$ and $\theta = 89°$ in field sweeps between $17.2\,\mathrm{T}$ and $12\,\mathrm{T}$, where θ is the angle between the magnetic field direction and the crystallographic c-axis in the ac-plane. Corrections to the magnetic field values have been applied according to the pre-determined field profile of the magnet and the distance of the coil from the field center at each angle. The FFT spectra of the background-subtracted dHvA signals in $1/B$ at the base temperature at various angles of rotation have been plotted in Fig. 5.29. For visual clarification, the spectra have been shifted with respect to one another according to the angle θ. Frequency peaks in the FFT spectrum at each orientation were identified when they exceeded the (frequency dependent) background noise level by at least a factor of two. The left panel in Fig. 5.30 shows the identified frequency peaks for all angles. The size of each black circle indicates qualitatively the significance of the frequency peak in the corresponding FFT spectrum.

According to DFT calculations from [23] and [36], we expect there to be five Fermi surfaces (FS) in YFe$_2$Ge$_2$ (see Figs. 5.31 and 1.3). Centred at the Z point are two small hole pockets ('1' and '2'), a truncated hole cylinder ('3') and a large hole disk ('4') which extends to the edges of the zone. At the zone corners around the X point, we see an extended electron cylinder. Recently, an updated DFT calculation was performed by Prof. Malte Grosche using the input z-parameter for the Ge atoms ($z = 0.3783$) obtained from the refinement of single-crystal X-ray diffraction data on a sample with RRR $\approx$ 170. In this updated calculation, only four Fermi surfaces are obtained, with one of the small hole pocket (sheet "1") absent. These Fermi surfaces are shown in Fig. 5.32. They are qualitatively similar to results from previous calculations except for the missing hole pocket. From the updated Fermi surfaces, quantum oscillation frequencies for the extremal orbits and band masses were further calculated using the Supercell K-space Extremal Area Finder (SKEAF) program [117]. Fig. 5.33 shows the expected quantum oscillation frequencies and band-masses (in electron masses, m_e) of each of the four Fermi surfaces against the angle θ. Due to the extrusion of the electron pocket towards the Γ point, many additional extremal orbits are present for this pocket.

By comparing the angular dependence of the experimentally obtained oscillation frequencies shown in the left panel of Fig. 5.30 and those estimated based on DFT calculations shown in the left panel of Fig. 5.33, we can assign the different measured frequencies to the corresponding Fermi surfaces. In particular, as shown in the right panel of Fig. 5.30, the β and γ peaks can be matched to the hole-like Band 33 and Band 34 respectively, due to their closely resembling angular dependence and magnitudes to the calculations. We see that the frequencies of the γ peaks are fast decreasing towards $\theta = 90°$, whereas those of the β peaks show a hump at around $40°$. Moreover, although the measured frequencies are only
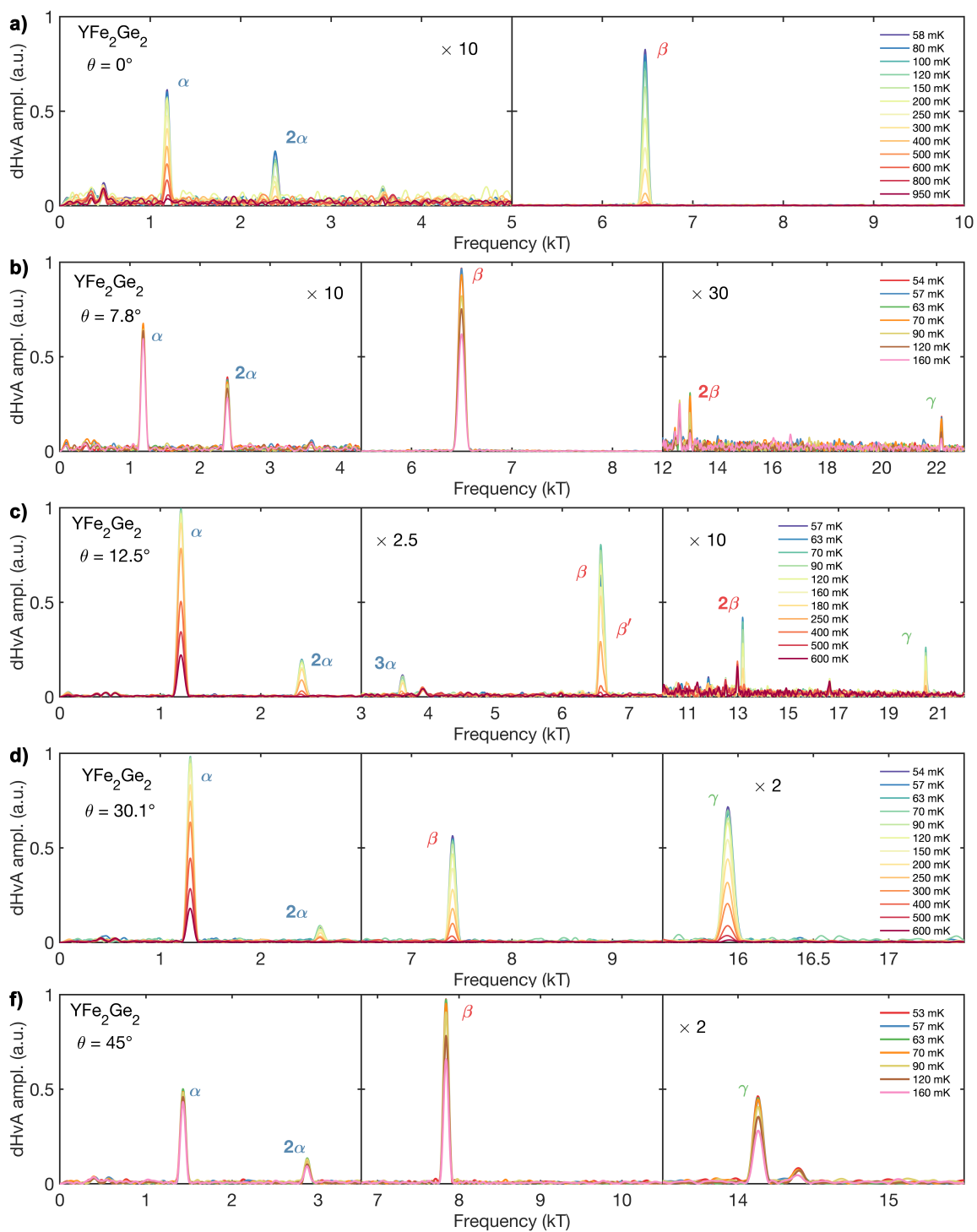
Fig. 5.34 FFT spectra for various field orientations showing the temperature dependence of a range of frequency peaks.
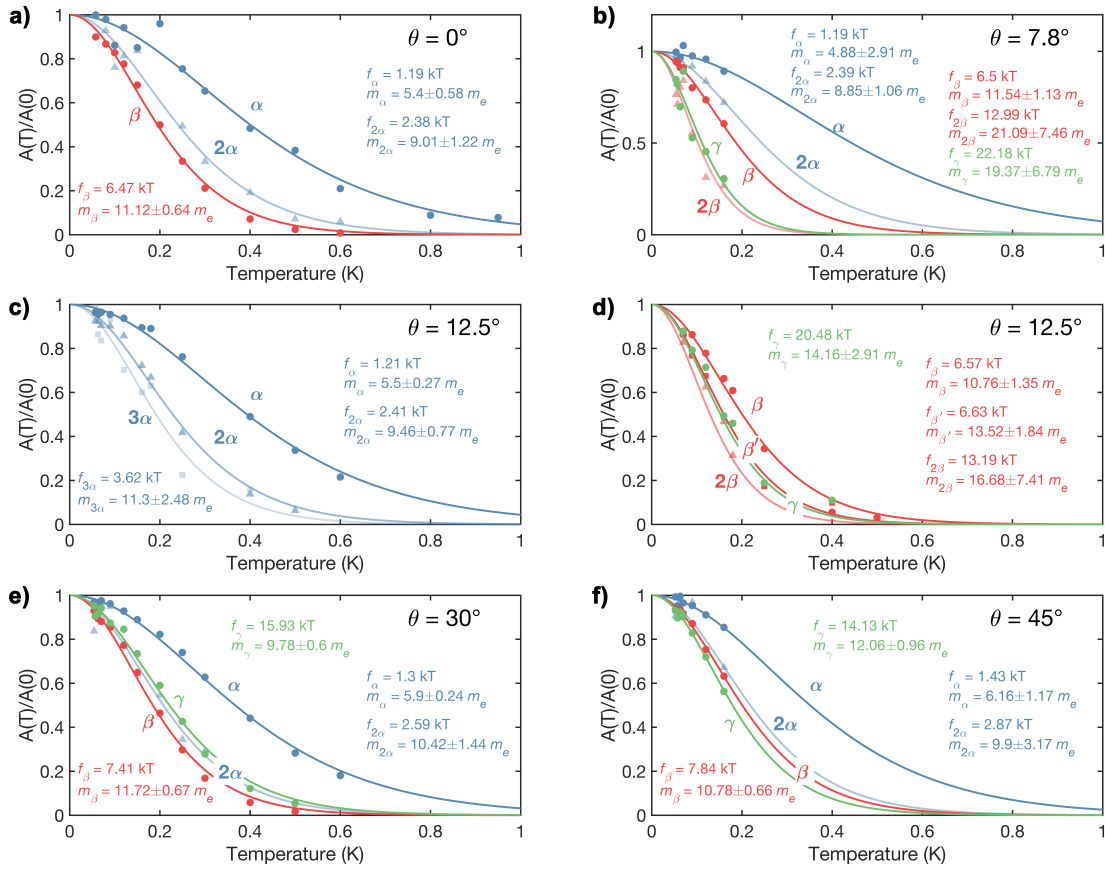
Fig. 5.35 Temperature dependence of the amplitudes of the α, β and γ oscillations and their harmonics (markers), and fits to the Lifshitz-Kosevich form for the temperature smearing factor (solid lines).

around half as high as those expected from the SKEAF calculation, we have assigned the α peaks (Fig. 5.30) to the hole-like Band 32 rather than the electron-like Band 35, because of the slow but smooth increase of the frequency towards $\theta = 90°$. The peaks which have double or triple the frequencies of those of the α and β fundamental peaks can be identified as harmonics. As we will see later, the extracted masses for these harmonic peaks share roughly the same multiplicity as the frequency ratios. In addition, there are also a range of unidentifiable peaks. Particularly at low frequencies of around 400 T, there exist multiple peaks (δ) which are weakly visible from the FFT spectra at different angles.

The temperature dependence of the dHvA amplitudes of the frequency peaks provides a means of estimating the quasi-particle masses on the different Fermi surfaces. Fig. 5.34 shows the FFT spectra in $1/B$ of the background-subtracted signals at varying temperatures for five different angles θ. The extracted oscillation amplitudes of the frequency peaks from the FFT spectra enable fittings of the thermal smearing factor R_T (Equ. 2.44) and hence allow us to estimate the renormalised quasiparticle masses. Here, we focus on the frequency peaks corresponding to the hole-like Fermi surface sheets. The low-frequency peaks at around 400 T and the occasionally visible peaks at higher frequencies do not show a strong reduction in oscillation amplitude at increased temperatures, at least at the investigated angles, suggesting low quasi-particle masses.

The normalised dHvA peak amplitudes (calculated as the areas under the peaks in the FFT spectrum by fitting each peak shape to a Gaussian function) as a function of temperature at $\theta = 0°$, 7.8°, 12.5°, 30.1° and 45° and the fittings of R_T of the Lifshitz-Kosevich theory are plotted in Fig. 5.35. The experimentally obtained QO frequencies of the three hole sheets and the fitted quasi-particle masses are further summarised in Table 5.5, and are compared with theoretical predictions from the DFT calculations.

The updated DFT calculations using the experimentally determined z-parameter suggests a bare Sommerfeld electronic specific heat coefficient $\gamma \approx 16\,\mathrm{mJ/molK^2}$, slightly higher than that predicted by [36]. The measured normal-state $\gamma_{norm} \approx 100\,\mathrm{mJ/molK^2}$ is hence around 6 times larger than the band-structure-calculated value. We therefore expect the quasi-particle masses to be similarly enhanced. However, as shown in the last column of Table 5.5, mass enhancement for the detected Fermi surface sheets appear to be between 3 and 5. This suggests that the hole sheets alone may not account for the specific heat enhancement and that there may be heavier Fermi surface sheets which are currently not observed, e.g. the electron sheet. Alternatively, electron correlations may be reduced at large applied fields. As shown in Fig 5.19 in Section 5.2, the heat capacity of YFe$_2$Ge$_2$ at 10 T appears to show a small reduction compared to the heat capacity measured at lower fields. It

Table 5.5 Comparison of experimentally observed orbit frequencies and quasi-particle masses with predictions from DFT calculations for the three hole bands.

Angle θ	DFT			Experiment			Mass enhancement
	Band	Freq. (kT)	Mass (m_e)	Orbit	Freq. (kT)	Mass (m_e)	
0°	32	2.89	1.58	α	1.19	5.4 ± 0.6	3.4 ± 0.4
		Harmonic		2α	2.38	9.0 ± 1.2	
	33	4.10	2.24	β	6.47	11.1 ± 0.6	5.0 ± 0.3
	34	28.29	8.89	γ	-	-	-
7.8°	32	2.90	1.59	α	1.19	4.9 ± 2.9	3.1 ± 1.8
		Harmonic		2α	2.39	8.9 ± 1.1	
	33	4.15	2.25	β	6.5	11.5 ± 1.1	5.1 ± 0.5
		Harmonic		2β	12.99	21.1 ± 7.5	
	34	24.13	5.54	γ	22.18	19.4 ± 6.8	3.5 ± 1.2
12.5°	32	2.91	1.60	α	1.21	5.5 ± 0.3	3.4 ± 0.2
		Harmonics		2α	2.41	9.5 ± 0.8	
				3α	3.62	11.3 ± 2.5	
	33	4.21	2.28	β	6.57	10.8 ± 1.4	4.7 ± 0.6
				β'	6.63	13.5 ± 1.8	5.9 ± 0.8
		Harmonic		2β	13.19	16.7 ± 7.4	
	34	22.21	4.44	γ	20.48	14.2 ± 2.9	3.2 ± 0.7
30.1°	32	3.04	1.66	α	1.3	5.9 ± 0.2	3.6 ± 0.1
		Harmonic		2α	2.59	10.4 ± 1.4	
	33	4.76	2.56	β	7.41	11.7 ± 0.7	4.6 ± 0.3
	34	17.39	2.74	γ	15.93	9.8 ± 0.6	3.6 ± 0.2
45°	32	3.25	1.76	α	1.43	6.2 ± 1.2	3.5 ± 0.7
		Harmonic		2α	2.87	9.9 ± 3.2	
	33	5.75	3.01	β	7.84	10.8 ± 0.7	3.6 ± 0.2
	34	14.71	2.45	γ	14.13	12.1 ± 1.0	4.9 ± 0.4

is possible that under an even higher field C/T continues to be suppressed, which may bring the enhancement factor closer to that estimated for the effective masses.

5.5 Summary

Through modifications of the conventional Sn-flux method, in particular by changing the growth protocols and the geometry of the growth set-up, we have successfully grown YFe$_2$Ge$_2$ single crystals which exhibit an order of magnitude improvement in residual resistivity ratio. Clear and sharp signatures of bulk superconductivity have been observed in these high-quality crystals. Low-temperature specific heat and muon spin rotation measurements have been performed on this new generation of single crystals. Results from both measurements revealed evidence for multi-gap superconductivity in YFe$_2$Ge$_2$, possibly of the s$^{\pm}$-wave state.

Quantum oscillations have been observed for the first time for YFe$_2$Ge$_2$ in this new generation of single-crystal samples. Three out of the four main Fermi surface sheets have been successfully identified. The angular dependence of the oscillation frequencies matches qualitatively with theoretical predictions from DFT calculations, proving the 3D electronic structure of YFe$_2$Ge$_2$. QO measurements revealed quasi-particle mass enhancements between 3 and 5 compared to the band-structure calculated values, less than the factor of 6 indicated by the enhancement of the normal-state Sommerfeld coefficient. This points to the possibility of a strongly renormalised heavy electron sheet, which is so far undetected. Further measurements at higher fields and lower temperatures may be required to clarify the missing masses.

Chapter 6

Summary and future prospects

The strong suppression of superconductivity by disorder has been the main obstacle in the investigation of unconventional superconductivity exhibited by the iron-based superconductor YFe_2Ge_2. Our persistent pursuit in improving the crystal growth techniques has led to significantly improved YFe_2Ge_2 sample quality. The availability of increasingly higher-quality crystals has gradually allowed the collection of experimental data on the intrinsic properties of both its normal and superconducting states. A clearer picture has thus begun to emerge regarding the position of YFe_2Ge_2 in the wider context of the iron-based superconductors.

At first sight, YFe_2Ge_2 appears to be an outlier among the layered iron-based superconductors. From the very beginning, the inclusion of a Group-IV element, Ge, into its building block sets it apart from the commonly studied pnictide and chalcogenide families. The bonding between the nearest germanium layers leads to its rather isotropic three-dimensional (3D) electronic structure, distinctive from the quasi-two-dimensional Fermi surfaces observed in other FeSCs. However, despite the apparent disparity in Fermiology, a closer inspection revealed many pronounced similarities between the physical properties of YFe_2Ge_2 with the isostructural alkali-metal iron arsenides $K/Cs/RbFe_2As_2$. It is also interesting to note that, although the electronic structures of these heavily hole-doped iron arsenides are very two-dimensional, their Fermi surfaces contain only hole sheets, which are again different from most other iron pnictides, in which a cylindrical electron sheet can be found in the Brillouin Zone corner.

In Section 5.2, we have already discussed the close resemblance of key features in the thermodynamic properties between YFe_2Ge_2 and the alkali-metal iron arsenides. To reiterate: (1) The normal-state low-temperature Sommerfeld coefficients are similarly enhanced in both systems compared to their respective band-structure calculated values and reach the order of $100\,\mathrm{mJ/molK^2}$; (2) The specific heat jumps $\Delta C(T_c)/T_c$ at the superconducting transition temperature are all around 50% or less of that of the normal state Sommerfeld coefficient

γ_{norm} just above the transition; (3) C/T in all samples maintains a sizeable fraction (around 50%) of γ_{norm} down to about $0.1T_c$. These features and the similarly strong suppression of T_c by the presence of impurities and disorder [17, 26] hint at an unconventional and possibly universal pairing mechanism among all four materials.

Moderate to strong electronic correlations are ubiquitously observed in FeSCs and have been thought to be important for understanding both their normal and superconducting state properties. In the alkali metal arsenides, evidence for strong electronic correlations stems from the large Sommerfeld coefficients and the sizeable quasi-particle mass enhancements [111]. In other iron pnictides, signatures of strong electron correlations were revealed by the significant reduction in the spectral weight of the Drude peak in optical conductivity compared to those expected from non-interacting electrons [118, 119], and mass renormalisation has been observed in angle-resolved photoemission spectroscopy (ARPES) in some systems where the effective masses were seen to be 3 to 4 times larger than the calculated band mass [120, 121]. On the other hand, mass enhancement as high as 20 has been observed in the iron chalcogenides [122, 123]. Furthermore, many, if not all, layered FeSCs can be characterised as "bad metals", according to the Mott-Ioffe-Regel criterion [124, 125] with their room temperature resistivity $\approx 1\,\text{m}\Omega\,\text{cm}$. Electron-phonon scattering alone is expected to only give a much smaller contribution to resistivity (of the order $\mu\Omega\,\text{cm}$) [125], which again implies strong electron-electron interactions in the FeSCs. In this respect, YFe_2Ge_2, with an effective mass renormalisation factor (compared to the band mass) of 3-5 and $\rho(300\,\text{K}) \approx 200\,\mu\Omega\,\text{cm}$, falls in the same category.

The presence of strong electronic correlations is important partly because it suggests that the traditional approach in terms of the standard single-particle schemes may not be sufficient for understanding the electronic properties in FeSCs. While results from DFT calculations are able to capture the key features of the bandstructure and the topology of the Fermi surfaces, magnetism in FeSCs has, in this approach, been understood in terms of the nesting between Fermi surfaces, whose effects alone can not account for the large integrated spin spectral weight observed, for example, by inelastic neutron experiment in the iron pnictides [126]. At the opposite end of the spectrum, by postulating the closeness to a Mott insulating state, the magnetism of these materials can be successfully modelled, but the metallic behaviour and spin-fluctuation mediated superconductivity have to be considered as resulting from charge doping [127]. A middle ground to this dichotomy is to place FeSCs in the *intermediate* correlation regime and to consider the multi-orbital nature of their electronic states. In this view, Hund's coupling J_H, namely the energy scale associated with intra-atomic exchange becomes important. It lowers the cost of Coulomb repulsion when two electrons with parallel spins are placed in different orbitals on the same Fe-site, as

opposed to them being in the same orbital. The interplay between the Hubbard interaction (associated with direct Coulomb repulsion), U, and J_H can lead to different behaviours for the different orbitals, causing "orbital decoupling" [128]. Correlations may therefore be tuned independently on the separate orbitals, resulting in a subset of the orbitals undergoing Mott localisation, which is termed *selective Mottness* or orbitally selective Mott physics (OSMP) [127]. Support for this coexistence of both strongly and weakly correlated electrons has been found in both experiments and realistic calculations which considers correlations on top of DFT. ARPES measurements have revealed strong orbital-dependent correlation effects in iron chalcogenides [123], and analyses of the experimental results from thermodynamic and quantum oscillation measurements of the hole-doped 122 iron arsenides in parallel with DFT + slave spin calculations also support the OSMP scenario [111]. In view of the widely varying electronic structures displayed by the FeSCs, for example the 3D Fermi surfaces of YFe_2Ge_2 versus the quasi-2D ones of the other compounds, OSMP, whose tuning
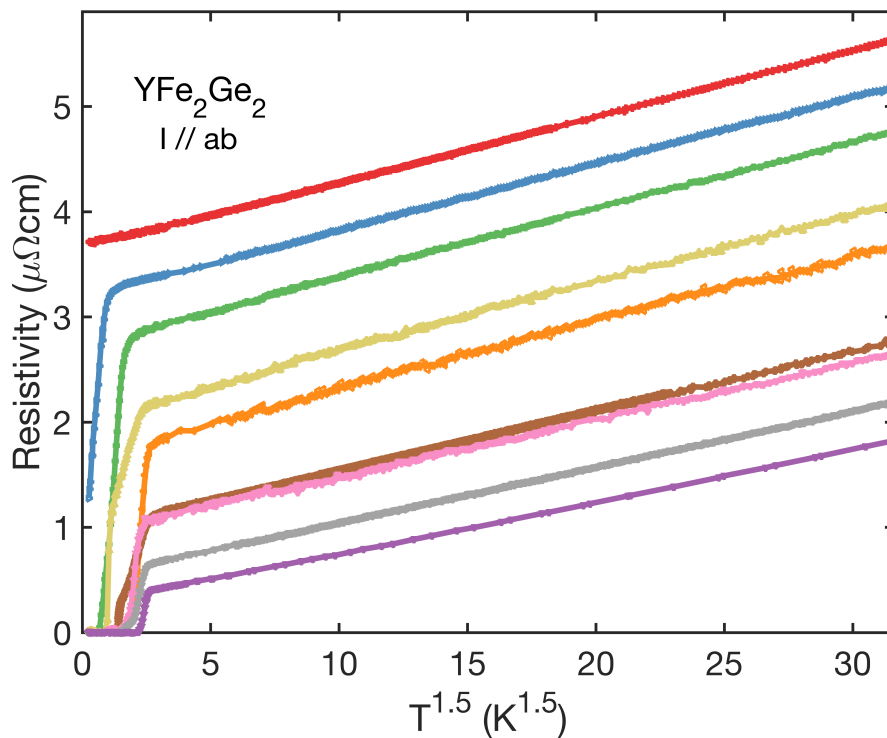

Fig. 6.1 Electrical resistivity of a range of single-crystal YFe_2Ge_2 with varying sample quality showing a $T^{1.5}$ power-law temperature dependence. Electrical current has been applied along the ab-plane for these measurements.

parameter is the doping of each orbital with respect to half filling, may be more suitable for understanding their physical properties than the traditional weak-coupling description.

Although similarities exist between YFe_2Ge_2 and the wider classes of FeSCs, there are certain features, apart from its unusual 3D electronic structure, which appear to be unique in this system. So far, all YFe_2Ge_2 samples, regardless of their RRRs, display an anomalous $T^{1.5}$ power-law temperature dependence in their low-temperature normal-state resistivity (see e.g. Fig. 6.1), signalling non-Fermi liquid behaviour. Although an early study of KFe_2As_2 claimed a similar $T^{1.5}$ behaviour in resistivity [129], a T^2 temperature dependence was showed by most other studies on samples with varying RRRs [130, 131]. Similar observations have been reported in $RbFe_2As_2$ as well [31, 132]. Meanwhile, in the doping series $BaFe_2(As_{1-x}P_x)_2$, non-Fermi liquid behaviour has been observed where resistivity shows a T^α power-law behaviour with α varying between 1 and 2 depending on the doping level [133]. This has been suggested to originate from an underlying antiferromagnetic quantum critical point at $x \approx 0.33$ [134]. Besides this doping series, the $T^{1.5}$ resistivity
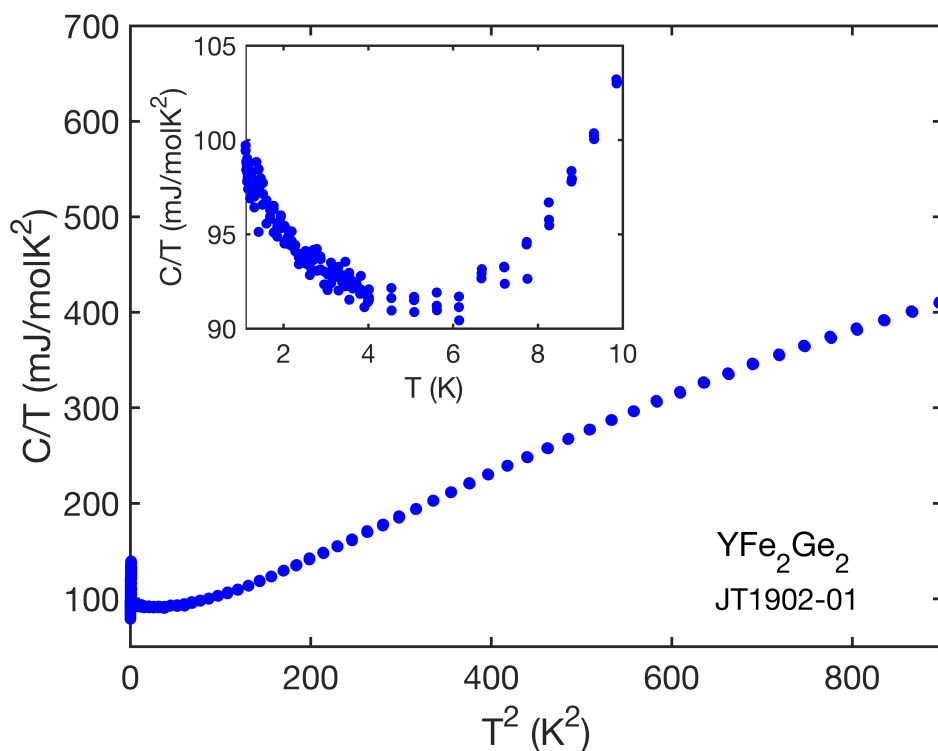
Fig. 6.2 C/T against T^2 of a YFe_2Ge_2 sample from growth batch JT1902. (inset) C/T versus temperature showing an unusual upturn below around 6 K.

behaviour has not been found in other FeSCs. This unusual temperature dependence may be a hint of another quantum critical point (QCP) in the proximity of YFe_2Ge_2, for instance, in the phase space of $Lu_{1-x}Y_xFe_2Ge_2$ [22, 28]. Furthermore, the robustness of non-Fermi liquid (NFL) behaviour even in the highest quality sample of YFe_2Ge_2 is surprising, because such behaviour is only expected very close to the QCP and tends to quickly recover to Fermi
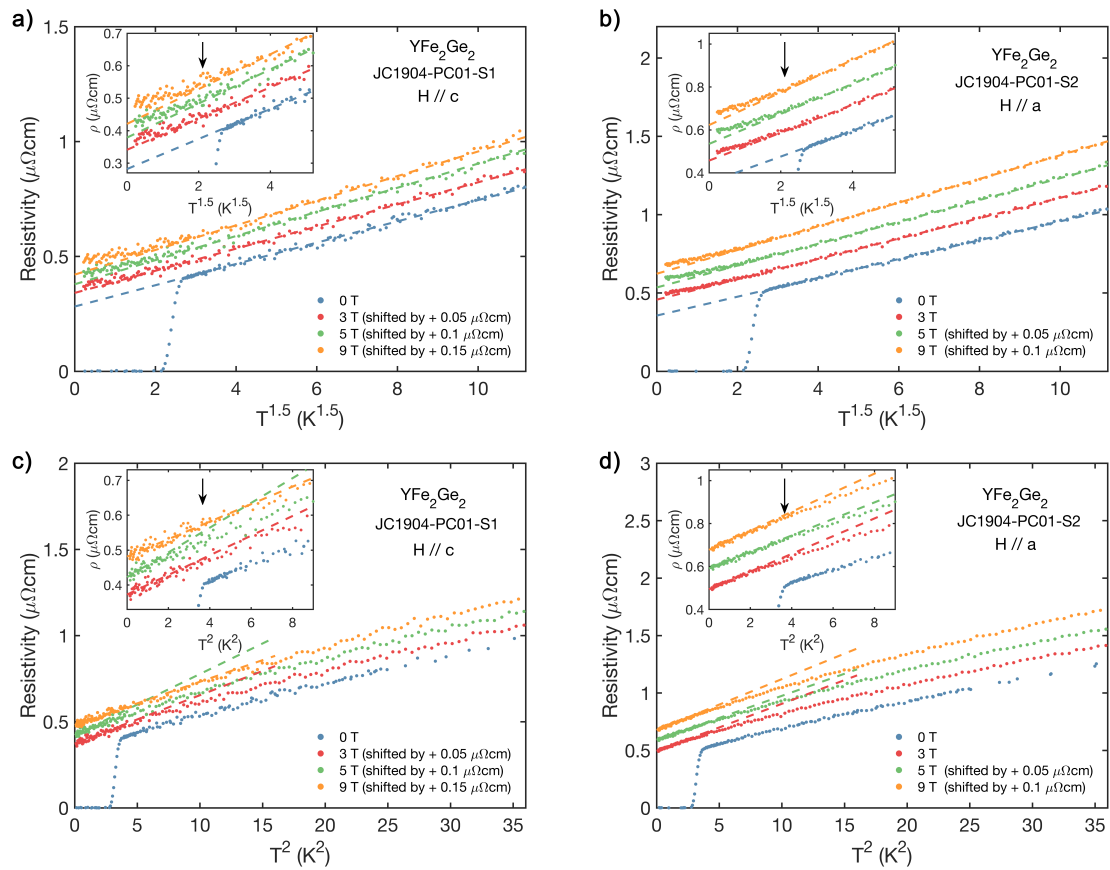
Fig. 6.3 Electrical resistivity of YFe_2Ge_2 under three different applied magnetic fields, with (a, c) **H** $\|$ c and (b, d) **H** $\|$ ab. (insets) Zoomed in plots at low temperature parts of the data. There appears to be a transition from $T^{1.5}$ to T^2 behaviour of the electrical resistivity at low temperature at high fields. The dashed lines in (a) and (b) are linear fittings to data of corresponding colours between 2 and 4 K, and those in (c) and (d) are linear fittings to data below 1 K. The arrows in the insets indicate roughly the temperatures at which the resistivity data start to deviate from the $T^{1.5}$ or T^2 power-law behaviour at 9 T. Some of the data have been shifted as indicated in the legend for clarity.

liquid (FL) bahaviour away from the QCP. This material is thus reminiscent of β-YbAlB$_4$, where quantum criticality is reached without any external tuning [135, 136].

Magnetic field may be used to tune a system closer to or away from a quantum critical point. Fig. 6.3 shows the result of a prelimiary study of the effect of magnetic field (large enough to completely suppress superconductivity) on the low-temperature normal-state resistivity in YFe$_2$Ge$_2$. While the signal-to-noise ratio is not good enough to allow a detailed investigation of the temperature-dependent exponent of the power-law behaviour, Fig. 6.3 reveals a crossover from $T^{1.5}$ to T^2 behaviour of the resistivity at low temperature. This is most clearly seen in the insets of Fig. 6.3(b) and (d) for resistivity data measured at magnetic field of 9 T applied in along the crystallographic a-direction. This transition from non-Fermi liquid to Fermi liquid behaviour at low temperatures is typical of materials in the proximity of a QCP and on the opposite side to a magnetic transition [137–139]. The inset of Fig. 6.3(b) also indicates a gradual increase of the crossover temperature between NFL and FL behaviour with increasing magnetic field. Further measurements with better signal optimisation are needed to map out this field dependence, which will help locate YFe$_2$Ge$_2$ in relation to the QCP.

Apart from the anomalous temperature dependence of the resistivity, the normal-state electronic specific heat of YFe$_2$Ge$_2$ also displays an unusual feature at low temperature. Fig. 6.2 shows C/T of a YFe$_2$Ge$_2$ single crystal. A small upturn in the normal-state C/T is clearly observed below 6 K in the inset of this figure. While the origin of such a C/T upturn is currently unclear, one may suspect an association with the presence of magnetic fluctuations, similar to those observed in compounds in proximity to magnetic order, such as CeCu$_2$Si$_2$ [140]. In fact, both a stripe-type antiferromagnetic and an in-plane ferromagnetic spin fluctuation have been detected in a recent inelastic neutron experiment of the normal state of YFe$_2$Ge$_2$ [38]. The competition of ferromagnetic and stripe magnetic instabilities is not unique to YFe$_2$Ge$_2$. In the Co-doped iron arsenides AFe$_{2-x}$Co$_x$As$_2$, nuclear magnetic resonance (NMR) measurements have showed evidence of a similar coexistence of both types of magnetic spin fluctuations [141], which has been suggested to be a cause of the suppression of superconductivity in the Co-overdoped samples. It is most likely that the competition of the magnetic instabilities underpins much of the normal-state and superconducting properties in YFe$_2$Ge$_2$ and deserves further scrutiny.

In summary, YFe$_2$Ge$_2$ presents a special case in the slowly growing family of FeSCs with its very isotropic electronic structure, but also shares a number of key characteristics with the other Fe-based compounds, in particular, the alkali metal iron arsenides. The rich chemistry and variety of possible electronic structures exhibited by the FeSCs make it

possible to test both material-specific and unified theories of strong electronic correlation and superconductivity.

Future prospects

Superconducting order parameter in YFe$_2$Ge$_2$

Although low-temperature μSR and specific heat measurements have provided hints for possible pairing states of the superconducting order parameter in YFe$_2$Ge$_2$, further experimental investigations will be needed to decide between the various possible scenarios. Many of these experiments are currently under way or have been planned:

- Thermal conductivity $\kappa(T)$ is a useful probe of low energy thermal excitations. In a superconductor, at temperatures far below T_c, both the specific heat $C(T)$ and $\kappa(T)$ are expected to contain only electronic contributions. The temperature dependence of $C(T)$ and $\kappa(T)$ at these low temperatures therefore can reveal crucial information regarding the structure of the superconducting gap function, in particular, the presence of nodal structures. The measurement of thermal conductivity is advantageous over specific heat at the lowest temperatures in that it does not suffer from nuclear Schottky anomalies. Furthermore, under applied magnetic field H below the upper critical field H_{c2}, $\kappa(H, T \to 0)$ encodes information about how the low energy density of state (DOS) changes in the vortex state as a function of H, which again depends sensitively on the superconducting gap structure.

  Thermal conductivity measurements of YFe$_2$Ge$_2$ down to 50 mK are currently being carried out by Prof. Robert Hill's group in University of Waterloo. Both poly- and single crystal samples with varying RRRs above 170 will be investigated. Given the striking similarities between thermodynamic properties in heat capacity of YFe$_2$Ge$_2$ and KFe$_2$As$_2$, it will be interesting to compare their thermal conductivity data. This may also provide new insights for resolving the controversy regarding the gap structure in KFe$_2$As$_2$ [17, 20].

- The London penetration depth $\lambda(T)$ is closely linked to the superfluid density $\rho_s(T)$ below T_c. While our μSR experiment has allowed the determination of an overall form of $\lambda(T)$ below T_c, the accurate behaviour at lowest temperatures is difficult to discern due to the scarce data points from the measurement. An alternative method of measuring $\lambda(T)$ is provided by the tunnel-diode resonance (TDR) technique, in which the gradual variation of the penetration depth can be tracked with much finer temperature steps. In collaboration with Prof. Huiqiu Yuan's group in the Centre of Correlated Matter in Hangzhou, the temperature dependence of the penetration depth in the new YFe$_2$Ge$_2$ samples will be measured down to 50 mK.

- From nuclear magnetic resonance (NMR) measurements, one may obtain three major quantities, namely Knight shift $K(T)$, T_1 and T_2 relaxation times, in which $K(T)$ and $1/T_1$ are directly related to the DOS of a metal and can therefore also provide information of the superconducting gap function of a superconductor. NMR measurements on YFe_2Ge_2 will be carried out by Prof. Kenji Ishida's group in Kyoto University.

- Inelastic neutron scattering (INS) experiments can provide crucial information about magnetic excitations in a material. A characteristic resonance within the superconducting state has been observed by INS in a wide range of iron-based superconductors [13–15]. This resonance mode is believed to arise from sign reversed quasi-particle excitations, which is consistent with an $s^{\pm}$ or a d-wave pairing state. With a resonance energy $E_r \approx 4.9 k_B T_c$, this spin resonance is generally observed at a wavevector compatible with the anti-ferromagnetic ordering wavevector of the non-superconducting parent compound. Collaborating with Dr. Devashibhai Adroja, we will be searching for the presence of spin resonance in single-crystal YFe_2Ge_2 in an upcoming INS experiment on the LET instrument at the ISIS neutron and muon source. Measurement time for this experiment has already been granted.

Origin of the unusual normal state in YFe_2Ge_2

The intermetallic compound YFe_2Ge_2, with its unusually strong electronic correlations, appears to be a unique case among a number of isostructural transition-metal compounds, for examples $LuTE_2Si_2$, $LaTE_2Ge_2$ and YTE_2Si_2 where TE are d-electron transition metals [142–145]. Although some of these compound also show superconductivity, they all appear to be of the conventional kind. Among these different 122 transition-metal compounds, the Fe-based compounds again show a comparatively higher Sommerfeld coefficient C/T of between 20 and $60\,\text{mJ/molK}^2$ at the lowest temperatures.

In order to investigate the unusual normal state of YFe_2Ge_2, such as the origin of the unusually high electronic heat capacity and the cause of the non-Fermi liquid behaviour of its resistivity, it will be instructive to study the various related compounds, in particular, YFe_2Si_2 and $LuFe_2Ge_2$. Similar to YFe_2Ge_2, DFT calculations suggest competition between multiple magnetic orders in YFe_2Si_2 [146]. Although not as significantly enhanced, YFe_2Si_2 also displays a sizeable Sommerfeld coefficient $C/T \approx 65\,\text{mJ/molK}^2$ (from our measurement on poly-crystalline samples) which is around 5 times the band-structure value. So far, no superconducting transition has been observed in YFe_2Si_2, but that may change with improved sample quality, as was found in YFe_2Ge_2. By comparing and contrasting the various physical properties of YFe_2Ge_2 and YFe_2Si_2, one may be able to understand the cause of their

electronic correlations. On the other hand, A-type magnetic order is realised in $LuFe_2Ge_2$ below $9\,K$ [34, 147]. This transition temperature can be suppressed by replacing lutetium with yttrium [28], raising the possibility of a QCP, which may be linked to the unusual normal-state properties in YFe_2Ge_2. Since the doping series $Lu_{1-x}Y_xFe_2Ge_2$ can be grown using traditional Sn-flux method, it is natural to adopt the liquid transport method for growing the same composition series to obtain high-quality crystals near to the critical composition. One may expect magnetic fluctuations associated with A-type order to be amplified near the critical point. It will therefore be interesting to investigate how the $T^{1.5}$ resistivity behaviour evolves as we approach the critical composition. If superconductivity in YFe_2Ge_2 is mediated by these magnetic fluctuations, we may also expect to observe an increase in T_c as the system is tuned towards $LuFe_2Ge_2$ by chemical substitution. However, it is likely that disorder from chemical substition and anti-site defects will act to suppress T_c, instead.

References

[1] Drozdov, A. P., Eremets, M. I., Troyan, I. A., Ksenofontov, V. & Shylin, S. I. Conventional superconductivity at 203 Kelvin at high pressures in the sulfur hydride system. *Nature* **525**, 73–76 (2015).

[2] Drozdov, A. P. *et al.* Superconductivity at 250 K in lanthanum hydride under high pressures. *Nature* **569**, 528–531 (2019).

[3] Paglione, J. & Greene, R. L. High-temperature superconductivity in iron-based materials. *Nature Physics* **6**, 645–658 (2010). 1006.4618.

[4] Basov, D. N. & Chubukov, A. V. Manifesto for a higher T_c. *Nature Physics* **7**, 272–276 (2011).

[5] Chubukov, A. & Hirschfeld, P. J. Iron-based superconductors, seven years later. *Physics Today* **68**, 46–52 (2015).

[6] Kamihara, Y. *et al.* Iron-based layered superconductor: LaOFeP. *Journal of the American Chemical Society* **128**, 10012–10013 (2006).

[7] Ogino, H. *et al.* Superconductivity at 17 K in $(Fe_2P_2)(Sr_4Sc_2O_6)$: a new superconducting layered pnictide oxide with a thick perovskite oxide layer. *Superconductor Science and Technology* **22**, 075008 (2009). 0903.3314.

[8] Shirage, P. M. *et al.* Emergence of Superconductivity in "32522" Structure of $(Ca_3Al_2O_{5-y})(Fe_2Pn_2)$ (Pn = As and P). *Journal of the American Chemical Society* **133**, 9630–9633 (2011).

[9] Chen, H. *et al.* Coexistence of the spin-density wave and superconductivity in $Ba_{1-x}K_xFe_2As_2$. *EPL (Europhysics Letters)* **85**, 17006 (2009). arXiv:0807.3950v1.

[10] Alireza, P. L. *et al.* Superconductivity up to 29 K in $SrFe_2As_2$ and $BaFe_2As_2$ at high pressures. *Journal of physics. Condensed matter : an Institute of Physics journal* **21**, 012208 (2009). 0807.1896.

[11] Ni, N. *et al.* Phase diagrams of $Ba(Fe_{1-x}M_x)_2As_2$ single crystals (M = Rh and Pd). *Physical Review B - Condensed Matter and Materials Physics* **80**, 1–7 (2009).

[12] Hosono, H. & Kuroki, K. Iron-based superconductors: Current status of materials and pairing mechanism. *Physica C: Superconductivity and its Applications* **514**, 399–422 (2015).

[13] Lumsden, M. D. & Christianson, A. D. Magnetism in Fe-based superconductors. *Journal of Physics Condensed Matter* **22** (2010).

[14] Dai, P. Antiferromagnetic order and spin dynamics in iron-based superconductors. *Reviews of Modern Physics* **87**, 855–896 (2015).

[15] Xie, T. *et al.* Neutron Spin Resonance in the 112-Type Iron-Based Superconductor. *Physical Review Letters* **120**, 1–7 (2018).

[16] Hirschfeld, P. J., Korshunov, M. M. & Mazin, I. I. Gap symmetry and structure of Fe-based superconductors. *Reports on Progress in Physics* **74** (2011). 1106.3712.

[17] Reid, J. P. *et al.* From d-wave to s-wave pairing in the iron-pnictide superconductor $(Ba,K)Fe_2As_2$. *Superconductor Science and Technology* **25** (2012).

[18] Reid, J. P. *et al.* Universal heat conduction in the iron arsenide superconductor KFe_2As_2: Evidence of a d-wave state. *Physical Review Letters* **109**, 1–5 (2012).

[19] Okazaki, K. *et al.* Octet-Line Node Structure of Superconducting Order Parameter in KFe_2As_2. *Science* **337**, 1314–1317 (2012).

[20] Hardy, F. *et al.* Multiband superconductivity in KFe_2As_2: evidence for one isotropic and several Liliputian energy gaps. *J. Phys. Soc. Jpn.* **83**, 014711 (2014).

[21] Bernardini, F. *et al.* Iron-based superconductivity extended to the novel silicide LaFeSiH. *Physical Review B* **97**, 2–6 (2018). 1701.05010.

[22] Zou, Y. *et al.* Fermi liquid breakdown and evidence for superconductivity in YFe_2Ge_2. *Physica Status Solidi - Rapid Research Letters* **8**, 928–930 (2014).

[23] Chen, J. *et al.* Unconventional superconductivity in the layered iron germanide YFe_2Ge_2. *Physical Review Letters* **116**, 127001 (2016).

[24] Kim, H. *et al.* Crystal growth and annealing study of fragile, non-bulk superconductivity in YFe_2Ge_2. *Philosophical Magazine* **95**, 804–818 (2015).

[25] Felner, I., Lv, B., Zhao, K. & Chu, C. W. High-pressure resistivity of YFe_2Si_2 and magnetic studies of $Y_{1-y}Ho_yFe_2Si_2$ and $YFe_2(Si_{1-x}Ge_x)_2$ systems. *Journal of Superconductivity and Novel Magnetism* **28**, 1207–1216 (2015).

[26] Chen, J., Gamża, M. B., Semeniuk, K. & Grosche, F. M. Composition dependence of bulk superconductivity in YFe_2Ge_2. *Physical Review B* **99**, 1–5 (2019).

[27] Semeniuk, K. *Correlated low temperature states of YFe_2Ge_2 and pressure metallised NiS_2*. PhD thesis, University of Cambridge (2018).

[28] Ran, S., Bud'Ko, S. L. & Canfield, P. C. Effects of substitution on low-temperature physical properties of $LuFe_2Ge_2$. *Philosophical Magazine* **91**, 4388–4400 (2011).

[29] Fujiwara, T. *et al.* Pressure effect on magnetic short range ordering of $LuFe_2Ge_2$. *Journal of the Physical Society of Japan* **76**, 60–61 (2007).

[30] Sasmal, K. *et al.* Superconducting fe-based compounds $(A_{1-x}Sr_x)Fe_2As_2$ with A = K and Cs with transition temperatures up to 37 K. *Physical Review Letters* **101**, 8–11 (2008).

[31] Zhang, Z. *et al.* Heat transport in $RbFe_2As_2$ single crystals: Evidence for nodal superconducting gap. *Physical Review B - Condensed Matter and Materials Physics* **91**, 1–5 (2015).

[32] Wang, A. F. *et al.* Calorimetric study of single-crystal $CsFe_2As_2$. *Physical Review B - Condensed Matter and Materials Physics* **87**, 2–7 (2013).

[33] Nakajima, Y. *et al.* High-temperature superconductivity stabilized by electron-hole interband coupling in collapsed tetragonal phase of KFe_2As_2 under high pressure. *Physical Review B - Condensed Matter and Materials Physics* **91**, 1–5 (2015).

[34] Avila, M., Bud'ko, S. & Canfield, P. Anisotropic magnetization, specific heat and resistivity of RFe_2Ge_2 single crystals. *Journal of Magnetism and Magnetic Materials* **270**, 51–76 (2004).

[35] Subedi, A. Unconventional sign-changing superconductivity near quantum criticality in YFe_2Ge_2. *Physical Review B - Condensed Matter and Materials Physics* **89**, 1–5 (2014).

[36] Singh, D. J. Superconductivity and magnetism in YFe_2Ge_2. *Physical Review B - Condensed Matter and Materials Physics* **89**, 1–6 (2014).

[37] Sirica, N. *et al.* Spectroscopic evidence for strong quantum spin fluctuations with itinerant character inYFe_2Ge_2. *Physical Review B* **91**, 1–5 (2015).

[38] Wo, H. *et al.* Coexistence of Ferromagnetic and Stripe-Type Antiferromagnetic Spin Fluctuations in YFe2Ge2. *Physical Review Letters* **122**, 217003 (2019).

[39] Ashcroft, N. & Mermin, N. *Solid State Physics.* HRW international editions (Holt, Rinehart and Winston, 1976).

[40] Tinkham, M. *Introduction to Superconductivity*, vol. 1 (Dover Publications, 2004).

[41] Bardeen, J., Cooper, L. N. & Schrieffer, J. R. Theory of Superconductivity. *Physical Review* **108**, 1175–1204 (1957). 1101.0277.

[42] Annett, J. F. *Superconductivity, superfluids and condensates*, vol. 5 (Oxford University Press, 2004).

[43] Mühlschlegel, B. Die thermodynamischen Funktionen des Supraleiters. *Zeitschrift für Physik* **155**, 313–327 (1959).

[44] Johnston, D. C. Elaboration of the α-model derived from the BCS theory of superconductivity. *Superconductor Science and Technology* **26** (2013).

[45] Werthamer, N. R., Helfand, E. & Hohenberg, P. C. Temperature and Purity Dependence of the Superconducting Critical Field, H_{c2}. III. Electron Spin and Spin-Orbit Effects. *Physical Review* **147**, 295–302 (1966).

[46] Clogston, A. M. Upper limit for the critical field in hard superconductors. *Physical Review Letters* **9**, 266–267 (1962). 0810.2605.

[47] Liu, Y. & Mao, Z. Q. Unconventional superconductivity in Sr_2RuO_4. *Physica C: Superconductivity and its Applications* **514**, 339–353 (2015).

[48] Tsuei, C. C. & Kirtley, J. R. Pairing symmetry in cuprate superconductors. *Reviews of Modern Physics* **72**, 969–1016 (2000). 0002341.

[49] Stewart, G. R. Unconventional superconductivity. *Advances in Physics* **66**, 75–196 (2017). 1705.05593.

[50] Bouquet, F. *et al.* Phenomenological two-gap model for the specific heat of MgB_2. *Europhysics Letters (EPL)* **56**, 856–862 (2001). 0107196.

[51] Padamsee, H., Neighbor, J. E. & Shiffman, C. A. Quasiparticle phenomenology for thermodynamics of strong-coupling superconductors. *Journal of Low Temperature Physics* **12**, 387–411 (1973).

[52] Carrington, A. & Manzano, F. Magnetic penetration depth of MgB_2. *Physica C: Superconductivity and its Applications* **385**, 205–214 (2003).

[53] Khasanov, R. & Guguchia, Z. Probing the multi gap behavior within '11' and '122' families of iron based superconductors: The muon-spin rotation studies. *Superconductor Science and Technology* **28** (2015).

[54] Prozorov, R. & Giannetta, R. W. Magnetic penetration depth in unconventional superconductors. *Superconductor Science and Technology* **19** (2006).

[55] Bang, Y. & Stewart, G. R. Superconducting properties of the $s^{\pm}$-wave state: Fe-based superconductors. *Journal of Physics Condensed Matter* **29**, aa564b (2017).

[56] Anderson, P. Theory of dirty superconductors. *Journal of Physics and Chemistry of Solids* **11**, 26–30 (1959).

[57] Abrikosov, A. A. & Gor'kov, L. P. Contribution to the theory of superconducting alloys with paramagnetic impurities. *Sov.Phys-JETP* **12**, 1243 (1961).

[58] Millis, A. J., Sachdev, S. & Varma, C. M. Inelastic scattering and pair breaking in anisotropic and isotropic superconductors. *Physical Review B* **37**, 4975–4986 (1988).

[59] Radtke, R. J., Levin, K., Schuttler, H. B. & Norman, M. R. Predictions for impurity-induced T_c suppression in the high-temperature superconductors. *Physical Review B* **48**, 653–656 (1993).

[60] Bang, Y., Choi, H. Y. & Won, H. Impurity effects on the $s^{\pm}$-wave state of the iron-based superconductors. *Physical Review B - Condensed Matter and Materials Physics* **79**, 1–8 (2009).

[61] Onari, S. & Kontani, H. Violation of anderson's theorem for the sign-reversing *s*-wave state of iron-pnictide superconductors. *Physical Review Letters* **103**, 4–7 (2009).

[62] Balatsky, A. V., Vekhter, I. & Zhu, J. X. Impurity-induced states in conventional and unconventional superconductors. *Reviews of Modern Physics* **78**, 373–433 (2006).

[63] Hussey, N. E. Low-energy quasiparticles in high-T_c cuprates. *Advances in Physics* **51**, 1685–1771 (2002).

[64] Schenck, A. Muon spin rotation spectroscopy: principles and applications in solid state physics (1985).

[65] Yaouanc, A. & De Reotier, P. D. *Muon spin rotation, relaxation, and resonance: applications to condensed matter*, vol. 147 (Oxford University Press, 2011).

[66] Sonier, J. E., Brewer, J. H. & Kiefl, R. F. μSR studies of the vortex state in type-II superconductors. *Reviews of Modern Physics* **72**, 769–811 (2000).

[67] Maisuradze, A., Khasanov, R., Shengelaya, A. & Keller, H. Comparison of different methods for analyzing μsR line shapes in the vortex state of type-II superconductors. *Journal of Physics Condensed Matter* **21** (2009).

[68] Lee, S. Using muons to probe the vortex lattice in superconductors. In *Muon Science*, 149–163 (Routledge, 2017).

[69] Schubnikow, L. & de Haas, W. Magnetic resistance increase in single crystals of bismuth at low temperatures. *Proceedings of the Koninklijke Akademie Van Weten-schappen te Amsterdam* **33**, 130–133 (1930).

[70] de Haas, W. J. & van Alphen, P. M. The dependence of the susceptibility of diamagnetic metals upon the field. *Commun. Phys. Lab. Univ. Leiden* 212a (1930).

[71] Shoenberg, D. *Magnetic oscillations in metals* (Cambridge university press, 2009).

[72] Feng, Z. *Sample growth and high pressure studies of novel strongly correlated systems, Dissertation, Schoenberg Laboratory for Quantum Matter, University of Cambridge* (2012).

[73] Canfield, P. C. & Fisk, Z. Growth of single crystals from metallic fluxes. *Philosophical Magazine B: Physics of Condensed Matter; Statistical Mechanics, Electronic, Optical and Magnetic Properties* **65**, 1117–1123 (1992).

[74] Kanatzidis, M. G., Pöttgen, R. & Jeitschko, W. The metal flux: A preparative tool for the exploration of intermetallic compounds. *Angewandte Chemie - International Edition* **44**, 6996–7023 (2005).

[75] Fisher, I. R., Shapiro, M. C. & Analytis, J. G. Principles of crystal growth of intermetallic and oxide compounds from molten solutions. *Philosophical Magazine* **92**, 2401–2435 (2012).

[76] Yan, J.-Q., Sales, B. C., Susner, M. A. & McGuire, M. A. Flux growth in a horizontal configuration: An analog to vapor transport growth. *Physical Review Materials* **1**, 023402 (2017).

[77] Design, Q. *Physical Property Measurement System Heat Capacity Option User's Manual* (2004).

[78] *S700X SQUID Magnetometer User Manual ver 0.96* (Cyogenic Ltd).

[79] Logg, P. *Superconductivity in the proximity of a quantum critical point. PhD thesis, University of Cambridge* (2014).

[80] Hwang, J. S., Lin, K. J. & Tien, C. Measurement of heat capacity by fitting the whole temperature response of a heat-pulse calorimeter. *Review of Scientific Instruments* **68**, 94–101 (1997).

[81] Wikipedia contributors. X-ray crystallography — Wikipedia, the free encyclopedia (2019). URL https://en.wikipedia.org/w/index.php?title=X-ray_crystallography&oldid=920801051. [Online; accessed 21-October-2019].

[82] Rietveld, H. M. A profile refinement method for nuclear and magnetic structures. *Journal of Applied Crystallography* **2**, 65–71 (1969).

[83] Rodríguez-Carvajal, J. Recent advances in magnetic structure determination by neutron powder diffraction. *Physica B: Condensed Matter* **192**, 55–69 (1993).

[84] Mccusker, L. B., Von Dreele, R. B., Cox, D. E., Louër, D. & Scardi, P. Rietveld refinement guidelines. *Journal of Applied Crystallography* **32**, 36–50 (1999).

[85] Le Bail, A. Whole powder pattern decomposition methods and applications: A retrospection. *Powder Diffraction* **20**, 316–326 (2005).

[86] Ishikawa, M., Braun, H. F. & Jorda, J. L. Effect of composition on the superconductivity of $CeCu_2Si_2$. *Physical Review B* **27**, 3092–3095 (1983).

[87] Mao, Z. Q., Mori, Y. & Maeno, Y. Suppression of superconductivity in Sr_2RuO_4 caused by defects. *Physical Review B - Condensed Matter and Materials Physics* **60**, 610–614 (1999).

[88] Stockert, O. *et al.* Magnetically driven superconductivity in $CeCu_2Si_2$. *Nature Physics* **7**, 119–124 (2011).

[89] Pfleiderer, C., Julian, S. R. & Lonzarich, G. G. Non-Fermi-liquid nature of the normal state of itinerant-electron ferromagnets. *Nature* **414**, 427–430 (2001).

[90] Takashima, S. *et al.* Robustness of non-Fermi-liquid behavior near the ferromagnetic critical point in clean $ZrZn_2$. *Journal of the Physical Society of Japan* **76**, 2–3 (2007).

[91] Smith, R. P. *et al.* Marginal breakdown of the Fermi-liquid state on the border of metallic ferromagnetism. *Nature* **455**, 1220–1223 (2008).

[92] Brando, M. *et al.* Logarithmic Fermi-liquid breakdown in $NbFe_2$. *Physical Review Letters* **101**, 026401 (2008).

[93] Blackstead, H. A. & Dow, J. D. Implications of Abrikosov-Gor'kov exchange scattering for theories of high-temperature superconductivity. *Physics Letters A* **206**, 107–110 (1995).

[94] Mackenzie, A. P. *et al.* Extremely strong dependence of superconductivity on disorder in Sr_2RuO_4. *Physical Review Letters* **80**, 161–164 (1998).

[95] Bauer, E. D. *et al.* Thermodynamic and transport investigation of CeCoIn$_{5-x}$Sn$_x$. *Physical Review B* **73**, 245109 (2006).

[96] Kitaoka, Y., Ishida, K. & Asayama, K. Impurity Effect in High-T_c Superconductors – A Consistent Analysis by d-Wave Superconducting Model –. *Journal of the Physical Society of Japan* **63**, 2052–2056 (1994).

[97] Orlando, T. P., McNiff, E. J., Foner, S. & Beasley, M. R. Critical fields, Pauli paramagnetic limiting, and material parameters of Nb$_3$Sn and V$_3$Si. *Physical Review B* **19**, 4545–4561 (1979).

[98] Chakraborty, B., Pickett, W. E. & Allen, P. B. Density of states, optical mass, and dc electrical resistance of Ta, W, Nb, and Mo using Slater-Koster interpolation. *Physical Review B* **14**, 3227–3230 (1976).

[99] Duong, N. P. Simultaneous structural and magnetic transitions in YFe$_4$Ge$_2$ studied by neutron diffraction and magnetic measurements. *Journal of Magnetism and Magnetic Materials* **236**, 14–27 (2001).

[100] Rullier-Albenque, F., Alloul, H. & Tourbot, R. Influence of Pair Breaking and Phase Fluctuations on Disordered High T_c Cuprate Superconductors. *Physical Review Letters* **91**, 047001 (2003). 0410502.

[101] Wang, G. & Shi, X. Electronic structures and magnetism of YM$_2$Ge$_2$(M = Mn-Cu): Ge-hight dependent magnetic ordering in YFe$_2$Ge$_2$. *Computational Materials Science* **121**, 48–53 (2016).

[102] Gegenwart, P. *et al.* Breakup of Heavy Fermions on the Brink of "Phase A" in CeCu$_2$Si$_2$. *Physical Review Letters* **81**, 1501–1504 (1998).

[103] Bachmann, M. D. *et al.* Spatial control of heavy-fermion superconductivity in CeIrIn$_5$. *Science* **366**, 221–226 (2019).

[104] Chen, J., Gamża, M. B., Semeniuk, K. & Grosche, F. M. Supplementary material: Composition dependence of bulk superconductivity in YFe$_2$Ge$_2$. *Physical Review B* **99**, 020501 (2019).

[105] Aharoni, A. Demagnetizing factors for rectangular ferromagnetic prisms. *Journal of Applied Physics* **83**, 3432–3434 (1998).

[106] Clem, J. R. & Hao, Z. Theory for the hysteretic properties of the low-field dc magnetization in type-II superconductors. *Physical Review B* **48**, 13774–13783 (1993).

[107] Bryant, C. A. & Keesom, P. H. Low-Temperature Specific Heat of Indium and Tin. *Physical Review* **123**, 491–499 (1961).

[108] Chan, Y. C. *et al.* Anisotropic two-gap superconductivity and the absence of a Pauli paramagnetic limit in single-crystalline LaO$_{0.5}$F$_{0.5}$BiS$_2$. *Physical Review B* **97**, 1–6 (2018). 1710.10841.

[109] Hu, C.-R. Numerical Constants for Isolated Vortices in Superconductors. *Physical Review B* **6**, 1756–1760 (1972).

[110] Wilhelm, H., Lühmann, T., Rus, T. & Steglich, F. A compensated heat-pulse calorimeter for low temperatures. *Review of Scientific Instruments* **75**, 2700–2705 (2004).

[111] Hardy, F. *et al.* Strong correlations, strong coupling, and s -wave superconductivity in hole-doped $BaFe_2As_2$ single crystals. *Physical Review B* **94**, 1–18 (2016).

[112] Wu, Y. *et al.* Supplementary material: Emergent Kondo Lattice Behavior in Iron-Based Superconductors AFe_2As_2 (A= K, Rb, Cs). *Physical review letters* **116**, 147001 (2016).

[113] Gastiasoro, M. N., Hirschfeld, P. J. & Andersen, B. M. Impurity states and cooperative magnetic order in Fe-based superconductors. *Physical Review B - Condensed Matter and Materials Physics* **88**, 1–5 (2013).

[114] Wang, Y., Kreisel, A., Hirschfeld, P. J. & Mishra, V. Using controlled disorder to distinguish s and s_{++} gap structure in Fe-based superconductors. *Physical Review B - Condensed Matter and Materials Physics* **87**, 1–6 (2013).

[115] Shaw, R. W., Mapother, D. E. & Hopkins, D. C. Critical Fields of Superconducting Tin, Indium, and Tantalum. *Physical Review* **120**, 88–91 (1960).

[116] Khasanov, R. *et al.* Proximity-induced superconductivity within the insulating $(Li_{0.84}Fe_{0.16})$OH layers in $(Li_{0.84}Fe_{0.16})$OH$Fe_{0.98}$Se. *Physical Review B* **93**, 1–11 (2016). 1602.06240.

[117] Rourke, P. M. & Julian, S. R. Numerical extraction of de Haas-van Alphen frequencies from calculated band energies. *Computer Physics Communications* **183**, 324–332 (2012). 0803.1895.

[118] Qazilbash, M. M. *et al.* Electronic correlations in the iron pnictides. *Nature Physics* **5**, 647–650 (2009). 0909.0312.

[119] Nakajima, M. *et al.* Normal-state charge dynamics in doped $BaFe_2As_2$: Roles of doping and necessary ingredients for superconductivity. *Scientific Reports* **4**, 1–6 (2014).

[120] Richard, P., Sato, T., Nakayama, K., Takahashi, T. & Ding, H. Fe-based superconductors: An angle-resolved photoemission spectroscopy perspective. *Reports on Progress in Physics* **74** (2011). 1110.6751.

[121] Yi, M. *et al.* Electronic reconstruction through the structural and magnetic transitions in detwinned NaFeAs. *New Journal of Physics* **14** (2012).

[122] Tamai, A. *et al.* Strong electron correlations in the normal state of the iron-based $FeSe_{0.42}Te_{0.58}$ superconductor observed by angle-resolved photoemission spectroscopy. *Physical Review Letters* **104**, 2–5 (2010).

[123] Yi, M. *et al.* Observation of universal strong orbital-dependent correlation effects in iron chalcogenides. *Nature Communications* **6**, 1–7 (2015).

[124] Hussey, N. E., Takenaka, K. & Takagi, H. Universality of the Mott-Ioffe-Regel limit in metals. *Philosophical Magazine* **84**, 2847–2864 (2004).

[125] Si, Q., Yu, R. & Abrahams, E. High-temperature superconductivity in iron pnictides and chalcogenides. *Nature Reviews Materials* **1** (2016). 1604.03566.

[126] Liu, M. *et al.* Nature of magnetic excitations in superconducting $BaFe_{1.9}Ni_{0.1}As_2$. *Nature Physics* **8**, 376–381 (2012). 1202.2827.

[127] de'Medici, L. Weak and strong correlations in fe superconductors. In *Iron-Based Superconductivity*, 409–441 (Springer, 2015).

[128] Wang, X. *et al.* Covalency, double-counting, and the metal-insulator phase diagram in transition metal oxides. *Physical Review B - Condensed Matter and Materials Physics* **86**, 1–10 (2012).

[129] Dong, J. K. *et al.* Quantum criticality and nodal superconductivity in the FeAs-Based superconductor KFe_2As_2. *Physical Review Letters* **104**, 087005 (2010).

[130] Terashima, T. *et al.* Resistivity and upper critical field in KFe_2As_2 single crystals. *Journal of the Physical Society of Japan* **78**, 17–20 (2009). 0903.3783.

[131] Hardy, F. *et al.* Multiband superconductivity in KFe_2As_2 : evidence for one isotropic and several Liliputian energy gaps. *J. Phys. Soc. Jpn.* **83**, 014711 (2014). arXiv: 1309.5654v1.

[132] Khim, S. *et al.* A calorimetric investigation of $RbFe_2As_2$ single crystals. *Physica Status Solidi (B) Basic Research* **254**, 1–7 (2017).

[133] Kasahara, S. *et al.* Evolution from non-Fermi- to Fermi-liquid transport via isovalent doping in $BaFe_2(As_{1-x}P_x)_2$ superconductors. *Physical Review B - Condensed Matter and Materials Physics* **81**, 1–5 (2010). 0905.4427.

[134] Shibauchi, T., Carrington, A. & Matsuda, Y. A Quantum Critical Point Lying Beneath the Superconducting Dome in Iron Pnictides. *Annual Review of Condensed Matter Physics* **5**, 113–135 (2014). 1304.6387.

[135] Nakatsuji, S. *et al.* Superconductivity and quantum criticality in the heavy-fermion system β-$YbAlB_4$. *Nature Physics* **4**, 603–607 (2008).

[136] Matsumoto, Y. *et al.* Quantum criticality without tuning in the mixed valence compound β-$YbAlB_4$. *Science* **331**, 316–319 (2011). 1101.4302.

[137] Gegenwart, P. *et al.* Magnetic-field induced quantum critical point in $YbRh_2Si_2$. *Physical Review Letters* **89**, 056402/1–056402/4 (2002). 0206289.

[138] Stewart, G. R. Non-Fermi-liquid behavior in d- and f-electron metals. *Reviews of Modern Physics* **73**, 797–855 (2001).

[139] Löhneysen, H. V., Rosch, A., Vojta, M. & Wölfle, P. Fermi-liquid instabilities at magnetic quantum phase transitions. *Reviews of Modern Physics* **79**, 1015–1075 (2007). 0606317.

[140] Steglich, F. *et al.* New observations concerning magnetism and superconductivity in heavy-fermion metals. *Physica B: Condensed Matter* **223-224**, 1–8 (1996).

[141] Wiecki, P. *et al.* Competing Magnetic Fluctuations in Iron Pnictide Superconductors: Role of Ferromagnetic Spin Correlations Revealed by NMR. *Physical Review Letters* **115**, 1–5 (2015). 1508.07506.

[142] Pikul, A. P. *et al.* Search for unconventional superconductors among the YTE_2Si_2 compounds (TE = Cr, Co, Ni, Rh, Pd, Pt). *Journal of Physics Condensed Matter* **29** (2017).

[143] Gupta, R., Dhar, S. K., Thamizhavel, A., Rajeev, K. P. & Hossain, Z. Superconducting and charge density wave transition in single crystalline $LaPt_2Si_2$. *Journal of Physics Condensed Matter* **29** (2017).

[144] Ciesielski, K. *et al.* Low-temperature electronic properties and band structures of $LaTE_2Si_2$ (TE=Fe, Co, Ag and Au). *Solid State Communications* **257**, 32–35 (2017).

[145] Chajewski, G. *et al.* Superconductivity in YTE_2Ge_2 compounds (TE= d-electron transition metal). *Physica B: Condensed Matter* **536**, 767–772 (2018).

[146] Singh, D. J. Evidence for proximity of YFe_2Si_2 to a magnetic quantum critical point. *Physical Review B* **93**, 1–6 (2016). 1604.06768.

[147] Ferstl, J., Rosner, H. & Geibel, C. Evidence for fluctuating Fe-moments in RFe_2Ge_2. *Physica B: Condensed Matter* **378-380**, 744–745 (2006).

Appendix A

Preliminary quantum oscillation measurements

Before the rotational study of the dHvA oscillations described in Section 5.4 was carried out, a preliminary investigation to detect quantum oscillations in crystals grown using the liquid transport method was first performed at a fixed angle in the dilution refrigerator. Two measurement methods were used in this initial study, namely the measurement of dHvA effect in ac susceptibility and the tunnel-diode oscillation (TDO) technique.

For optimising productivity in each fridge run, the initial QO measurements were carried out in parallel with other experiments. In particular two pressure-cells were mounted on the same measurement probe (see e.g. Fig. A.1) during the same run. This has limited the base temperature achievable in the case of the dHvA measurements, because of induction heating in the cell bodies by the ac modulation field. Meanwhile, the base temperature in the TDO measurements was itself affected by the heating from its circuitry during operation. Despite these limitations, clear oscillatory signals have been observed.

For the dHvA measurement, a YFe_2Ge_2 sample (JT1902-06, 18.7 mg) was placed inside the pick-up coils situated on the platform. The platform was then mounted to the lower end of the probe. The right panel in Fig. A.1 shows the coils on this platform on the right-hand side. The sample was oriented with the crystallographic a-axis parallel to the central axis of the pickup coils, which was in turn parallel to the AC-modulation and DC field direction. The two pick-up coils, each having around 900 turns with a resistance of around $210\,\Omega$ at room temperature, are counterwound. Care was taken to adjust the windings of the two coils so that they are well compensated when no sample was present. To provide good thermal conduction of the sample to the dilution refrigerator, a $50\,\mu m$ silver wire was spot welded to the sample, and the contact was further reinforced by a droplet of silver epoxy H20E cured at $80\,°C$. The other end of the silver wire was subsequently soldered onto another thicker silver wire
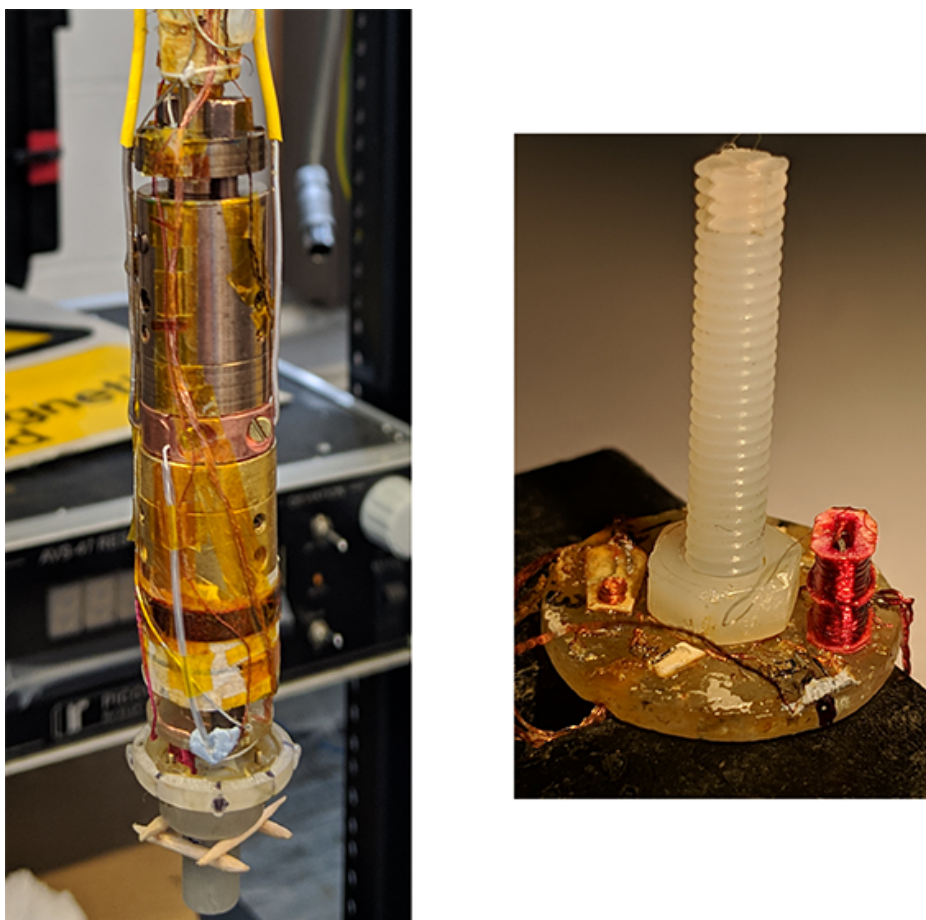
Fig. A.1 (Left) Picture showing the end of the dilution refrigerator sample probe where two diamond-anvil pressure cells are mounted on top of the sample platform for the dHvA and TDO coils. (Right) Picture showing the sample platform with a small TDO coil on the bottom left and a dHvA coil-set on the right.

which was heat sunk against the mixing chamber of the dilution refrigerator. A modulation frequency of 34 Hz was used to obtain a good signal-to-noise ratio. The oscillatory voltage was amplified by a low-temperature transformer at 1:30 ratio and measured by an SR830 lock-in amplifier.

As for the TDO technique, two small samples of YFe$_2$Ge$_2$ (from batch JT1902) were glued on top of one another with their ab-planes in parallel and placed inside a coil (18 turns; 40 μm copper wires; inner diameter 1.2 mm) which formed the main inductance of a resonant LCR tank circuit. A tunnel diode which was DC-biased into its negative differential resistance regime ($dV/dI < 0$) drove oscillation near the resonant frequency $\omega_0 \simeq 1/\sqrt{LC}$ of the tank circuit. Changes in both conductivity and susceptibility of the samples (e.g.
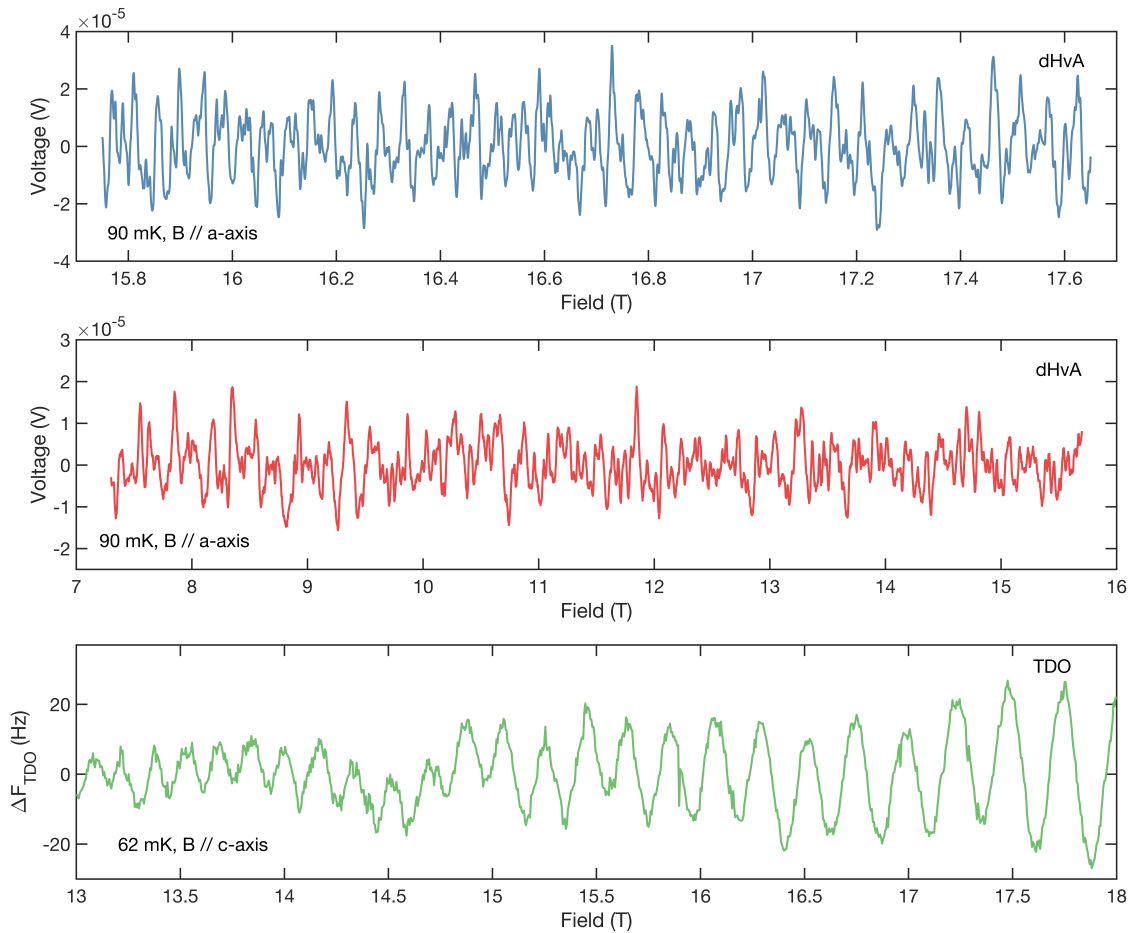
Fig. A.2 The de Haas-van Alphen effects (upper and middle panels) and tunnel-diode oscillation (lower panel) of YFe$_2$Ge$_2$. Background signals, approximated as low-order polynomials, have been subtracted from these data. For the dHvA measurements, magnetic field is applied along the crystallographic a-axis, while magnetic field is along the c-axis for samples measured in the TDO technique. These measurements were performed on samples from batch JT1902.

from Shubnikov-de Haas or dHvA oscillations, respectively) were detected as shifts in the TDO frequency. The samples were aligned with their c-axes parallel to both the coil axis and the main DC magnetic field. In order to reduce sample heating, the low-power 100 µA tunnel diode was operated in a pulsed mode (100 ms on and 900 ms off). In zero field at low temperatures, the oscillator frequency was ∼ 74 MHz, with a typical standard deviation in frequency of the order of several hertz.
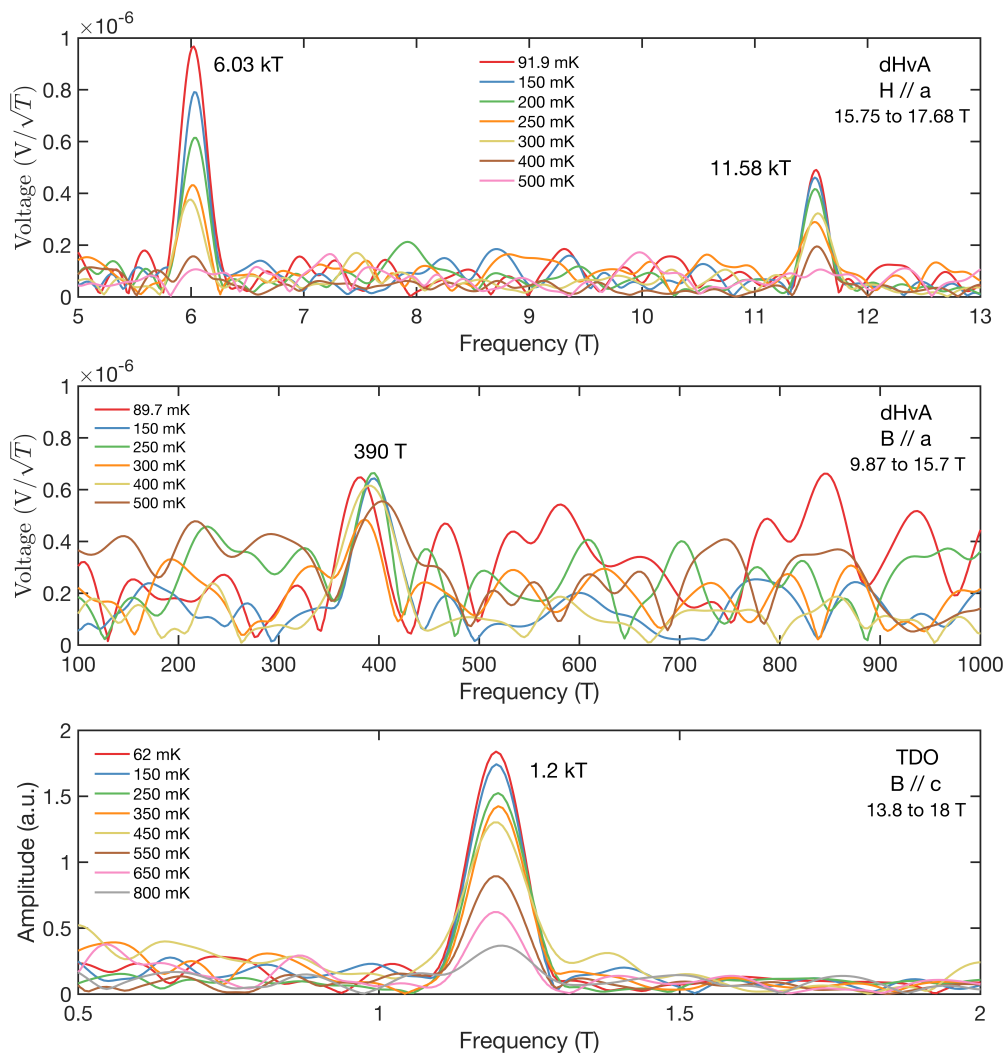
Fig. A.3 Fast-Fourier-transform spectra of the de Haas-van Alphen (upper and middle panel) and TDO (lower panel) signals at different temperatures. In order to observe the 390 T peak, dHvA data at a lower field interval has been taken for obtaining the FFT spectra in the middle panel.
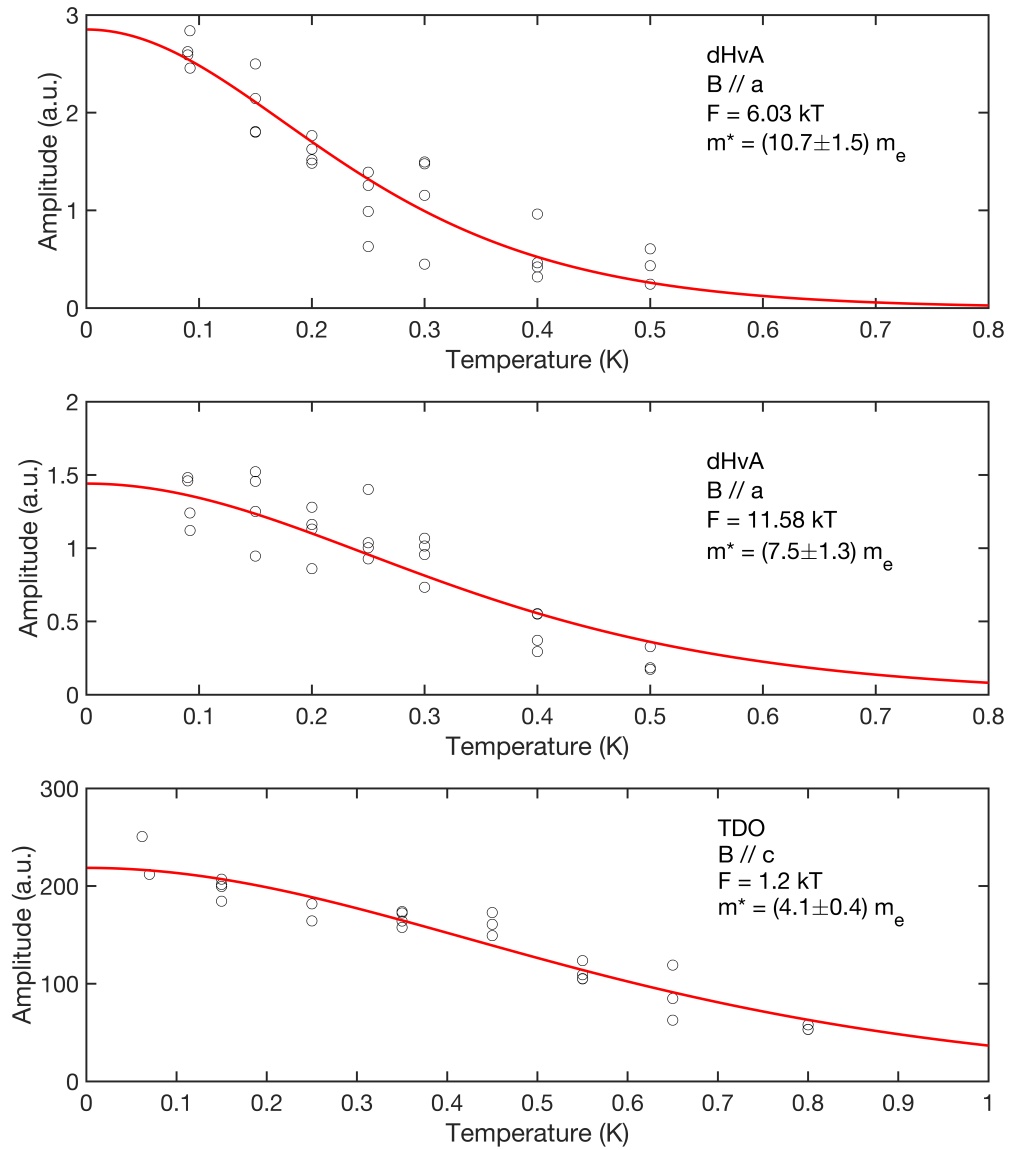
Fig. A.4 The temperature dependences of three frequencies shown in the FFT spectra in Fig. A.3 are fitted to the thermal smearing factor R_T of the Lifshitz-Kosevich theory to obtain estimates of the effective masses.

Table A.1 Table comparing the frequencies and quasiparticle masses for different Fermi-surface orbits between the DFT-calculated and experimentally measured values. The Band numbers correspond to the Fermi surface sheets shown in Fig. 5.32.

| Band	DFT		Experiment		$m_{\mathrm{exp}}/m_{\mathrm{DFT}}$
	Freq. (kT)	Mass (m^*/m_e)	Freq. (kT)	Mass (m^*/m_e)	
33 ($B//a$)	5.73	2.63	6.03	10.71 ± 1.5	4.1 ± 0.6
34 ($B//a$)	12.0	2.66	11.54	7.5 ± 1.3	2.8 ± 0.5
32 ($B//c$)	2.89	1.58	1.2	4.1 ± 0.4	2.6 ± 0.3

The typical field-dependence of the measured in-phase voltage signal from the susceptibility coil and the measured shift in TDO frequency are shown in Fig. A.2. Low-order polynomial backgrounds have been subtracted from the data. In Fig. A.2, the top and middle panel are data taken at two different magnetic field sweep rates and in different field ranges. As discussed below, the lower field range is needed to resolve the low frequency oscillation. A fast Fourier transform (FFT) procedure was performed on the background-subtracted data in $1/B$ for both the dHvA signals and the TDO frequency signals measured at different temperatures. From the FFT spectra of the dHvA signals (top and middle panels in Fig. A.3) three distinct frequency peaks can be observed, whereas the FFT spectra of the TDO signals (bottom panel in Fig. A.3) reveal a single frequency.
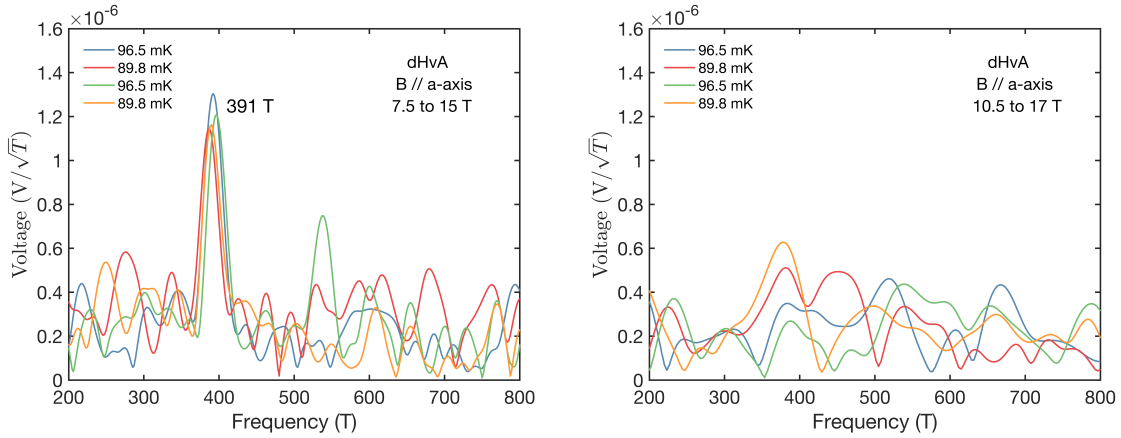

Fig. A.5 Low-frequency region of the fast-Fourier-transform spectra produced using the low-field (left panel) and higher-field (right panel) intervals of the de Haas-van Alphen signals. Although the background noise levels appear the same in both spectra, the peak at around 391 T is not detected for the signal at the higher-field interval.

The temperature dependence of the oscillation amplitudes extracted from these FFT spectra enables the fitting of the Lifshitz-Kosevich (L-K) formula (Equ. 2.44) and hence estimates of the effective quasiparticle masses on each corresponding Fermi surface. Fig. A.4 shows the L-K fits of the peak amplitudes (integrated over the area under the peaks in the FFT spectrum taking into account the overlap with neighbouring peaks) for three frequency peaks. Little suppression with increasing temperature was observed for the low-frequency peak at around $\sim 390\,$T. This suggests a low quasiparticle mass for this particular frequency. The slow suppression with increasing temperature and the relatively weak amplitude compared to background noise make the fitting to the available data difficult for this frequency. Furthermore, the oscillation amplitude of this peak seems to be suppressed as magnetic field is increased so that at the field ranges higher than $14\,$T, the oscillation corresponding to this frequency cannot be resolved. This is illustrated by the difference between the spectra in the left and right panels of Fig. A.5. Although the noise level is similar in both figures, by including data at the lower field range, the amplitudes of this low frequency peak appear to be significantly larger. This suggests that there may be a change of the Fermi surface topology at high fields.

Table A.1 summarises the experimentally obtained QO frequencies and quasi-particle masses from the dHvA and TDO measurements. Results from these early measurements matched reasonably well with those obtained from the rotational study in Section 5.4, although the obtained mass enhancements are slightly lowered.

Appendix B

Supplementary tables and figures

Tables B.1 to B.3 list the sets of data which have been used for plotting Fig. 4.3 and Fig. 4.8 in Chapter 4 and Fig. 5.12 in Chapter 5.

Figs. B.1 to B.3 show the original heat capacity data of YFe_2Ge_2 sampels SR1726-02 and JT1902-11 measured down to $30\,mK$, which display the anomalous field-dependent upturn at low temperatures.

Table B.1 Samples for which the RRR and T_c values have been used for plotting Fig. 4.3.

Ingot #	Sample label	Nominal Composition $Y_{1+x}[Fe_{1+y}Ge_{1+z}]_2$			Annealed? (Y/N)	RRR	T_c (K)		
		x (%)	y (%)	z (%)			80%	50%	20%
26	RF26A01	10.1	0	0.3	N	29	-	-	-
	RF26A01				Y	80	1.84	1.77	1.68
29	RF29A01	5.2	0	-1	N	18	0.66	0.41	-
	RF29A03	5.2			Y	67	1.42	1.27	1.12
37	RF37A01	2.1	0	-0.1	N	30	1.14	1.06	0.98
	RF37A02				Y	80	1.71	1.62	1.53
45	RF45A01	-2.1	0	0	N	8.3	-	-	-
	RF45A02				Y	39	1.42	1.31	1.2
23	RF23C02	-3.4	0	0	N	7.5	-	-	-
	RF23C02				Y	33	1.29	1.18	1.06
44	RF44A01	-10	0	0	N	7.3	-	-	-
	RF44A02				Y	42	1.66	1.56	1.41
32	RF32A01	0	10.3	0	N	25	1.3	1.14	1.01
	RF32A04				Y	143	1.97	1.84	1.74
34	RF34B01	0	5.3	0	N	39	1.58	1.44	1.14
	RF34B02				Y	211	1.92	1.87	1.82
25	RF25A01	0	1.9	0	N	20	1.64	1.53	1.42
	RF25A01				Y	100	1.83	1.7	1.6
35	RF35A01	0	-2	0	N	9.6	0.61	-	-
	RF35A02				Y	78	1.68	1.52	1.36
42	RF42A01	0	-5.1	-0.1	N	7.9	-	-	-
	RF42A02				Y	60	1.11	0.95	0.8
27	RF27A01	0	-9.1	0.2	N	11	0.88	0.69	0.42
	RF27A02				Y	32	1.33	1.19	1.02
43	RF43A01	0	-0.1	9	N	6.0	-	-	-
	RF43A02				Y	37	1.29	1.21	1.07
57	RF57A01	0	0	4.9	N	6.8	-	-	-
	RF57A03				Y	30	1.19	1.06	0.93
36	RF36A01	0	-0.1	2	N	9.4	-	-	-
	RF36A03				Y	56	1.51	1.3	1.11
24	RF24A01	0	0	-2.1	N	38	1.14	0.99	0.87
	RF24A01				Y	68	1.92	1.83	1.79
22	RF22A02	0	0	-5.2	N	26	1.41	1.25	1.17
	RF22A02				Y	109	1.92	1.8	1.74
33	RF33A01	0	0	-10.1	N	27	1.28	1.12	1
	RF33A02				Y	55	1.57	1.45	1.34
66	RF66B02	0	0	0	N	7.8	-	-	-
	RF66A01				Y	43	1.49	1.26	1.01

Table B.2 Lattice parameters a and c from refinements of the powder X-ray diffraction data for a range of polycrystalline ingots and the highest measured RRR for each annealed ingot. These data have been used for plotting Fig. 4.8.

Ingot #	a (Å)	c (Å)	RRR
22	3.96338(1)	10.45627(4)	109
23	3.96333(1)	10.45489(5)	33
24	3.96353(1)	10.45557(4)	68
25	3.96380(1)	10.45494(3)	100
27	3.96335(1)	10.45240(4)	32
	3.96355(1)	10.45310(5)	
	3.96327(1)	10.45195(3)	
	3.96387(1)	10.45309(3)	
	3.96399(1)	10.45418(4)	
29	3.96348(1)	10.45496(3)	67
	3.96363(1)	10.45534(3)	
	3.96349(1)	10.45558(4)	
	3.96375(1)	10.45585(3)	
	3.96356(1)	10.45551(3)	
	3.96348(1)	10.45551(4)	
32	3.96353(1)	10.45580(4)	143
34	3.96325(1)	10.45605(4)	211
35	3.96340(1)	10.45473(4)	78
36	3.96346(1)	10.45475(4)	56
37	3.96344(1)	10.45544(5)	80
42	3.96333(1)	10.45414(4)	60
43	3.96355(1)	10.45373(4)	37
44	3.96352(1)	10.45369(4)	42
45	3.96341(1)	10.45401(4)	39
57	3.96336(1)	10.45168(6)	30
66	3.96328(1)	10.45347(4)	43
72	3.96336(2)	10.45524(5)	122
	3.96351(1)	10.45533(5)	
	3.96320(1)	10.45506(4)	
	3.96321(1)	10.45506(4)	
	3.96338(2)	10.45523(6)	
	3.96352(1)	10.45516(4)	
73	3.96342(1)	10.45588(4)	178
	3.96346(1)	10.45670(4)	
	3.96377(1)	10.45718(4)	
	3.96376(1)	10.45711(4)	
	3.96323(2)	10.45646(6)	

Table B.3 Lattice parameters a and c from refinements of the powder X-ray diffraction data for a range of single crystal batches and the typical RRR measured for each batch. These data have been used for plotting Fig. 5.12.

| Batch label	a (Å)	c (Å)	RRR
SR1703	3.96351(1)	10.45359(5)	50
SR1704	3.96302(1)	10.45197(4)	56
SR1726	3.96369(2)	10.45489(9)	172
SR1727	3.96347(1)	10.45554(5)	66
SR1728	3.96350(1)	10.45555(5)	106
SR1730	3.96328(2)	10.45779(10)	200
SR1732	3.96349(1)	10.45611(4)	88
JT1902	3.96344(1)	10.45699(4)	328
JC1904	3.96364(1)	10.45785(5)	463
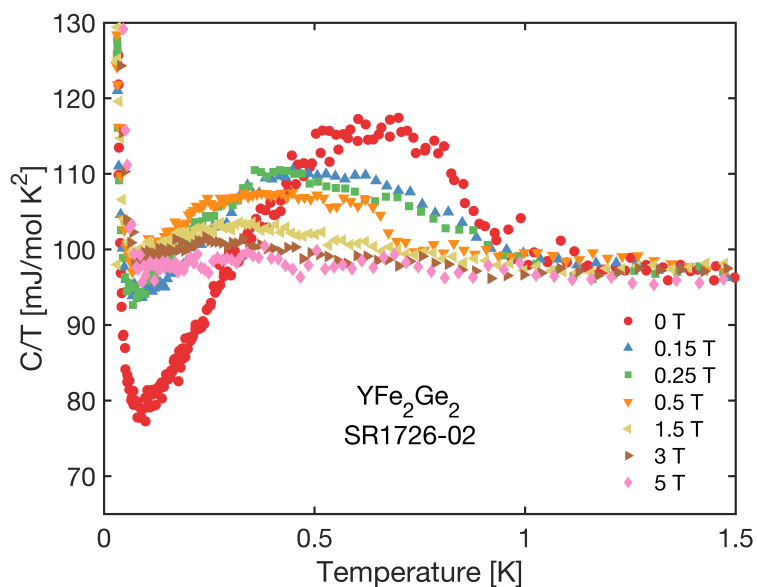
Fig. B.1 C/T of YFe$_2$Ge$_2$ single crystal sample SR1726-02.
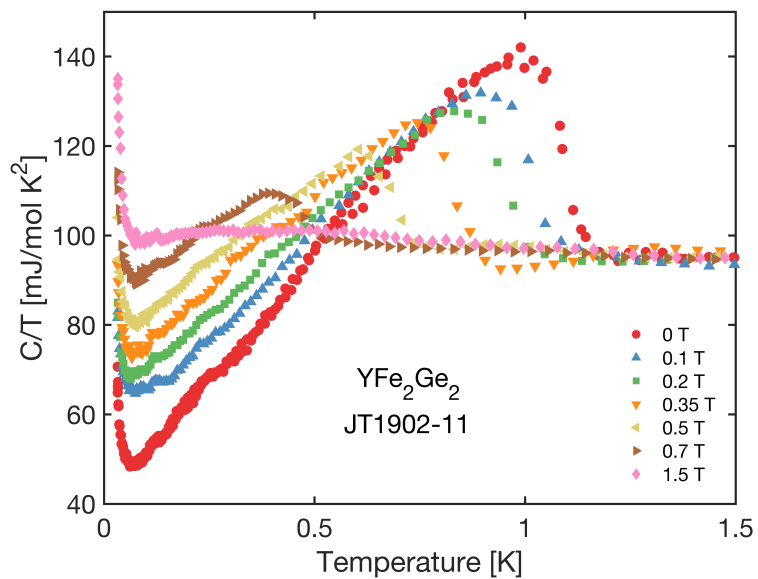
Fig. B.2 C/T of YFe$_2$Ge$_2$ single crystal sample JT1902-11 both in zero field and at low applied magnetic fields.
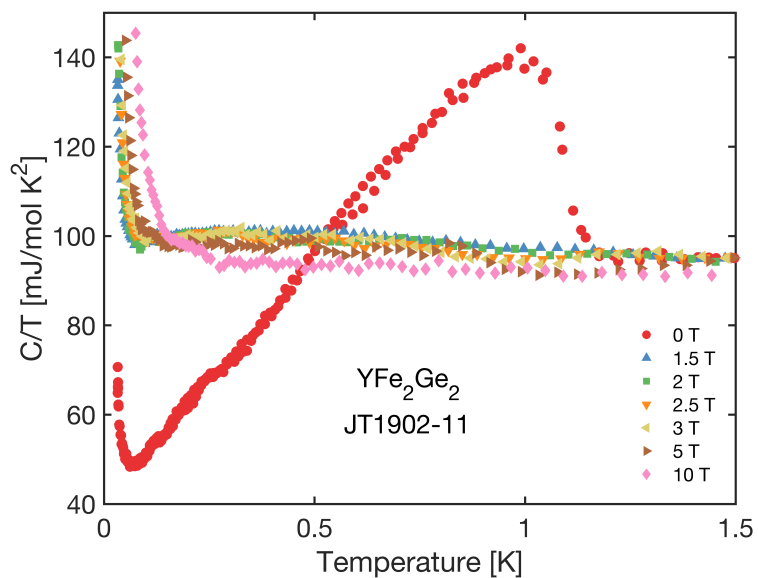
Fig. B.3 C/T of YFe$_2$Ge$_2$ single crystal sample JT1902-11 both in zero field and at relatively high applied magnetic fields.